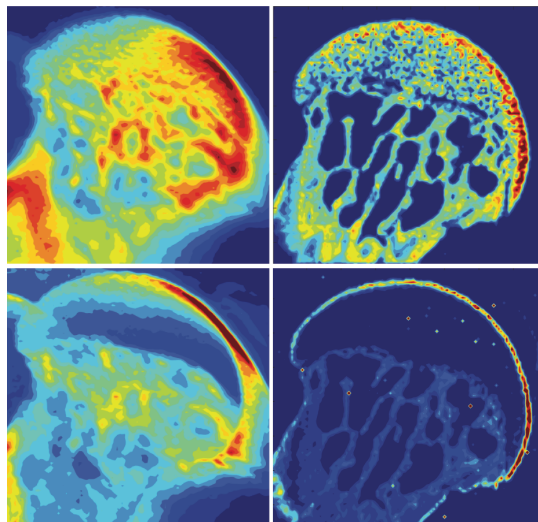# Distribution and Speciation of Tungsten in Bone

Cassidy R. VanderSchee

Thesis submitted to McGill University in partial fulfilment of the requirements for the degree of

Doctor of Philosophy

Department of Chemistry
McGill University, Montréal

April 2021

At Blackwater Pond the tossed waters have settled
after a night of rain.
I dip my cupped hands. I drink
a long time. It tastes
like stone, leaves, fire. It falls cold
into my body, waking the bones. I hear them
deep inside me, whispering
oh what is that beautiful thing
that just happened?

Mary Oliver

To my parents, Colleen and Lennard

Table of Contents

Abstract

Tungsten is generally understood as non-toxic. Recently, however, it has been associated with various medical conditions including pediatric leukemia. Tungsten has been shown to accumulate in bone, a well-known storage site for both essential and toxic metals in the body. The uptake mechanism of tungsten and other metals in bone, however, is poorly understood due to difficulty modelling the local environment of bone with *in vitro* experiments. Biomimetic studies are needed to accurately determine metal distribution and form *in vivo* so that the potential consequences of metal uptake in bone are fully understood.

This thesis aims to elucidate the mechanism of tungsten uptake in bone through the *in situ* study of tungsten distribution and speciation. Synchrotron radiation micro X-ray fluorescence (μXRF) and laser ablation inductively coupled plasma mass spectroscopy (LA-ICP-MS) are used to map tungsten distribution in specially prepared bone thin-sections. LA-ICP-MS provided significantly higher sensitivity and image resolution compared to μXRF measurements in bone. To quantitatively determine metal concentrations in bone using LA-ICP-MS, matrix-matched calibration standards were developed and tested for accuracy. Information on the oxidation state and local environment of tungsten in bone is investigated using micro X-ray absorption near-edge structure (μXANES).

μXRF and LA-ICP-MS results indicate that tungsten is heterogeneously accumulated across all bone tissues. Furthermore, the persistence of tungsten in cortical bone tissue following removal of the original source, indicates that tungsten is retained in an insoluble form and that bone-associated tungsten may be a further source of chronic exposure. μXANES spectra for tungsten in these tissues indicate that it is no longer in the originally administered form, orthotungstate, but resembles the heteropolytungsate species, phosphotungstate. Not only does this have alarming toxicological implications, it also points towards an accumulation mechanism related to bone-remodeling.

Lastly, the extension of these techniques to the study of other metal systems in bone, specifically zinc and copper, is demonstrated. Copper was found as a reduced Cu(I) species in the ligaments and articular cartilage of the knee and hip joint. Zinc was found in areas of active calcification in bone and articular cartilage. Similarity between zinc and tungsten accumulation in cortical bone further supports a connection between tungsten uptake and bone remodeling.

Résumé

Bien que le tungstène soit généralement considéré comme non toxique, il a récemment été associé à diverses pathologies, notamment la leucémie infantile. Il a été démontré que le tungstène s'accumule dans les os, un site de stockage bien connu des métaux essentiels et toxiques dans l'organisme. Cependant, le mécanisme d'absorption du tungstène et d'autres métaux dans l'os est mal compris en raison de la difficulté de modéliser la structure et la chimie complexes des métaux et de l'os par des expériences in vitro. Des études biomimétiques sont nécessaires pour déterminer avec précision la distribution et la forme des métaux in vivo, afin que les conséquences potentielles de l'absorption des métaux dans l'os soient pleinement comprises.

Cette thèse vise à élucider le mécanisme d'absorption du tungstène dans l'os par l'étude *in situ* de la distribution et de la spéciation du tungstène. La microfluorescence des rayons X par rayonnement synchrotron (µXRF) et la spectroscopie de masse à plasma inductif par ablation laser (LA-ICP-MS) sont utilisées pour cartographier la distribution du tungstène dans des sections minces d'os spécialement préparées. Il a été constaté que la LA-ICP-MS offrait une sensibilité et une résolution d'image nettement supérieures à celles des mesures µXRF dans l'os. Afin de déterminer quantitativement les concentrations de métaux dans les os à l'aide de la LA-ICP-MS, des normes d'étalonnage appariées à la matrice ont été développées et testées pour leur précision. Les informations sur l'état d'oxydation et l'environnement local du tungstène dans l'os sont étudiées à l'aide de l'absorption des micro-rayons X près de la structure d'arête (µXANES).

Les résultats µXRF et LA-ICP-MS indiquent que le tungstène est accumulé de manière hétérogène dans tous les tissus osseux. En outre, la persistance du tungstène dans le tissu osseux cortical après l'élimination de la source d'origine indique que le tungstène est conservé sous une forme insoluble et que le tungstène associé à l'os peut constituer une source supplémentaire d'exposition chronique. Les spectres µXANES du tungstène dans ces tissus indiquent qu'il n'est plus sous la forme administrée à l'origine, l'orthotungstate, mais qu'il ressemble plutôt à l'espèce hétéropolytungsate, le phosphotungstate. Ce constat a non seulement des implications toxicologiques alarmantes, mais il oriente également vers un mécanisme d'accumulation lié au remodelage osseux.

Enfin, l'extension de ces techniques à l'étude d'autres systèmes métalliques dans l'os, notamment le zinc et le cuivre, est démontrée. Le cuivre a été trouvé sous forme d'une espèce

réduite de Cu(I) dans les ligaments et le cartilage articulaire du genou et de la hanche. Le zinc a été trouvé dans les zones de calcification active du tissu osseux et du cartilage articulaire. La similitude entre l'accumulation de zinc et de tungstène dans l'os cortical confirme le lien entre l'absorption de tungstène et le remodelage osseux.

Acknowledgements

List of Abbreviations

ALP	alkaline phosphatase
APS	Advanced Photon Source
BEI	backscattered electron imaging
BMU	basic multicellular unit
BN	bone standard
CLS	Canadian Light Source
EPR	electron paramagnetic resonance
ESEEM	electron spin echo envelope modulation
ESR	electron spin resonance
ETM	early transition metal
HA	hydroxyapatite standard
HAP	hydroxyapatite
HERFD	high-energy resolution fluorescence detected
HC	7:3 hydroxyapatite:collagen standard
ICRP	International Commission on Radiological Protection
IR	infrared
IRIF	image resolution improvement factor
KB	Kirkpatrick-Baez
LA-ICP-MS	laser ablation inductively coupled plasma mass spectrometry
LOD	limit of detection
LOX	lysyl oxidase
LTQ	lysine tyrosylquinone
m/z	mass-to-charge ratio
MMA	methyl methacrylate
MMP	matrix metalloproteinase
μXANES	micro-X-ray absorption near edge spectroscopy
NSLS-II	National Synchrotron Light Source II
NSRRC	National Synchrotron Radiation Research Center
OA	osteoarthritis
PBS	phosphate buffered solution
PET	positron emission tomography
POM	polyoxometalate
ppm	parts per million
R^2	coefficient of determination
RSD	relative standard deviation
SR-μXRF	Synchrotron radiation micro-X-ray fluorescence
SRM	standard reference material
SRX	Sub-micron resolution X-ray spectroscopy

$t_{1/2}$	half-life
TPQ	tryhydroxyphenethylamine quinone
TTP	tetratolylporphyrin
XANES	X-ray absorption near edge spectroscopy
XAS	X-ray absorption spectroscopy
XRD	X-ray diffraction
XRF	X-ray fluorescence

List of Figures

Chapter 4: Quantification of local zinc and tungsten deposits in bone with LA-ICP-MS using novel hydroxyapatite-collagen calibration standards

Chapter 5: Identification of local copper and zinc deposits in bone tissue

Chapter 6: Addressing K/L-edge overlap in elemental analysis from μXRF: bioimaging of tungsten and zinc in bone tissue using synchrotron radiation and LA-ICP-MS

List of Tables

Preface and Contributions of Authors

This thesis describes the distribution and speciation of tungsten in bone using synchrotron-based X-ray techniques and laser ablation inductively coupled mass spectrometry (LA-ICP-MS). These techniques can be applied to the investigation of other metals in bone as well, including essential trace metals copper and zinc.

Chapter 1 provides a literature review of pertinent topics related to early transition metal storage in bone. This includes the chemistry of early transition metals under physiological conditions, a basic description of bone biology and an overview of metal distribution in bone, and discussion of possible accumulation mechanisms for early transition metals in bone. This chapter is prepared for an unsubmitted review manuscript titled "Early transition metals and bone: distribution and uptake mechanisms," co-authored by C.R. VanderSchee and Prof. S. Bohle. The manuscript was written by C.R. VanderSchee and jointly edited by C.R. VanderSchee and Prof. S. Bohle.

Chapter 2 describes the application of synchrotron-based X-ray techniques, micro X-ray fluorescence (μXRF) and micro X-ray absorption spectrometry (μXAS) in determining the localization and speciation of tungsten in murine bone tissue. The work presented in Chapter 2 is published as a communication in *Communications Chemistry* entitled: "Accumulation of persistent tungsten in bone as *in situ* generated polytungstate." This article is co-authored by C.R. VanderSchee, D. Kuter, A.M. Bolt, F. Lo, R. Feng, J. Thieme, Y.K. Chen-Wiegart, G. Williams, K. K. Mann and Prof. S. Bohle. The manuscript and supporting information were written by C.R. VanderSchee and edited by all authors. C.R. Vanderschee conducted sample preparation, X-ray data collection and analysis, and figure preparation. D. Kuter aided with data collection and analysis. Beamline scientists (F. Lo, R. Feng, J. Thieme, Y.K. Chen-Wiegart, G. Williams) provided invaluable help with data collection at the synchrotrons. K.K. Mann and A.M. Bolt conducted the mouse exposure experiments and provided their biological expertise during data analysis.

Chapter 3 compares the ability of μXRF and LA-ICP-MS to measure tungsten and zinc distribution in bone. This work was published as a communication in *Analytical and Bioanalytical*

Chemistry, titled "Addressing K/L-edge overlap in elemental analysis from μXRF: bioimaging of tungsten and zinc in bone tissue using synchrotron radiation and LA-ICP-MS." This article was co-authored by C.R. VanderSchee, D. Kuter, H. Chou, B.P. Jackson, K. K. Mann and Prof. S. Bohle. The manuscript and supporting information were written by C.R. VanderSchee and edited by all authors. C.R. VanderSchee prepared the samples, collected and analyzed μXRF and LA-ICP-MS data, and prepared the figures. D. Kuter aided with data collection and analysis, with B.P. Jackson providing his invaluable expertise. K.K. Mann and H. Chou conducted mouse exposure experiments and provided their biological expertise during data analysis.

Chapter 4 describes the development of a novel LA-ICP-MS calibration method for *in situ* quantification of local tungsten and zinc deposits in bone. The work presented in this chapter was prepared for publishing in a manuscript titled "Quantification of local zinc and tungsten deposits in bone with LA-ICP-MS using novel hydroxyapatite-collagen calibration standards." This work is co-authored by C.R. VanderSchee, D. Frier, D. Kuter, K. K. Mann, B.P. Jackson, and Prof. S. Bohle. The manuscript and supporting information were written by C.R. VanderSchee and edited by all authors. C.R. VanderSchee prepared the samples, collected and analyzed ICP-MS and LA-ICP-MS data, and prepared the figures. D. Frier developed the ICP-MS digestion procedure. D. Kuter aided with LA-ICP-MS data collection and analysis and B.P. Jackson provided invaluable expertise. K.K. Mann conducted mouse exposure experiments and provided biological expertise during data analysis.

Chapter 5 extends the X-ray techniques described in Chapter 1 to investigate copper and zinc localization and form in bone tissue. The work described here has not yet been published in a peer-reviewed journal. The content of this chapter was written by C.R. VanderSchee and edited by Prof. S. Bohle. C.R. VanderSchee conducted all sample preparation, data collection, and analysis. APS beamline scientists M. Newville and Z. Finfrock provided invaluable assistance with X-ray data collection and analysis. K.K. Mann conducted mouse exposure experiments and M. Grant provided human tissue samples.

Chapter 1. Introduction - Early Transition Metals and Bone: Distribution and Uptake Mechanisms

1.1. Introduction

Early transition metals (ETMs), defined as Group 4-7 elements in the periodic table, are known for their unique hardness, high melting point, and tendency to form stable oxyphilic species.[1-3] These properties make them extremely valuable in several applications, especially as bone implant materials.[4] These metals are dispersed in the environment and can be found in many forms. The aqueous chemistry of Group 5 and 6 elements is particularly complex, with a number of species possible depending on pH, metal concentration, and the presence of other coordinating species.[5]

In the body, ETMs are known to accumulate primarily in bone.[6] Bone is a well-known storage site for both essential and toxic metals in the body.[7] While sequestering potential toxins in bone can be an efficient method for reducing their toxicity, this may also lead to a disturbance of local cellular function and chronic toxicity (depending on the concentration and form of the metal). The effects of ETMs on bone metabolism/bone cells have been discussed in depth,[4, 8-21] however, many studies do not take into account metal speciation in bone. Understanding the potential consequences of metal accumulation requires an understanding of how, and in what form, metals are interacting with bone tissue. The mechanism of ETM accumulation is poorly understood because of the complexity of bone tissue as well as the challenge of determining metal speciation *in vivo*.

In this chapter, we will briefly describe the chemistry of ETMs under physiological conditions and provide a basic explanation of bone biology followed with an overview of metal distribution in bone. These three sections will be brought together to discuss possible accumulation mechanisms for ETMs in bone.

1.2. Early Transition Metals

For the purposes of this review, we define ETMs as those elements which: a) are part of the main transition group or *d* block and contain partially filled *d* shells only and b) the highest oxidation state corresponds to the total number of *d* and *s* electrons in the atom.[22] Scandium and yttrium (Group 3) are not considered here as their chemistry is more similar to the lanthanide

series. By these parameters, the ETMs begin at Group 4 (Ti) and go until Group 7 (Mn). We can further classify ETMs by the first transition series (Ti, V, Cr, Mn) with partially filled *3d* shells, second transition series (Zr, Nb, Mo, Tc) with partially filled *4d* shells, and third transition series (Hf, Ta, W, Re) with partially filled *5d* shells.

1.2.1. Properties

One major way in which ETMs are differentiated from the late transition metals is with regards to their reactivity. ETMs are considerably more oxyphilic and less thiophilic compared to the later transition metals. This is related to their decreased electronegativity.[1] In addition, ETMs, with the exception of manganese, are considered refractory metals. Refractory metals are classified as having high melting points (> 1850°C), hardness, and wear resistance.[2, 3] These properties result in their use in many practical applications, including bone implant materials.[4]

When discussing the chemistry of the ETMs, it is useful to compare the individual Groups as well as the first transition series elements to the second and third. Because of the lanthanide contraction, the heavier atoms in a Group have very similar chemical properties which can differ considerably from those of the corresponding element in the first series.[5] For example, in Group 4, the properties of Nb and Ta are very similar to each while quite different from those of V. The lanthanide contraction occurs due to the filling of the *4f* shell and results in the contraction of atomic and ionic sizes of the third transition series so that their radius is nearly identical to the second transition series, as seen in Figure 1.1.

Chemical differences between the first transition series and the second and third transition series is seen in both the stable oxidation states and aqueous chemistry of the ETMs.[22] Though ETMs can exist in a number of oxidation states (Table 1.1), higher oxidation states are generally more stable for the heavier atoms of a group. Figure 1.1. shows the Arhens ionic radius of the early transition metals in their highest available oxidation state (i.e. Group 4 = +4, Group 5 = +5, etc.).[23] In the early transition metals, the highest oxidation state is typically found in oxo compounds.[22]
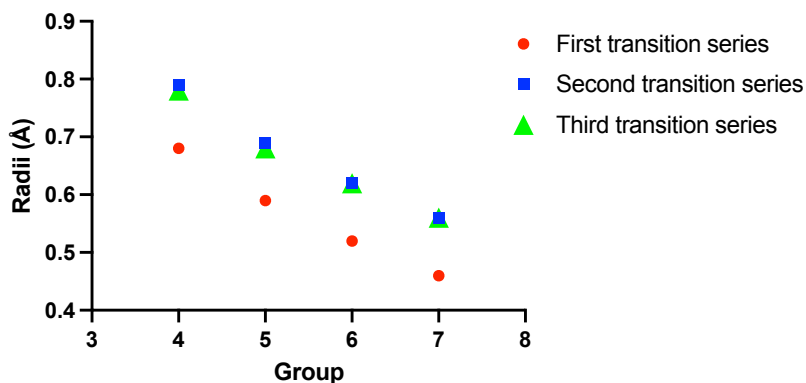
Figure 1.1. Ionic radius of the early transition metals in their highest oxidation state. Based on data from Shannon and Prewitt[23]

Group	Element	Symbol	Atomic Number	Aqueous O.S.	Dominant aqueous species at pH = 7.4*
4	Titanium	Ti	22	III, IV	$TiO_{2(s)}$
	Zirconium	Zr	40	IV	$ZrO_{2(s)}$
	Hafnium	Hf	72	IV	$HfO_{2(s)}$
5	Vanadium	V	23	IV, V	**V(IV):** VO_2^+ **V(V):** $H_2VO_4^-$
	Niobium	Nb	41	V	$Nb_2O_5 \bullet nH_2O$
	Tantalum	Ta	73	V	$Ta_2O_5 \bullet nH_2O$
6	Chromium	Cr	24	III, VI	**Cr(III):** $[Cr(H_2O)_5(OH)]^{2+}$; $[Cr(H_2O)_4(OH)_2]^+$ **Cr(VI):** CrO_4^{2-}
	Molybdenum	Mo	42	VI	MoO_4^{2-}
	Tungsten	W	74	VI	WO_4^{2-}
7	Manganese	Mn	25	II	Mn^{2+}
	Technetium	Tc	43	VII	TcO_4^-
	Rhenium	Re	75	VII	ReO_4^-

Table 1.1. Summary of aqueous chemistry of the early transition metal elements.[5] *At low metal concentration.

1.2.2. Aqueous Chemistry

The aqueous chemistry of the ETMs is complex, with several species possible depending on metal concentration, pH, redox environment, and presence of other ions. Therefore, a thorough discussion of the interaction of ETMs with bone requires careful consideration of their form under physiological conditions. Metal uptake in bone is preceded by transportation either in the blood or in the synovial fluid between bone implants and bone tissue.[24] Thus, metals in contact with bone tissue are in the form that is dominant in aqueous solutions at physiological pH, 7.4. Once at the bone, metals may undergo further speciation changes if subjected to the localized acidic

environments (pH ~4.5) with high calcium and phosphate concentrations present during bone remodeling.[25]

The hydrolysis behavior of the ETMs is described in detail by Baes and Mesmer.[5] Herein, we draw from this work and others to briefly describe the aqueous chemistry of each ETM under physiological conditions. A summary of the stable oxidation states in aqueous solution along with the dominant species at low metal concentration and pH 7.4 is found in Table 1.1. Generally, only the highest available oxidation states are stable in aqueous solution. The first transition series elements are also stable in other oxidation states and can form simple cationic complexes in aqueous solution.

1.2.2.1. Group 4: Titanium, Zirconium, Hafnium

Group 4 elements have a characteristic +4 oxidation state in solution. Ti can also exist in +3 oxidation state, but this is primarily at lower pHs than possible under physiological conditions. Group 4 metals hydrolyze at very low pHs (> 2) in water.[5, 26] However, at neutral pHs and in the absence of complexing agents, Ti^{4+}, Zr^{+4} and Hf^{+4} ions precipitate as insoluble oxides TiO_2, ZrO_2, and HfO_2. Ti(IV) has extremely low solubility at pH 7.4 (0.2 fM using the proposed soluble species $TiO(OH)_2$ with $K_{sp} = 1 \times 10^{-29}$).[27] Despite this, Ti is surprisingly abundant in humans and present in blood in nM concentrations, over a million times higher than predicted by the solubility.[28] Elevated levels of Ti(IV) in solution is due to chelation by small molecules and proteins, primarily blood protein serum transferrin. Zr and Hf, like Ti, bind to blood serum transferrin, elevating their solubility in the body as well.[29, 30]

1.2.2.2. Group 5: Vanadium, Niobium, Tantalum

The aqueous chemistry of vanadium is one of the most complicated among transition metals. Niobium and tantalum have a similar, though less complex, chemistry. In biological systems, vanadium exists in both anionic and cationic forms, primarily in +4 and +5 oxidation states, whereas niobium and tantalum only exist in the +5 oxidation state in water.[5] Group 5 metals undergo a number of redox, hydrolytic and condensation reactions in aqueous solution dependant on pH, metal concentration, and presence of coordinating ligands.

At neutral pH, vanadium exists as V(V) species, while acidic pHs favor the existence of cationic V(IV) species in the body.[31] The biochemistry of these species differs substantially and understanding their metabolism and biological effects is further complicated by the number of

possible complexes they can form with biogenic ligands and the ease of transition between V(V) and V(IV) oxidation states.[32] Whereas vanadium(IV) is particularly stable in the form of the vanadyl ion, VO^{2+}, the pentavalent ions of the Group 5 elements form oxyanions of varying polynuclearity dependant on pH and concentration.[5] For example, vanadium(V) forms mono- and divanadate species VO_4^{3-} and $V_2O_7^{4-}$ at concentrations below 2×10^{-5} M, while polyoxometalates such as metavanadate $(VO_3)_x^{x-}$ and decavanadate $V_{10}O_{28}^{6-}$ are formed at higher concentrations. The distribution of these species in aqueous solution depends on concentration and pH, as shown in Figure 1.2.[33] Similarly, at physiological pHs, niobium(V) and tantalum(V) form variably soluble $Nb_2O_5 \cdot nH_2O$ and $Ta_2O_5 \cdot nH_2O$ species whose solubility is enhanced by chelation.[34-36] At high metal concentrations and basic pHs, niobium and tantalum also condense into polyoxometalates (POMs), most typically hexametalate species $[H_xM_6O_{19}]^{(8-x)-}$.[33, 37-39]
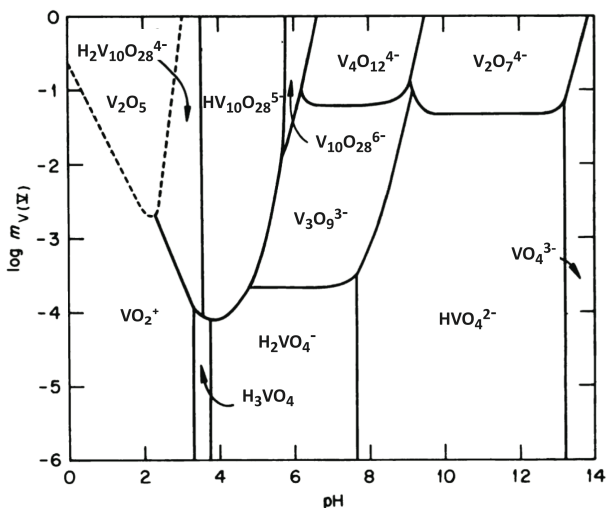
Figure 1.2. Predominance diagram for vanadate(V) species.[33]

Both Group 5 and 6 metals, apart from chromium, form POMs. The rich chemistry of POMs is extensive, and a full discussion is beyond the scope of this review. The topic is discussed in depth by Pope,[33] as well as in a number of more recent reviews.[40-45] There are two main characteristics of POM metals that distinguish them from other polyoxoanion metals such as Cr(VI).[46] First, these metals are able increase their coordination from 4 to 5, 6, and occasionally 7. Second, these elements can engage in multiple bonding with "terminal" oxygen atoms due to their vacant and accessible d-orbitals. The most common environment in POMs is distorted octahedral with one or two terminal oxygen atoms. POMs are produced from their monovalent tetrahedral oxyanions via a Brønsted acid-base condensation process (Equation 1.1.).[33]

5

$$p\,\text{H}^+ + q\text{MO}_4^{r-} \leftrightharpoons [\text{H}_x\text{M}_q\text{O}_y]^{n-} + (4q - y)\text{H}_2\text{O}$$

Equation 1.1.
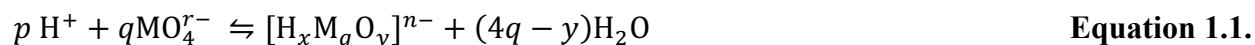
Heteroatoms can also be incorporated into POM structures. The most common heterpolyanions are of the Keggin-type, described by the general formula: $[\text{XM}_{12}\text{O}_{40}]^{n-}$ where X is the heteroatom (such as P, Si, Be, B, Al, Ge, Sn, Te, and all the first-row transition elements). Phosphorus forms more heterpolyanions than other heteroatoms, which is especially relevant given the high concentration of phosphorus in bone. V(V) can form various phosphovanadates at pHs from 1-10.[43]

1.2.2.3. Group 6: Chromium, Molybdenum, Tungsten

Chromium exists in solution as Cr(III), considered to be biologically safe, and Cr(VI), known to be biologically active under physiological conditions.[47] Molybdenum and tungsten are most stable in the +6 oxidation state.[5] The aqueous chemistry of Cr(III) is complex. At physiological pH, a number of mononuclear and polynuclear species are possible depending on metal concentration and pH.[5, 48] While mononuclear hydrolysis reactions occur rapidly, the formation of polynuclear species is limited by slow kinetics. In aqueous solution, Cr(III) exists as octahedral aqua ions, with $[\text{Cr}(\text{H}_2\text{O})_5(\text{OH})]^{2+}$ and $[\text{Cr}(\text{H}_2\text{O})_4(\text{OH})_2]^+$ the dominant mononuclear species at neutral pH.

Hexavalent Group 6 metals hydrolyze extensively.[5] At pHs greater than 7, chromium(VI), molybdenum(VI) and tungsten(VI) form tetrahedral monomeric oxometallates: chromate CrO_4^{2}, molybdate MO_4^{2-}, and tungstate WO_4^{2-}, respectively, as seen in Figure 1.3. Cr(VI) polyoxoanions are entirely based on tetrahedral CrO_4 species and effectively limited to $\text{Cr}_2\text{O}_7^{2-}$ and $\text{Cr}_3\text{O}_{10}^{2-}$.[49] On the other hand, Mo(VI) and W(VI) form POMs of mainly octahedral structure. The first POMs which form in aqueous solution are the heptametalates, paramolybdate and paratungstate-A, $\text{M}_7\text{O}_{24}^{6-}$. Paramolybdate becomes further protonated as the pH drops.[33] The hydrolysis behavior of the polytungstates is more complex than that of the polymolybdates. In more dilute and acidic solutions, paratungstate anions slowly disproportionate into WO_4^{2-} and the Keggin structure metatungstate, $\text{H}_2\text{W}_{12}\text{O}_{40}^{6-}$. Several other kinetically metastable species, including paratungstate-B $(\text{H}_2\text{W}_{12}\text{O}_{42}^{10-})$, may also be formed in aqueous solution. The distribution diagram in Figure 1.3. provides a simplified picture of polytungstate aqueous chemistry. In reality, analysis of

polytungstate equilibria is complicated due to the extreme range of rates observed, from rapid (seconds - minutes) to slow (hours -weeks).
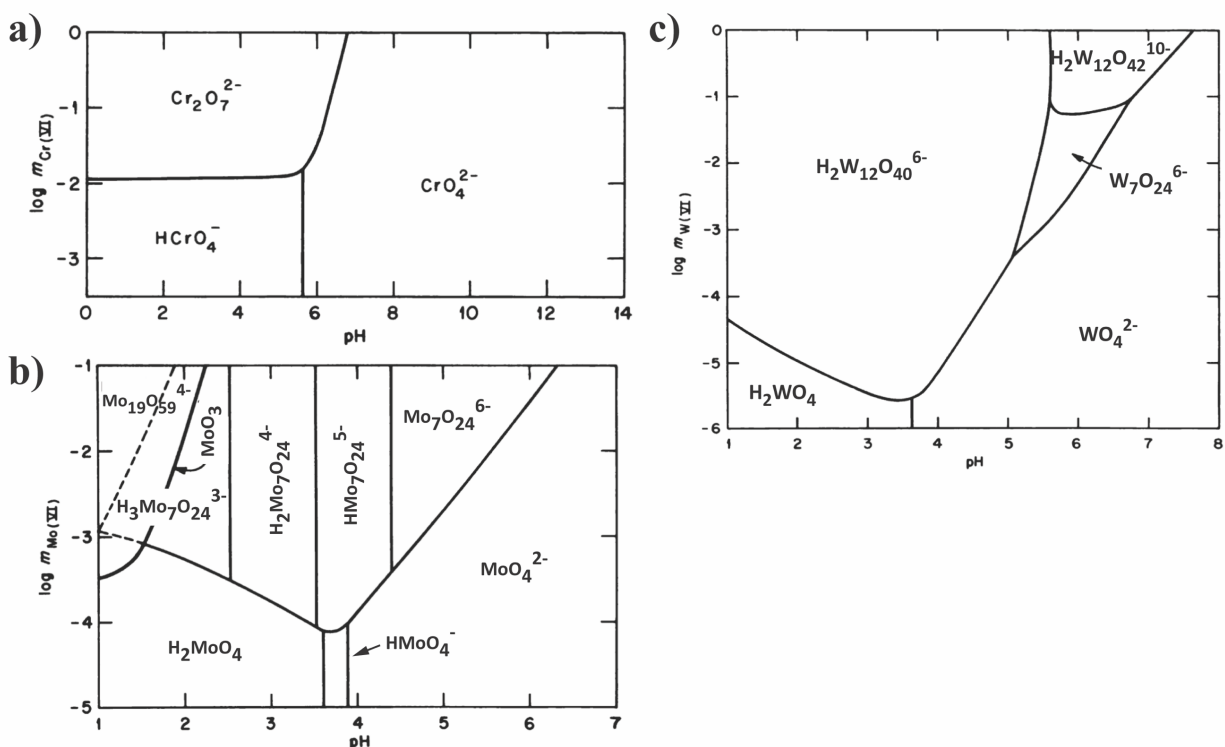
Figure 1.3. Predominance diagrams for a) chromium(VI) (25°C and I = 1 M), b) molybdenum(VI) (25°C and I = 3 M) and c) tungsten(VI) (50°C and I = 3 M). Solid lines represent the conditions at which the predominant species in adjacent regions have equal amounts of the metal atom. Based on images from Baes and Mesmer,[5] with updated species from Pope.[33]

Tungsten(VI) and molybdenum(VI) also readily form a number of heteropolyanions of phosphorus at acidic and neutral pHs. Phosphotungstate ($PW_{12}O_{40}{}^{3-}$) and phosphomolybdate ($PMo_{12}O_{40}{}^{3-}$) are particularly well-studied due to their stability in aqueous solutions and use in catalysis.[43, 50] Careful speciation investigations of phosphotungstates at physiological pH demonstrates that these species persist under biological conditions with detrimental consequences in plants and animals.[50]

1.2.2.4. Group 7: Manganese, Technetium, Rhenium

Manganese is most stable in the +2 oxidation state in aqueous solution at acidic and neutral pHs.[5] Rather than hydrolyzing, Mn(II) exists in solution as the manganous ion, Mn^{2+} at pHs less than 8. Species such as manganate(VI) ($MnO_4{}^{2-}$) and permanganate(VII) ($MnO_4{}^{-}$) are unstable in aqueous solutions at physiological pH.

The +7 oxidation state dominates the aqueous chemistry of technetium and rhenium.[5] Tc(VII) and Re(VII) form soluble pertechnetate (TcO_4^-) and perrhenate (ReO_4^-), respectively. These species are tetrahedral in aqueous solutions. There is no evidence of polymer formation in solutions of either Tc(VII) or Re(VII). A more in-depth discussion of Re and Tc speciation has been conducted by A.A. Haase *et al.*[19]

1.2.3. Bone Implants

One cannot discuss the interaction of ETMs in bone without mentioning their key role in bone implant materials. A full discussion on the composition, biocompatibility and mechanical requirements of current orthopaedic implants can be found elsewhere.[51, 52] In this section we will briefly describe the use of ETMs in bone implants. The distribution of these metals in bone following the leaching from bone implants is discussed in Section 4.2.

The primary materials currently used for implants include titanium and its alloys (with V, Zr, Hf, Nb, Ta, Mo), cobalt-chromium alloys, and stainless steel.[51] ETMs make particularly good implant materials due to their excellent biocompatibility, wear resistance, mechanical properties, and corrosion resistance.[53] Without a high corrosion resistance, metals can leach with high concentrations into the surrounding bone tissue, bloodstream, and/or other organs with toxic consequences. The corrosion mechanisms of metallic implants are discussed elsewhere.[54, 55]

Due to their corrosion resistance and biocompatibility, pure Ti and Ti-6Al-4V are the most commonly used titanium materials for implant applications.[51] The corrosion resistance of titanium alloys is strongly dependant on the alloying element and the oxides formed. The corrosion of Ti and Ti-6Al-4V is significantly reduced by the formation of a protective titanium-oxide (TiO_2) layer. However, this layer can be worn away through friction in moving joints, resulting in the release of Ti, Al and V ions and particles. The use of vanadium in Ti alloys is a source of concern, due to the known toxicity of some vanadium species.[56-58] To address these concerns, vanadium-free titanium implant alloys began development in the 1980s.[57] Of the early transition metals, zirconium,[59] hafnium,[60] niobium,[61] tantalum,[62] and molybdenum,[63] alone or in combination[64-70] have been used in titanium-alloy implants. Nb, Ta and Hf alloys stabilize the surface TiO_2 passive film through formation of stable Nb_2O_5,[51] Ta_2O_5,[62] and HfO_2[4, 71, 72] oxides, thus improving the corrosion resistance compared to Ti-6Al-4V.

Though stainless steel has a low wear resistance, its good mechanical properties, corrosion resistance and low cost continue its use as temporary implants.[53, 55] The only biocompatible type

of stainless steel (AISI 316L) contains 17-20% Cr, 13-15% Ni and 2-3% Mo, as well as a small amount of other metals.[24] Cobalt-chromium (Co-Cr) alloys have the strongest wear resistance compared to stainless steel and Ti-alloys.[73] They contain a cobalt base (~66%) with an additive of 26-30% chromium.[24] Other metals such as nickel (3-5%) and molybdenum (4-5%) are also incorporated. Tungsten has been considered as an addition to Co-Cr alloys in some limited situations and has exhibited good corrosion resistance and biocompatibility.[74, 75] In both stainless steel and Co-Cr alloys, chromium serves to increase the hardness and corrosion resistance by forming a thin passivation layer of Cr(III) oxide, Cr_2O_3.[24]

1.3. Bone Composition and Remodeling

1.3.1. Introduction to Bone

Bone is a dynamic, highly vascularized tissue composed of $50 - 70\%$ inorganic apatite $[Ca_{10}(PO_4)_6(OH)_2]$, $20 - 40\%$ organic matrix (90% collagen), $5 - 10\%$ water, and <3% lipids.[76, 77] Bone serves many key biological functions beyond structural support, including protection of vital organs, mineral storage and homeostasis, and supporting hematopoiesis.[77, 78] Bone undergoes a constant process of remodeling in order to repair microdamage and regulate calcium ion concentration. The two cell types involved in this process are osteoclasts and osteoblasts, which are responsible for resorbing old bone and the formation of new bone, respectively.[79]

There are two forms of bone tissue: cortical bone (80%) and trabecular (or cancellous) bone (20%).[80] Both forms have the same matrix composition, though cortical bone is much denser than trabecular bone. In the long bone, cortical bone surrounds the marrow space and the trabecular bone. Trabecular bone is significantly more porous than cortical bone, with a honeycomb-like structure.[81] The proportions of cortical and trabecular bone vary depending on the location in the skeleton.

Long bones, such as the femur, are divided into three physiological sections: the diaphysis, metaphysis, and epiphysis (Figure 1.4.). Cortical bone forms the thick walls of the diaphysis but thins and increases in diameter into the metaphysis and epiphysis. The metaphysis and epiphysis contain a greater fraction of porous trabecular bone. In terms of cortical to trabecular ratio, the diaphysis is primarily composed of cortical bone (95:5), whereas the metaphysis and epiphysis have a higher amount of trabecular (50:50), being composed of a trabecular meshwork within a thin cortical shell.[77]
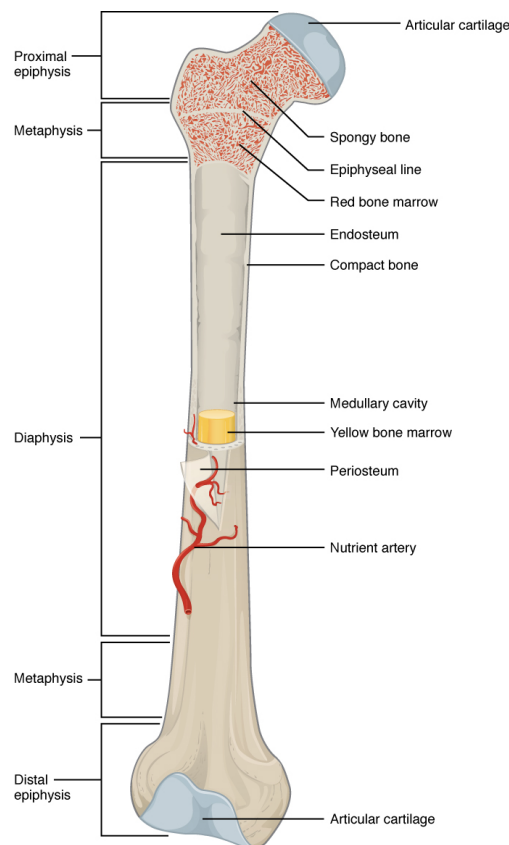
Figure 1.4. Anatomy of a femur.[82]

To provide the basis for discussion surrounding the deposition of the early transition metals in bone, the following sections will discuss topics of bone composition and remodeling in more detail. Other important aspects of bone biology including bone formation, differences in woven and lamellar bone, and hierarchical organization are not included here but are thoroughly described in the literature.[83-87]

1.3.2. Inorganic Matrix: Apatite

Apatite, the inorganic matrix of bone, provides bone most of its stiffness and strength as well as serving as an ion reservoir.[80] This material has been the source of considerable study on topics including biomineralization[88] and synthetic bioactive materials.[89, 90] Besides natural formation, apatites can also be produced synthetically via several routes, including precipitation, sol-gel, hydrolysis and hydrothermal methods.[91, 92] Hydroxyapatite, $[Ca_{10}(PO_4)_6(OH)_2]$, is often chosen as the synthetic analogue to biological apatite, due to its crystallographic similarity.[93] Hydroxyapatite crystalizes as the hexagonal $P6_3/m$ space group, with the unit cell containing two non-equivalent calcium sites, Ca_I and Ca_{II} (Figure 1.5.).[94] Ca_I is coordinated by nine oxygen atoms

whereas Ca$_{II}$ is coordinated to seven oxygen atoms, leading to a smaller overall polyhedron volume.[7, 95]
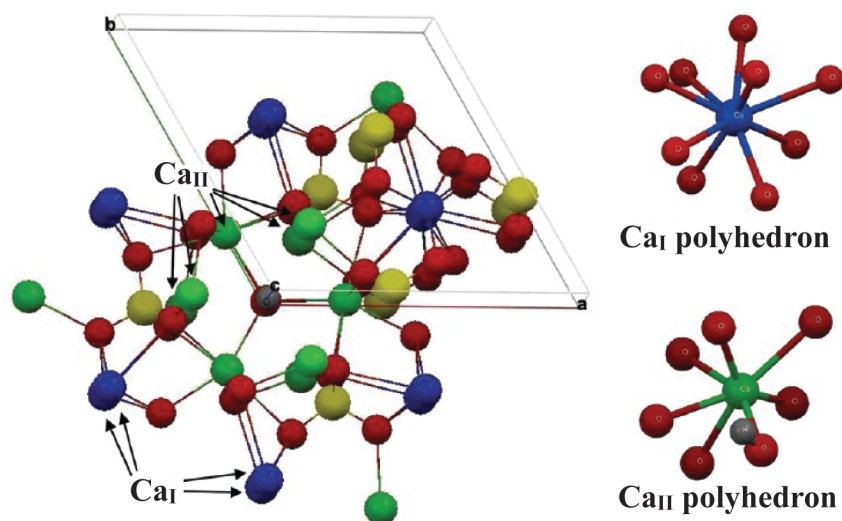
Figure 1.5. Hydroxyapatite crystal lattice and Ca$_I$ and Ca$_{II}$ polyhedrons. Reprinted with permission from ref.[7] Copyright 2012 American Chemical Society.

Unlike synthetic hydroxyapatite, biological apatite contains significant amounts of carbonate (CO_3^{2-}) ion, which substitute into the PO_4^{3-} sites (type B carbonated apatite) and OH^- sites (type A carbonated apatite).[96] Furthermore, biological apatite can also contain hydrogen phosphate ions (HPO_4^{2-}) ions in PO_4^{3-} sites.[97, 98] The present of the bivalent CO_3^{2-} and HPO_4^{2-} in PO_4^{3-} sites corresponds to the formation of calcium deficient, or non-stoichiometric, apatite characteristic of bone mineral.[99] Other trace elements known to substitute into the crystal lattice of bone apatite include chloride or fluoride ions into the OH^- sites and magnesium, strontium, barium, zinc, iron, lead, and aluminum ions into the calcium sites.[100-104] Incorporation of these elements within apatite can affect the dimensions of the unit cell.[105]

Depending on lattice distortions from substituted ions and/or bone maturity, the crystal lattice of bone apatite can range from amorphous to crystalline.[105, 106] Overall, the degree of crystallinity increases with bone age.[107, 108] Crystal size can also vary for biological apatite, with bone mineral comprised of apatite nanometric crystals with a high surface area.[99] Bone crystals' high surface area is essential for bone's ion reservoir and homeostasis functions, since it allows for the rapid exchange of ions at the bone surface or in the hydration shell of the crystals.[109]

1.3.3. Organic Matrix

Bone is composed of a number of biomacromolecules which serve various functions in bone (Table 1.2). Collagen, predominately Type-I collagen, makes up 85-90% of bone tissue.[77] Collagens are proteins composed of the amino acids, primarily glycine, proline, and hydroxyproline arranged as Gly-X-Y repeats and folded into a triple-helical structure.[110] Type-1 collagen provides much of the structural integrity in connective tissues in the human body, particularly in bone, tendons and ligaments.[111, 112]

The organic matrix of bone also consists of 10-15% non-collagenous proteins. [77] Key non-collagenous proteins include osteocalcin,[113] osteonectin,[114] osteopontin,[115] bone sialoprotein,[116] and alkaline phosphatase.[117] Though the roles of each of these proteins is not well-defined, they are known to serve several functions including influencing the organization of the matrix, the mineralization of the bone, and the behavior of bone cells. Known functions are summarized in Table 1.2.

Protein	Function
Type-I collagen	Structural flexibility
Osteocalcin	Regulates osteoclasts; inhibits mineralization
Osteonectin	Inhibits mineralization
Osteopontin	Inhibits mineralization and remodeling
Bone sialoprotein	Initiates mineralization
Alkaline phosphatase	Hydrolyzes mineral deposition inhibitors

Table 1.2. Major bone macromolecules

1.3.4. Bone Cells and Remodeling

Osteoclasts, osteoblasts, bone-lining cells, and osteocytes are the four cells essential for carrying out bone remodeling.[80] Bone remodeling is the continual, lifelong process in which bone is renewed to maintain bone strength and mineral homeostasis.[118] The coordinated action of the four bone cells carry out this process and together form the basic multicellular unit (BMU).[119, 120] Remodeling occurs in four sequential phases: Activation, resorption, reversal, and formation.

During activation, mononuclear osteoclast precursors are recruited and activated, bone-lining cells are lifted off the surface, and multinucleated preosteoclasts are formed.[121] Bone lining cells are flat cells which lie directly against the bone matrix in non-remodeling locations.[118] Though the function of these cells is not fully understood, it has been shown that bone lining cells produce collagenase, which digests the layer of unmineralized matrix on the bone surface, exposing it to osteoclasts for bone resorption.[122]

Bone resorption is mediated by osteoclasts.[123, 124] As seen in Figure 1.6., the cell membrane first forms a ruffled border at the bone surface, creating a sealed zone between the cell and bone matrix.[125] The osteoclasts then secrete hydrogen ions into the sealed zone, lowering the pH to ~4.5, which helps mobilize bone mineral.[25] The organic portion of the bone is then degraded by secreted proteases.[126] After matrix degradation, organic and inorganic resorption products are transported through the cell and liberated into the extracellular space.[127]
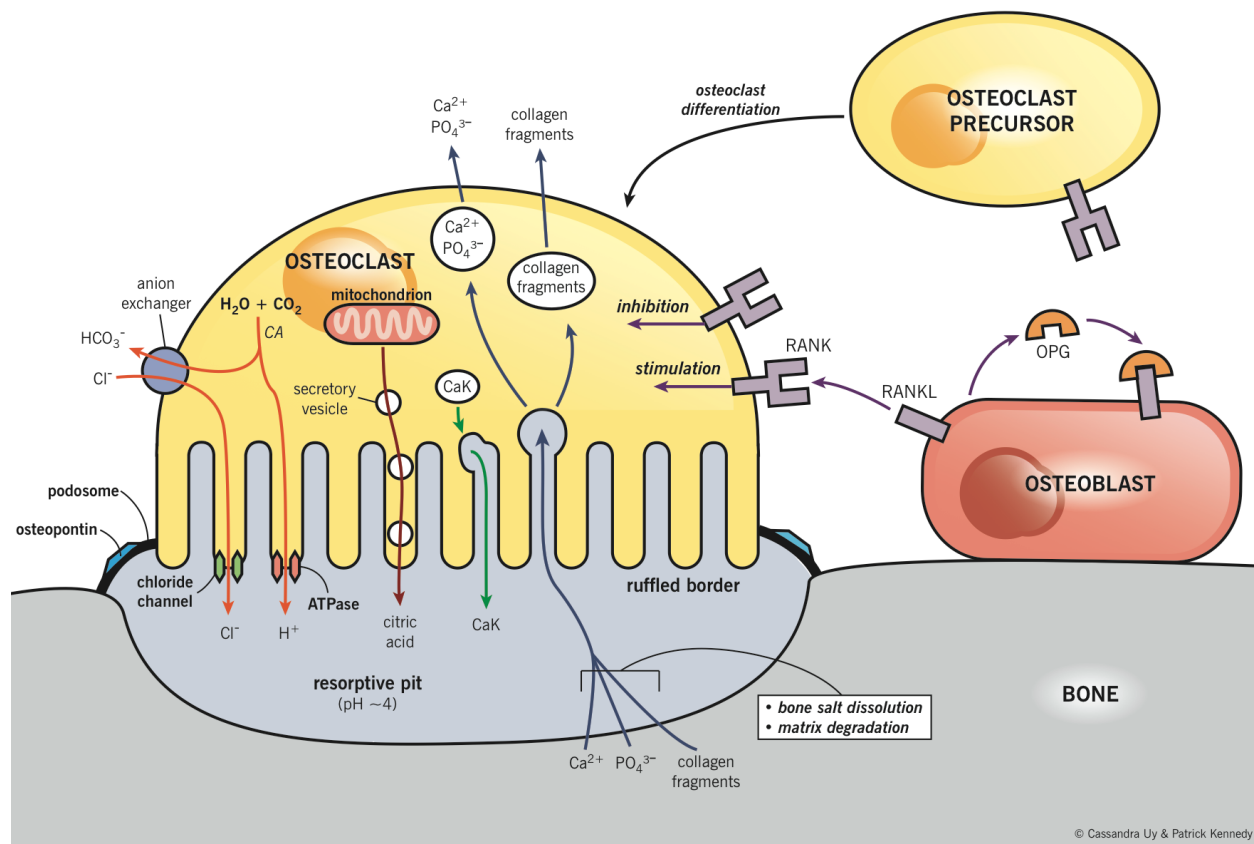
Figure 1.6. Bone resorption by osteoclasts. CaK = cathepsin K, CA = carbonic anhydrase. RANK = receptor activator for nuclear factor κB, RANKL = RANK ligand.[128]

Resorption is followed by a short reversal phase, in which bone resorption transitions to bone formation.[129, 130] During this phase, osteoclasts stimulate differentiation of osteoblast precursors, activating bone formation. Simultaneously, bone resorption is halted as osteoclasts undergo apoptosis due to high extracellular calcium concentration.[131] The coupling signals linking the end of bone resorption to the beginning of bone formation is currently unknown, though several candidates have been suggested.[130, 132, 133]

Osteoblasts are the bone cells responsible for bone formation through the secretion of the organic components of the bone matrix.[134] Once they differentiate from their precursors, osteoblasts begin to secrete collagenous and non-collagenous proteins which fill the resorption pits left by osteoclasts. Osteoblasts also indirectly aid in bone matrix mineralization.[135] Key candidates for the initiation of apatite crystal formation are osteoblast-derived. Furthermore, osteoblasts may regulate mineralization by releasing small, membrane-bound matrix vesicles that concentrate calcium and phosphate and destroy mineralization inhibitors.[136] At the completion of bone formation, the majority of osteoblasts undergo apoptosis. Those that do not, become either osteocytes or bone-lining cells.[134] Osteocytes are bone cells embedded into the bone matrix, forming a network with neighboring cells.[137] These cells are increasingly considered to maintain the balance between osteoclasts and osteoblasts and, thereby, moderate bone remodeling.[137-139]

1.4. Early Transition Metal Distribution in the Skeleton

Bone is one of the main target organs for ETMs. Their deposition patterns in the skeleton may differ depending on animal model, mode of exposure and metal speciation and complexation. Understanding specifics of ETM distribution in bone can provide valuable information about uptake mechanism as well as where these metals may be poised to interact with key biological function. In this section, we distinguish between two categories of metals. First, the deposition in bone resulting from external exposure to metallic compounds (metals, oxides, or salts). Second, internal exposure from metal leachate or wear particles from bone implants.

1.4.1. The Case of Metallic Compounds

The International Commission on Radiological Protection (ICRP) has compiled metabolic data on all the elements in 1975, including the early transition metals.[6] With this data, they developed biokinetic models to enable a dose assessment after exposure to radionucleotides. These models predict the biodistribution and retention of these elements in the whole body. Biokinetic information is based on the behavior of internally deposited elements in human and animal subjects. Since 1975, the ICRP has regularly updated systematic biokinetic models for the Period 5 transition metals (Zr, Nb, Mo, Tc) with the most recent update in 2016.[140] Herein, we will limit our discussion to the distribution of the ETMs in bone. A complete overview of each metal's metabolic data is provided by the ICRP.[141-152]

1.4.1.1. Group 4: Titanium, Zirconium, Hafnium

The biokinetic data for the Group 4 metals has been thoroughly reviewed by Leggett and Samuels.[153] As indicated in their review, the biokinetics of Zr have been extensively explored by the ICRP,[140] but are significantly limited for Ti and Hf. For this reason, the biokinetic models for Ti and Hf are largely based on comparison of their element-specific information and corresponding data for their chemical analogue Zr.

Bone is a long-term reservoir of labile ^{44}Ti after administration of ^{44}TiCl$_4$ and [^{44}Ti]ammonium oxalotitanate in lambs and rats, respectively.[154, 155] Further studies on hamsters demonstrate that Ti accumulates in both the mineralized and demineralized portions of bone.[156] The distribution of Ti in these studies resembles those predicted by the systematic model for Zr.[153] Zhu *et al.* found a considerable difference, however, in the distribution of long-term Ti and Zr tissue deposits obtained from autopsies of 68 Chinese men.[157] Whereas the median concentration of Zr in bone was greater than in soft tissues in these samples, the opposite was true for Ti. Beyond labile Ti, the biokinetics of TiO$_2$ nanoparticles have been thoroughly studied due to their role in numerous commercial applications and as debris from titanium based implants.[158] After intravenous,[159] oral,[160] and intratracheal[161] exposure to TiO$_2$, Ti accumulated and was retained in soft tissue, followed by bone. In summary, the initial distribution of Ti and Zr are similar at early time points after exposure but exhibit significant differences in long-term behavior. [156]

Distribution studies of Zr have primarily focused on ^{89}Zr, an emerging radiopharmaceutical for positron emission tomography (PET) and ^{95}Zr, an important fission product. [149, 162, 163] These studies suggest that weakly chelated ^{95}Zr and ^{89}Zr have a high affinity and retention in bone. More specifically, Abou *et al.* found that Zr accumulates in the mineralized fraction of bone, with high uptake observed in the epiphysis and none observed in bone marrow.[163] Several studies have looked at the distribution of ^{95}Zr and ^{95}Nb simultaneously, since ^{95}Zr ($t_{1/2}$ = 65 days) decays into ^{95}Nb ($t_{1/2}$ = 35 days).[164] The distribution of both radioisotopes was similar, with high accumulation being observed in bone for ^{95}Nb as well as ^{95}Zr.[164-166]

Comparison of Zr and Hf data indicates that Hf is a close physiological analogue of Zr, likely due to their exceptionally similar chemical and physical properties.[153] Both metals have almost identical total-body retention curves. Ando and Ando investigated the biokinetics of ^{181}Hf and ^{95}Zr and found the kinetics for Hf closely followed Zr in bone with bone as the dominant repository for Hf at 24 and 48 h.[167] Studies by Taylor *et al.*, also found that the skeleton was the

main reservoir for Hf in rats and hamsters.[168, 169] Because of the similarity between Hf and Zr, Leggett and Samuels proposed that the biokinetic model for Zr be applied to Hf as well.[153]

1.4.1.2. Group 5: Vanadium, Niobium, Tantalum

Similar to the Group 4 elements, biokinetic data for the Group 5 metals has been thoroughly reviewed by Leggett and O'Connell.[170] The discussion in their review revolves around the comprehensive report of Nb biokinetics by the ICRP.[140] Group 5 metals have similar chemical properties, though V has a much smaller ionic radii than Nb and Ta.[170] Furthermore, while Nb and Ta exist primarily in the +5 oxidation state under physiological conditions, V has a much more complex biological chemistry. In nature, V exists in several valance states, the most common being +3, +4, and +5.[171] Pentavalent forms (VO_3^-, VO_4^{3-})$^-$ are the most common in extracellular body fluids and quadrivalent forms (VO^{+2}) the most common intracellularly.

It can be difficult to compare the metabolism, distribution, incorporation into bone, and biological effects of vanadium due to the many different chemical forms and oxidations states this metal can achieve. Regardless of speciation, several studies demonstrate that vanadium accumulates primarily in bone after 24 h.[172, 173] Both uncomplexed and complexed vanadyl(IV) (VO^{2+}) species result in V deposition in bone.[174, 175] Furthermore, many V(V) species including metavanadate (VO_3^-),[174] vanadium oxychloride ($VOCl_3$),[176-178] and vanadium pentoxide (V_2O_5)[156, 179] also exhibit high uptake and retention of V in bone regardless of administration method. Vanadium is found in both the mineralized and demineralized fractions of bone.[156] Significantly higher concentrations of V were found in young rats compared to adult rats, with greater deposition in areas of recent bone formation.[179, 180] In summary, biokinetic data for V indicates that V, like Nb, is a bone-seeking metal. However, long-term data suggests that V has significantly shorter retention times in bone compared to Nb or Ta.[157, 181] Because of this, the biokinetic model for V only includes bone surfaces, and assumes that V is not transported and retained by the bone volume.[170]

The biokinetics of Nb have been thoroughly described by the ICRP.[140] Distribution studies have primarily followed [95]Nb, a high yield fission product. [95]Nb arises as the progeny of [95]Zr and many studies measure their distribution simultaneously. Nb shows similar systemic behavior to Zr,[164-166] though with a lower rate of transfer to bone. Nb oxalate is the most common form of Nb used in distribution studies as it is relatively soluble in biological fluids.[140] Studies suggest that the systematic behavior of Nb does not depend strongly on the mode of intake or the species of the

subject.[182] Studies of [95]Nb and [90]Nb distribution found that bone and bone marrow are some of the target organs for these isotopes after inhalation[183] and intravenous exposure.[184, 185] Because of its increased retention in bone compared to other tissues, as time passes bone contains increasingly higher percentages of Nb (~27% of injected amount).[182, 186] Autoradiographic studies indicate Nb deposits in bone are retained primarily on the bone surface.[187] Studies by Mraz and Eisele show that Nb accumulates more in the bones of young animals demonstrating that Nb, like many bone-seeking metals, has higher uptake in the bones of growing mammals.[188, 189] However, if Nb is stabilized in a complex, such as Nb labelled antibody [95]Nb-bevacizumab, negligible uptake is found in bone, indicating the promising application of these compounds in PET applications.[185] The ICRP's biokinetic model for Nb predicts that the Nb present in the bone surfaces is equally divided between cortical and cancellous bone.[140] The percentage of uptake is predicted to increase for children and infants.[170] Nb depositing at bone surfaces is either buried in bone volume or returns to blood at a rate proportional to the rate of bone turnover, which differs for cortical and cancellous bone.

The biokinetic model for Nb can be applied to Ta given their chemical similarities,[170] similar behavior in rats,[190, 191] and nearly identical radii in their pentavalent state, the most common oxidation state for both Nb and Ta in naturally occurring compounds.[192] Ando *et al.* studied the distribution and excretion of Nb and Ta following intravenous administration of [95]Nb oxalate and [182]Ta oxalate to tumor-bearing rats and found that the behavior of Ta closely followed that of Nb in bone and other tissues.[190, 191] Fleshman *et al.* observed that, when soluble [182]Ta was administered orally to rats as potassium tantalate (TaO_3^-), the majority of absorbed Ta, over 40% of the total body burden, is deposited and retained in bone.[193]

1.4.1.3. Group 6: Chromium, Molybdenum, Tungsten

The two most biologically relevant oxidation states for chromium are Cr(III) and Cr(VI).[194] Cr(VI), known as the toxic Cr species, is generally bound to oxygen as chromate (CrO_4^{2-}) or dichromate ($Cr_2O_7^{2-}$). In the body, Cr(VI) is reduced to Cr(III) shortly after administration. Cr(III) has traditionally been thought of as an essential nutrient for humans and not toxic.[195] Several studies demonstrate that Cr is deposited and retained in bone after administration of either Cr(III) or Cr(VI).[196-201] Distribution in bone was observed as heterogeneous, with highest uptake in the epiphyses.[200] Uptake is further influenced by age, with young mice accumulating more Cr over time and older mice acquiring a smaller fraction that did not increase with time.[197] Accumulation

in the bone marrow has also been observed.[202] In a long-term distribution study by Zhu *et al.*, bone is found to contain about 26% of systematic Cr content.[157] After analysis of the available data, biokinetic models for Cr(III) and Cr(VI) exposure include bone as a significant repository for Cr.[194, 203, 204] Uptake and loss of Cr by bone are predicted to be linked to the age-dependant rate of bone turnover.

There are conflicting reports about whether bone is a depositing organ for Mo. The ICRP previously identified the skeleton as a deposition organ,[205] however, this was based on a review that did not measure Mo in bone directly.[206] Alternatively, Schroeder *et al.*[207] and Sumino *et al.*[208] did not detect Mo in human bone samples, while Yoo *et al.*[209] reported mean concentration Mo in bone of 0.09 μg/g, which is comparable to the value found in other low accumulation organs. Animal studies where high concentrations of molybdenum were administered to rats[210, 211] and cows[212] found that Mo accumulated in bone at levels comparable to other organs. This data indicates that the skeleton is not a major repository for Mo and thus, in the most recent ICRP biokinetic model (2016), the skeleton is pooled together with the rest of the organs which show non- specific Mo uptake.[140]

A biokinetic model for tungsten has been described by Leggett.[213] A number of studies confirm that, after oral and intravenous exposure to dissolved Na_2WO_4, the major site of long-term tungsten retention is generally bone.[143, 214-217] Kelly *et al.* demonstrates that oral exposure to Na_2WO_4 resulted in rapid bone accumulation within 1 week and reached almost maximal concentrations by 4 weeks.[218] Accumulation of tungsten is also greater in growing bone than mature bone.[217]

The lack of Mo uptake in bone is interesting considering the observed accumulation of tungsten, a close chemical analogue of Mo. W is known to replace Mo in some enzymes, suggesting that these metals have similar biological modes of action.[219] Perhaps explaining this disparity, an autoradiography study of [99]Mo distribution in bone demonstrated that Mo accumulates in the mineralizing tissues in the developing teeth and bone of young rats.[220] Given the report that tungsten accumulation in bone is much higher in young mice than mature animals,[217] this may suggest that accumulation of Mo in bone is dependent on bone remodelling. More data is needed to fully understand the observed difference in uptake for Mo and W.

1.4.1.4. Group 7: Manganese, Technetium, Rhenium

Bone is one of the long-term storage organs of Mn in the human body, holding approximately 40% of the total body Mn burden.[6, 221-223] Animal studies demonstrate that Mn is retained in bone longer than other organs. Using orally administered radioactive ^{54}Mn in rats, Furchner *et al.* demonstrates that the half-life of Mn in bone is 50 days, much longer than other tissues.[224] O'Neal *et al.* found that, after chronic oral exposure, Mn concentrations in bone reached a steady state after 6 weeks with an average half-life of 143 days.[225] Studies of fox bone samples found that Mn concentrations were highest in compact bone > compact bone and cartilage > cartilage > spongy bone.[226] Alternatively, when measuring the Mn content in hip joints from patients about to undergo their first hip-replacement surgery, Brodziak-Dopierala *et al.* found Mn content, from highest to lowest: articular cartilage > cancellous bone > joint capsule > cortical bone.[227] This data is incorporated into the biokinetic model proposed by Leggett,[228] which predicts that Mn deposits evenly on cortical and cancellous bone surfaces. Mn activity leaves bone surfaces with a half-time of 40 days, with 1% of the activity transported and retained in the bone volume.

Biokinetic studies of technetium usually involve its administration as pertechnetate (TcO_4^-), the form which dominates in aqueous environments such as body fluids.[229] Tc, unlike the other early transition metals, is not considered a bone-seeker and its distribution is more similar to inorganic iodide. Most studies of Tc distribution in humans and animals have not reported any bone uptake.[140, 230] However, some reports do find Tc uptake in bone, albeit at a significantly lower concentration than most soft tissues.[231-233] Holm and Rioseco investigated the transfer of ^{99}Tc from lichens to reindeer and found relatively high concentrations of Tc in bone, evenly distributed between cortical and cancellous bone.[234] Due to this data, the ICRP (2016) biokinetic model for Tc depicts a low rate of uptake of Tc, but predicts that, in cases of chronic exposure, bone contains a significant portion of the total body burden given the long-term retention of the small portion of deposited Tc.[140]

Rhenium has very little biokinetic data, especially in regard to bone uptake.[146] The ICRP thus predicts that the metabolism of Re is similar to Tc. A report by Zuckier *et al.* demonstrates that $^{99m}TcO_4^-$ and $^{188}ReO_4^-$ had remarkably similar distribution in mice, with no specific bone uptake observed.[235]

1.4.2. The Case of Implant Materials

The release of particles/ions from implants into the surrounding tissue and ultimate biodistribution in the body lay at the center of biocompatibility and biokinetic studies. A comprehensive review of the *in vivo* release of trace metals from metallic implants in the human body is provided by Matusiewicz.[24] For the purposes of this review, we will focus on metal release from orthopedic implants into local bone environment.

Matsuno *et al.* implanted pure Ti, Nb, Ta and Re wires in the femoral bone marrow of rats.[4] No dissolution from the implants into the surrounding hard tissue was evident after 4 weeks, indicating the biocompatibility of these materials. Similarly, negligible metal leaching or debris were found after 8 weeks in a comparative study of Ti and Zr implants.[236] Despite the corrosion-resistance demonstrated by these studies, the release of metal ions or high surface area nanoparticles have been shown at longer exposure times and/or following wear damage.[237] Studies on humans at retrieval of failed total joint replacements demonstrate high accumulation of titanium in the surrounding soft tissue, serum, synovial fluid, and synovial tissue.[238-241] Distribution into the bone itself appears to be limited, with small titanium deposits in about 5% of the bone surrounding the implant.[53, 242-244] ZrO_2 wear particles have been observed in peri-implant soft tissues after degradation of Zr-containing bone cement, which contribute to the observed inflammatory tissue response.[245]

Vanadium is present in small amounts at the surface of Ti-6Al-4V bone implants as V_2O_5.[246] $H_2VO_4^{2-}$ ions are known to release from the implant surface due to the solubility of V_2O_5.[31] However, modelling suggests that V(V) species may convert to V(IV) species in the synovial fluid surrounding the joint and bind to human serum albumin. With no evidence of V accumulation in bone from V-containing alloys,[242, 244] it is likely that V ions released from bone implants remain in the synovial fluid or bind to human transferrin in blood serum and are transported out of the joint.[31] Further studies on other common Ti-alloy metals such as Zr, Hf, Nb, and Ta are still needed to understand their distribution and potential impact in bone upon implant failure.

Ektessabi *et al.* used synchrotron radiation micro X-ray fluorescence (SR-µXRF) to observe the accumulation of Cr in the tissue surrounding a failed stainless steel hip implant.[247] Brodziak-Dopierala *et al.* analyzed the Cr content in 91 samples of human hip joint tissues following joint replacement and found an average of 17.86 µg/g in the cancellous bone, 5.73 µg/g in the articular cartilage, 5.33 µg/g in the cortical bone, and 1.28 µg/g in the joint capsule.[248] The

highest amount of Cr was found in the cancellous bone, the most metabolically active type of bone tissue.

Mo can also be present in periprosthetic tissues due to corrosion and/or wear of Mo-containing bone implants.[249] Elevated Mo concentrations in the synovial fluid and joint capsule has been observed in subjects with Mo-containing CoCr alloys hip implants.[250]

1.5. Interaction Mechanisms of Early Transition Metals with the Bone Matrix

As described in Section 1.4., ETMs show marked affinity for bone. Both organic and mineral components of bone can contribute to metal binding interactions on the molecular level.[7] Furthermore, metal interaction with bone is highly dependant on metal speciation. The aqueous chemistry of ETMs is complex, and the local *in vivo* environment can drastically affect metal speciation and oxidation state.[24] Metal speciation can be difficult to determine *in vivo* since metal levels are often extremely low. Given the complexity of bone tissue and the number of possible chemical interactions with metal ions, unravelling the nature of *in vivo* binding can be challenging. To circumvent the difficulties of *in vivo* investigations, many studies utilize either model systems with synthetic hydroxyapatite (HAP) or *in vitro* methods.

1.5.1. Organic Matrix

Several different studies show that ETMs bind to the organic matrix of bone. Merritt and Brown demonstrate that titanium and vanadium deposit in both the mineralized and demineralized portions of bone.[156] Vanadyl(IV) (VO^{2+}) associates with chondroitin sulfate A, an acid mucopolysaccharide present in connective tissues, by coordinating to the carboxylate group and the glycosidic oxygen of the D-glucuronate moieties.[251, 252] Doi *et al*. demonstrate with electron spin resonance (ESR) that chromium(III) associates with the organic component of bone.[253] Small amounts of molybdenum (1.2%) and tungsten (0.6%) firmly bind to collagen.[254-256] Hart *et al*. found Mo in periprosthetic organic tissue, with XAS analysis indicating that Mo exists as an octahedral coordinated Mo(VI) species bound by oxygen and then carbon in the second coordination sphere, which likely represents organic carbonyl ligand binding to Mo.[249] Mn accumulates in the articular cartilage of hip joints,[227] which Kusaka *et al*. hypothesized is due to the electrostatic interaction between positive Mn cations with the negatively charged groups of proteoglycans in the cartilage matrix.[257]

To our knowledge, these are the only studies which discuss the interaction between ETMs and organic components of bone. These studies suggest that a small, though significant percentage of ETMs accumulation in bone is due to bonding to the organic components of bone. More rigorous and methodological work is required to untangle the relative contribution of the organic matrix to the overall binding of metals in bone as well understanding the binding mechanism in relation to metal speciation.

1.5.2. Inorganic Matrix

There are few studies which investigate the interaction of metals within the apatite matrix of bone directly due to the complex nature of bone tissue. Bone mineral is a non-stoichiometric poorly crystalline carbonated apatite with a hydrated amorphous layer present at the surface.[99, 258, 259] A commonly accepted mechanism for the uptake of ions into bone involves diffusion from blood plasma into the amorphous layer of bone followed by further diffusion into the bone apatite crystal.[260] More specifically, as demonstrated in Figure 1.7., this uptake can occur via chemical complexation and surface sorption on the mineral surface, ion-exchange with calcium or phosphate in the amorphous layer and/or crystalline apatite, and precipitation of a poorly soluble compound.[260-262]

Because the amorphous layer of bone is labile, it is difficult to analyze or model directly.[260] Consequently, understanding the interaction mechanisms of metals with bone often relies on synthetic HAP models. Several methods to prepare HAP are known, including dry, high temperature, and wet methods such as chemical precipitation.[91, 263] Our discussion of the early transition metals interaction with synthetic HAP will be limited to those prepared using the precipitation method. This method is more bio-mimetic than solid-state procedures since the metals are introduced as HAP precipitates out from aqueous solutions containing calcium and phosphate, though at a pH which is likely more basic (~10) than reasonable under local bone conditions.[264] While the mechanistic conclusions from synthetic HAP studies can be useful for understanding metal interaction with bone mineral, it is important to note that these studies are often not conducted under physiological conditions and, thus, conclusions may not be biologically relevant.
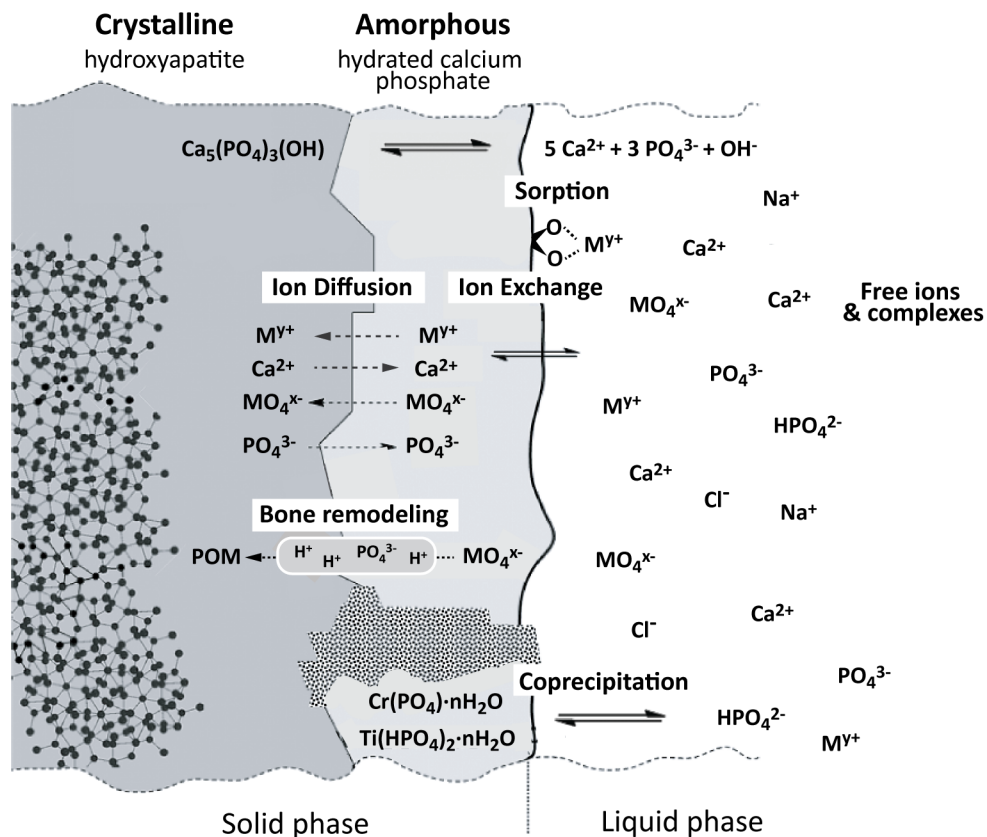
Figure 1.7. General mechanisms for metal uptake into bone, with focus on early transition metal elements.

Synthetic studies indicate that some ETMs may incorporate into the HAP by substituting the Ca^{2+} ions in the HAP lattice. Only small, positive cations are likely to substitute calcium in the apatite lattice.[265] When synthetic HAP is doped with Group 4 metal ions, its lattice parameters decrease in the a-axis and c-axis, indicating the substitution of the smaller Ti^{4+}, Zr^{+4}, and Hf^{+4} ions into the calcium sites in HAP, likely in the Ca_I site which is aligned and parallel to the c-axis. [266-269] Similarly, experiments incorporating Cr(III) into synthetic HAP demonstrate that Cr^{3+} substitutes into both Ca sites in HAP.[270] Characterization of Mn(II) doped HAP with electron paramagnetic resonance (EPR), IR, and XRD demonstrate that Mn^{2+} substitutes into both the Ca_I[271-273] and/or Ca_{II} site[274-278] in HAP. In ion-exchange synthesis methods, Mn^{2+} and Ca^{2+} ions exchange at the HAP surface.[279]

An alternative uptake mechanism proposed for the ETMs in bone is substitution for PO_4^{3-} ions in HAP. Other oxyanions such as arsenate (AsO_4^{3-})[280, 281] and carbonate (CO_3^{2-})[96] are known to incorporate into HAP through this mechanism. As described in Section 2.2. and shown in Table 1.1., most of the early transition metals exist as monovalent oxyanion $H_xMO_4^{y-}$ species in aqueous

23

solution at physiological pH, not cations. With this understanding of tungsten's chemistry, Fleshman *et al.* proposed that WO_4^{2-} accumulates in bone by substituting or replacing phosphate in apatite.[282] Studies demonstrate that V(V) oxides incorporate into HAP by substituting the phosphate groups for tetrahedral VO_4^{3-} species. [283-286] Similarly, synthesis of niobium[287, 288] and tantalum[289] doped-HAP increased HAP's lattice parameters, indicative of phosphate substitution with a larger niobate ($Nb_xO_y^{z-}$) and tantalate ($Ta_xO_y^{z-}$) species.

Discussing the implications of synthetic studies requires a robust understanding of ETM aqueous chemistry under physiological conditions. Most synthetic HAP prepared via the precipitation method were conducted at high pH, resulting in metal speciation different from that under biological conditions. The aqueous chemistry of Group 5 and 6 metals is particularly complex and very sensitive to pH and metal concentration. While synthetic studies observed uptake of niobium and tantalum oxyanions into the phosphate sites of HAP, these studies were conducted under basic conditions (pH > 10).[287-289] Niobium and tantalum form soluble oxyanions ($M_xO_y^{z-}$) in alkaline solution, while at neutral pHs they form sparingly soluble pentoxides, Nb_2O_5 and Ta_2O_5.[38, 39] Whether oxyanion $M_xO_y^{z-}$ species or pentoxide M_2O_5 species dominate under physiological conditions is unclear.[290] The different chemistry of these species may result in very different uptake mechanisms in bone.

The speciation of V(V) oxides is also highly pH and concentration dependant.[285] While VO_4^{3-} is the prominent species at high pH's, at physiological pH (7.4) $H_2VO_4^-$ or POM species can dominate depending on metal concentration (Figure 1.2.).[33] Kalnina *et al.* synthesized vanadium-doped HAP using a bio-mimetic approach at physiological pH with ammonium metavanadate(V), NH_3VO_3, as the vanadium source.[291] Using X-ray absorption near edge spectroscopy (XANES), they found that the V centers in the V-doped HAP no longer had tetrahedral geometry, but more closely resembled five-coordinate systems. The data is consistent with a partial replacement of the PO_4^{3-} by VO_4^{3-} within the HAP lattice, with an additional long V(V)-OH$^-$ bond to a HAP OH$^-$ anion.

If a metal has more than one accessible oxidation state in solution, untangling various aspects of its bone uptake mechanism becomes even more challenging. Vanadium readily exists in +4 and +5 oxidation states in solution, with both demonstrating very different uptake mechanisms. Whereas vanadate(V) is predicted to substitute PO_4^{3-} in the apatite lattice.[283-286], vanadyl V(VI) likely adsorbs on the bone surface by coordinating to phosphate.[292-295] In a series

of studies conducted by Dikanov *et al*, electron spin echo envelope modulation (ESEEM) investigations on VO^{2+}-bone, VO^{2+}-HAP, and VO^{2+}-triphosphate samples were conducted. Three identifiable V-O-P (phosphate) binding modes from several structurally distinct vanadyl-phosphate complexes in the bone matrix were observed.[294] Comparison to the reference species demonstrated a facial, tridentate triphosphate coordinated to the vanadyl cation along with two water molecules near the equatorial plane, shown in Figure 1.8.[295, 296] This species is indicative of vanadyl adsorbed to the hydrated surface of bone. Further complicating investigations into vanadium interactions with bone, studies suggest that V(V) can be reduced to V(IV) within bone *in vivo*.[291]
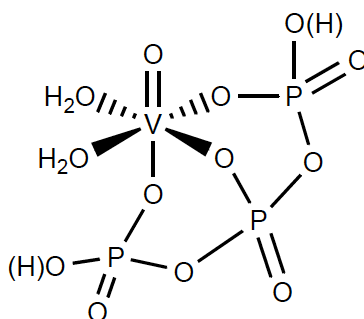
Figure 1.8. Proposed solution structure of VO^{2+}-triphosphate.[296]

Chromium also exists in two oxidation states *in vivo*, Cr(III) and Cr(VI). However, its uptake mechanism is hypothesized to be limited to Cr(III) alone since Cr(VI) reduces to Cr(III) *in vivo*, after Cr(VI) intake.[194] When considering leaching from Cr-based implants, Merritt and Brown used *in vitro* experiments to demonstrate that, upon corrosion, Cr(VI) ions are released and subsequentially taken up into the red blood cells and reduced to Cr(III).[297, 298] Hart *et al.* investigated the Cr speciation in hip capsule tissue from failed hip implants using X-ray absorption spectroscopy (XAS) and found no evidence of Cr(VI) species.[249] Furthermore, chromium in periprosthetic tissue closely resembled Cr(III) phosphate, $CrPO_4 \cdot 4H_2O$. Determining whether chromium deposits in bone by substituting calcium ions, adsorbing to bone surface via interactions with phosphate groups, similar to VO^{2+}, or by some alternative mechanism requires more study.

Beyond pH, it is important to consider the effect of biogenic ligands on metal uptake into bone. Group 4 metals tend to form insoluble MO_2 species in solution at neutral pH.[5] In the body, their solubility is enhanced by complexation to biogenic ligands such as blood serum transferrin.[28-30] Conversely, synthetic HAP experiments with zirconium and hafnium were conducted at a pHs

> 8 in the absence of complexing ligands[268, 269] while titanium-doped HAP was prepared by incubating HAP with NaCl solutions containing different concentrations of Ti.[266, 267] Given the differences between the experimental and *in vivo* conditions, it is difficult to determine if Group 4 metals ion-exchange with calcium in biological apatite, as suggested by synthetic HAP studies, or are deposited via an alternate mechanism, such as coprecipitating as phosphates. After incubating HAP with titanium, Ribeiro *et al.* observed the formation of Ti phosphate, $Ti(HPO_4)_2 \cdot nH_2O$, in HAP at Ti concentrations above 200 ppm.[266, 267] Zr^{4+} also shows a strong affinity for phosphate in solution.[163]

Given the complexity of bone tissue and the high sensitivity of ETM speciation to the aqueous environment, including complexing ligands and pH, more studies that follow bio-mimic approaches are needed to obtain an adequate picture of ETM accumulation in biological apatite.[258] Wang *et al.*, very recently (2020) set up an *in vitro* experiment that accounts for solid/liquid exchange in apatite under biomimetic conditions.[260] They investigated the interaction of uranium(VI) with apatite and, in agreement with *in vivo* data, demonstrate that uranium accumulation in bone is due to diffusion into the amorphous layer, not precipitation of a uranium phosphate phase as suggested by structural studies of crystalline HAP. Future work using biomimetic strategies such as this are required to gain a better understanding of the interaction of ETMs with bone.

1.5.3. Connection between Metal Uptake and Bone Remodeling?

A relationship between bone remodeling and metal uptake into bone has rarely been discussed. However, Group 5 and 6 metals, vanadium,[179, 180] niobium,[188, 189] chromium,[197] molybdenum,[220] and tungsten[217, 299] all demonstrate higher uptake in the bones of young animals, specifically in areas of recent bone formation. No reports were found which specifically discuss tantalum uptake in young animals. Higher uptake in young animals indicates an accumulation mechanism linked to bone remodelling, as remodelling activity is significantly higher in growing bones versus mature bone.

It is interesting that this trend is specifically observed for Group 5 and 6 metals. These metals have a complex aqueous chemistry where the formation of several POMs could be possible depending on the pH and metal concentration (Section 2.2.). During bone remodeling, the pH can lower to ~4.5 in the localized resorption pockets created by osteoclasts (Section 3.4.). Furthermore, calcium and phosphate ions mobilized from the inorganic bone matrix are also concentrated in

solution. These conditions are ripe for the creation of POMs and heteropolyoxoanions.[43] An uptake mechanism related to bone remodelling has not been considered extensively in the literature beyond the observation of higher uptake of some metals in younger animals.

Formation of POM species in bone is concerning because these species can be long lasting and more reactive than their simple monovalent oxyanions. The reactivity of POMs is well-documented, and these species are often used as catalysts in many reactions.[41, 45] However, the same redox and acidic properties of POMs which lead to their use in catalysis may also result in toxicity. For example, polytungstates, which form under normal environmental and physiological conditions, are much more toxic than their monotungstate (WO_4^{2-}) counterpart.[50] *In vivo* investigations of Group 5 and 6 metal speciation in bone must, therefore, be conducted to both understand their uptake mechanism and to provide a fundamental basis for toxicological study so that the biological effects of metal accumulation in bone is understood.

1.6. Conclusion

This Chapter describes how, despite decisive data reporting the accumulation of the ETMs in bone, there is little conclusive information about how, or in what form, these metals accumulate. Existing *in vivo* data is sparce and studies of metal uptake into synthetic HAP models are generally not done under biologically relevant conditions. ETM speciation in aqueous solutions is heavily dependent on pH, metal concentration, and presence of coordinating ligands. As metal speciation directly affects bone uptake mechanism, methodological studies with biomimetic systems are needed to fully understand the complex interaction of metals with bone's organic and inorganic matrix. *In vivo* studies are ultimately required to validate *in vitro* and model studies and to accurately determine metal distribution and speciation in bone. These studies are essential to understand how metals accumulate in bone and, ultimately, their effect on essential bone function.

This dissertation seeks to unravel some of the complexities of ETM bone accumulation, through the *in situ* study of tungsten distribution and speciation in bone. Chapter 2 will explore the distribution and speciation of tungsten in bone using synchrotron X-ray techniques. Chapter 3 and 4 are dedicated to improving methods for quantitatively determining localized metal distribution in bone by using laser ablation inductively coupled plasma mass spectrometry. Chapter 5 demonstrates the power of these methods to visualize and determine the form of other localized metals in biological tissue, in this case, copper and zinc deposits in knee and hip joint tissue.

Finally, Chapter 6 summarizes important conclusions from our study of tungsten in bone and provides future outlook on the topic.

1.7. References

1.   Kepp, K. P. A Quantitative Scale of Oxophilicity and Thiophilicity. *Inorganic Chemistry* **2016,** *55* (18), 9461-9470.

2.   Snead, L. L.; Hoelzer, D. T.; Rieth, M.; Nemith, A. A. N., Refractory Alloys: Vanadium, Niobium, Molybdenum, Tungsten. In *Structural Alloys for Nuclear Energy Applications*, Odette, G. R.; Zinkle, S. J., Eds. Elsevier: Boston, 2019; pp 585-640.

3.   International Plansee Society for Powder, M.; International Tungsten Industry, A., *International Journal of Refractory Metals & Hard Materials*. Elsevier Science Publishers Ltd.

4.   Matsuno, H.; Yokoyama, A.; Watari, F.; Uo, M.; Kawasaki, T. Biocompatibility and Osteogenesis of Refractory Metal Implants, Titanium, Hafnium, Niobium, Tantalum and Rhenium. *Biomaterials* **2001,** *22* (11), 1253-1262.

5.   Baes, C. F.; Mesmer, R. E., *The Hydrolysis of Cations*. Wiley: New York, 1976.

6.   ICRP, Report of the Task Group on Reference Man: A Report. Pergamon: 1975.

7.   Vidaud, C.; Bourgeois, D.; Meyer, D. Bone as Target Organ for Metals: The Case of F-Elements. *Chemical Research in Toxicology* **2012,** *25* (6), 1161-1175.

8.   Dermience, M.; Lognay, G.; Mathieu, F.; Goyens, P. Effects of Thirty Elements on Bone Metabolism. *Journal of Trace Elements in Medicine and Biology* **2015,** *32*, 86-106.

9.   Hallab, N. J.; Vermes, C.; Messina, C.; Roebuck, K. A.; Glant, T. T.; Jacobs, J. J. Concentration- and Composition-Dependent Effects of Metal Ions on Human Mg-63 Osteoblasts. *Journal of Biomedical Materials Research* **2002,** *60* (3), 420-433.

10.   Yamamoto, A.; Honma, R.; Sumita, M. Cytotoxicity Evaluation of 43 Metal Salts Using Murine Fibroblasts and Osteoblastic Cells. *Journal of Biomedical Materials Research* **1998,** *39* (2), 331-340.

11.   Bolt, A. M.; Mann, K. K. Tungsten: An Emerging Toxicant, Alone or in Combination. *Current Environmental Health Reports* **2016,** *3* (4), 405-415.

12.   Sansone, V.; Pagani, D.; Melato, M. The Effects on Bone Cells of Metal Ions Released from Orthopaedic Implants. A Review. *Clinical cases in mineral and bone metabolism : the official journal of the Italian Society of Osteoporosis, Mineral Metabolism, and Skeletal Diseases* **2013,** *10* (1), 34-40.

13. Puleo, D. A.; Huh, W. W. Acute Toxicity of Metal Ions in Cultures of Osteogenic Cells Derived from Bone Marrow Stromal Cells. *Journal of Applied Biomaterials* **1995,** *6* (2), 109-116.

14. Chen, Y.; Roohani-Esfahani, S.-I.; Lu, Z.; Zreiqat, H.; Dunstan, C. R. Zirconium Ions up-Regulate the Bmp/Smad Signaling Pathway and Promote the Proliferation and Differentiation of Human Osteoblasts. *PLOS ONE* **2015,** *10* (1), e0113426.

15. Barrio, D. A.; Etcheverry, S. B. Vanadium and Bone Development: Putative Signaling Pathways *Canadian Journal of Physiology and Pharmacology* **2006,** *84* (7), 677-686.

16. Ghosh, S. K.; Saha, R.; Saha, B. Toxicity of Inorganic Vanadium Compounds. *Research on Chemical Intermediates* **2015,** *41* (7), 4873-4897.

17. Asling, C. W.; Hurley, L. S. The Influence of Trace Elements on the Skeleton. *Clinical Orthopaedics and Related Research (1976-2007)* **1963,** *27*.

18. Lüthen, F.; Bulnheim, U.; Müller, P. D.; Rychly, J.; Jesswein, H.; Nebe, J. G. B. Influence of Manganese Ions on Cellular Behavior of Human Osteoblasts in Vitro. *Biomolecular Engineering* **2007,** *24* (5), 531-536.

19. Haase, A. A.; Bauer, E. B.; Kühn, F. E.; Crans, D. C. Speciation and Toxicity of Rhenium Salts, Organometallics and Coordination Complexes. *Coordination Chemistry Reviews* **2019,** *394*, 135-161.

20. Golasik, M.; Herman, M.; Piekoszewski, W. Toxicological Aspects of Soluble Titanium – a Review of in Vitro and in Vivo Studies. *Metallomics* **2016,** *8* (12), 1227-1242.

21. Dalal, A.; Pawar, V.; McAllister, K.; Weaver, C.; Hallab, N. J. Orthopedic Implant Cobalt-Alloy Particles Produce Greater Toxicity and Inflammatory Cytokines Than Titanium Alloy and Zirconium Alloy-Based Particles in Vitro, in Human Osteoblasts, Fibroblasts, and Macrophages. *Journal of biomedical materials research. Part A* **2012,** *100* (8), 2147-58.

22. Cotton, F. A., *Advanced Inorganic Chemistry*. 6th edition / ed.; Wiley: New York, 1999.

23. Shannon, R. D.; Prewitt, C. T. Effective Ionic Radii in Oxides and Fluorides. *Acta Crystallographica Section B* **1969,** *25* (5), 925-946.

24. Matusiewicz, H. Potential Release of in Vivo Trace Metals from Metallic Medical Implants in the Human Body: From Ions to Nanoparticles – a Systematic Analytical Review. *Acta Biomaterialia* **2014,** *10* (6), 2379-2403.

25. Silver, I. A.; Murrills, R. J.; Etherington, D. J. Microelectrode Studies on the Acid Microenvironment beneath Adherent Macrophages and Osteoclasts. *Experimental Cell Research* **1988,** *175* (2), 266-276.

26. Chakraborty, B.; Weinstock, I. A. Water-Soluble Titanium-Oxides: Complexes, Clusters and Nanocrystals. *Coordination Chemistry Reviews* **2019,** *382*, 85-102.

27. Loza-Rosas, S. A.; Saxena, M.; Delgado, Y.; Gaur, K.; Pandrala, M.; Tinoco, A. D. A Ubiquitous Metal, Difficult to Track: Towards an Understanding of the Regulation of Titanium(Iv) in Humans. *Metallomics : integrated biometal science* **2017,** *9* (4), 346-356.

28. Nuevo-Ordóñez, Y.; Montes-Bayón, M.; Blanco-González, E.; Paz-Aparicio, J.; Raimundez, J. D.; Tejerina, J. M.; Peña, M. A.; Sanz-Medel, A. Titanium Release in Serum of Patients with Different Bone Fixation Implants and Its Interaction with Serum Biomolecules at Physiological Levels. *Analytical and Bioanalytical Chemistry* **2011,** *401* (9), 2747.

29. Then, G. M.; Appel, H.; Duffield, J.; Taylor, D. M.; Thies, W. G. In Vivo and in Vitro Studies of Hafnium-Binding to Rat Serum Transferrin. *Journal of Inorganic Biochemistry* **1986,** *27* (4), 255-270.

30. Zhong, W.; Parkinson, J. A.; Guo, M.; Sadler, P. J. Unusual Features for Zirconium(Iv) Binding to Human Serum Transferrin. *JBIC Journal of Biological Inorganic Chemistry* **2002,** *7* (6), 589-599.

31. Costa, B. C.; Tokuhara, C. K.; Rocha, L. A.; Oliveira, R. C.; Lisboa-Filho, P. N.; Costa Pessoa, J. Vanadium Ionic Species from Degradation of Ti-6al-4v Metallic Implants: In Vitro Cytotoxicity and Speciation Evaluation. *Materials Science and Engineering: C* **2019,** *96*, 730-739.

32. Levina, A.; Crans, D. C.; Lay, P. A. Speciation of Metal Drugs, Supplements and Toxins in Media and Bodily Fluids Controls in Vitro Activities. *Coordination Chemistry Reviews* **2017,** *352*, 473-498.

33. Pope, M. T., *Heteropoly and Isopoly Oxometalates*. Springer-Verlag: Berlin ;, 1983.

34. Deblonde, G. J. P.; Chagnes, A.; Bélair, S.; Cote, G. Solubility of Niobium(V) and Tantalum(V) under Mild Alkaline Conditions. *Hydrometallurgy* **2015,** *156*, 99-106.

35. Peiffert, C.; Nguyen-Trung, C.; Palmer, D. A.; Laval, J. P.; Giffaut, E. Solubility of B-Nb2o5 and the Hydrolysis of Niobium(V) in Aqueous Solution as a Function of Temperature And ionic Strength. *Journal of Solution Chemistry* **2010,** *39* (2), 197-218.

36. Fairbrother, F.; Robinson, D.; Taylor, J. B. Some Water-Soluble Complexes of Pentavalent Niobium and Tantalum. *Journal of Inorganic and Nuclear Chemistry* **1958,** *8*, 296-301.

37. Abramov, P. A.; Sokolov, M. N.; Vicent, C. Polyoxoniobates and Polyoxotantalates as Ligands—Revisited. *Inorganics* **2015,** *3* (2), 160-177.

38. Filella, M.; May, P. M. The Aqueous Solution Thermodynamics of Niobium under Conditions of Environmental and Biological Interest. *Applied Geochemistry* **2020,** *122*, 104729.

39. Filella, M.; May, P. M. The Aqueous Solution Thermodynamics of Tantalum under Conditions of Environmental and Biological Interest. *Applied Geochemistry* **2019,** *109*, 104402.

40. Hill, C. L. Introduction: Polyoxometalates Multicomponent Molecular Vehicles to Probe Fundamental Issues and Practical Problems. *Chemical Reviews* **1998,** *98* (1), 1-2.

41. Hill, C. L., Polyoxometalates: Reactivity. In *Comprehensive Coordination Chemistry Ii*, McCleverty, J. A.; Meyer, T. J., Eds. Pergamon: Oxford, 2003; pp 679-759.

42. Pope, M. T., Polyoxo Anions: Synthesis and Structure. In *Comprehensive Coordination Chemistry Ii*, McCleverty, J. A.; Meyer, T. J., Eds. Pergamon: Oxford, 2003; pp 635-678.

43. Gumerova, N. I.; Rompel, A. Polyoxometalates in Solution: Speciation under Spotlight. *Chemical Society Reviews* **2020,** *49* (21), 7568-7601.

44. Samaniyan, M.; Mirzaei, M.; Khajavian, R.; Eshtiagh-Hosseini, H.; Streb, C. Heterogeneous Catalysis by Polyoxometalates in Metal–Organic Frameworks. *ACS Catalysis* **2019,** *9* (11), 10174-10191.

45. Wang, S.-S.; Yang, G.-Y. Recent Advances in Polyoxometalate-Catalyzed Reactions. *Chemical Reviews* **2015,** *115* (11), 4893-4962.

46. Pope, M. T., Chapter 9 - Structural Chemistry of Actinide Polyoxometalates. In *Structural Chemistry of Inorganic Actinide Compounds*, Krivovichev, S. V.; Burns, P. C.; Tananaev, I. G., Eds. Elsevier: Amsterdam, 2007; pp 341-361.

47. Afolaranmi, G. A.; Tettey, J.; Meek, R. M. D.; Grant, M. H. Release of Chromium from Orthopaedic Arthroplasties. *The open orthopaedics journal* **2008,** *2*, 10-18.

48. Stuenzi, H.; Marty, W. Early Stages of the Hydrolysis of Chromium(Iii) in Aqueous Solution. 1. Characterization of a Tetrameric Species. *Inorganic Chemistry* **1983,** *22* (15), 2145-2150.

49. Pope, M. T.; Kortz, U. Polyoxometalates. *Encyclopedia of Inorganic and Bioinorganic Chemistry* **2012**.

50. Strigul, N. Does Speciation Matter for Tungsten Ecotoxicology? *Ecotoxicology and Environmental Safety* **2010,** *73* (6), 1099-1113.

51. Geetha, M.; Singh, A. K.; Asokamani, R.; Gogia, A. K. Ti Based Biomaterials, the Ultimate Choice for Orthopaedic Implants – a Review. *Progress in Materials Science* **2009,** *54* (3), 397-425.

52. Saini, M.; Singh, Y.; Arora, P.; Arora, V.; Jain, K. Implant Biomaterials: A Comprehensive Review. *World journal of clinical cases* **2015,** *3* (1), 52-57.

53. Guibert, G.; Irigaray, J. L.; Moretto, P.; Sauvage, T.; Kemeny, J. L.; Cazenave, A.; Jallot, E. Characterisation by Pixe–Rbs of Metallic Contamination of Tissues Surrounding a Metallic Prosthesis on a Knee. *Nuclear Instruments and Methods in Physics Research Section B: Beam Interactions with Materials and Atoms* **2006,** *251* (1), 246-256.

54. Eliaz, N. Corrosion of Metallic Biomaterials: A Review. *Materials (Basel, Switzerland)* **2019,** *12* (3), 407.

55. Virtanen, S.; Milošev, I.; Gomez-Barrena, E.; Trebše, R.; Salo, J.; Konttinen, Y. T. Special Modes of Corrosion under Physiological and Simulated Physiological Conditions. *Acta Biomaterialia* **2008,** *4* (3), 468-476.

56. Wapner, K. L. Implications of Metallic Corrosion in Total Knee Arthroplasty. *Clinical Orthopaedics and Related Research®* **1991,** *271*.

57. Eisenbarth, E.; Velten, D.; Müller, M.; Thull, R.; Breme, J. Biocompatibility of Β-Stabilizing Elements of Titanium Alloys. *Biomaterials* **2004,** *25* (26), 5705-5713.

58. Domingo, J. L. Vanadium and Tungsten Derivatives as Antidiabetic Agents. *Biological Trace Element Research* **2002,** *88* (2), 97-112.

59. Zhao, X.; Niinomi, M.; Nakai, M.; Ishimoto, T.; Nakano, T. Development of High Zr-Containing Ti-Based Alloys with Low Young's Modulus for Use in Removable Implants. *Materials Science and Engineering: C* **2011,** *31* (7), 1436-1444.

60. Miyazaki, T.; Sueoka, M.; Shirosaki, Y.; Shinozaki, N.; Shiraishi, T. Development of Hafnium Metal and Titanium-Hafnium Alloys Having Apatite-Forming Ability by Chemical Surface Modification. *Journal of Biomedical Materials Research Part B: Applied Biomaterials* **2018,** *106* (7), 2519-2523.

61. Kobayashi, E.; Wang, T. J.; Doi, H.; Yoneyama, T.; Hamanaka, H. Mechanical Properties and Corrosion Resistance of Ti–6al–7nb Alloy Dental Castings. *Journal of Materials Science: Materials in Medicine* **1998,** *9* (10), 567-574.

62. Zhou, Y. L.; Niinomi, M.; Akahori, T.; Fukui, H.; Toda, H. Corrosion Resistance and Biocompatibility of Ti–Ta Alloys for Biomedical Applications. *Materials Science and Engineering: A* **2005,** *398* (1), 28-36.

63. Correa, D. R. N.; Kuroda, P. A. B.; Grandini, C. R. Structure, Microstructure, and Selected Mechanical Properties of Ti-Zr-Mo Alloys for Biomedical Applications. *Advanced Materials Research* **2014,** *922*, 75-80.

64. González, M.; Peña, J.; Manero, J. M.; Arciniegas, M.; Gil, F. J. Design and Characterization of New Ti-Nb-Hf Alloys. *Journal of Materials Engineering and Performance* **2009,** *18* (5), 490-495.

65. Nagase, T.; Iijima, Y.; Matsugaki, A.; Ameyama, K.; Nakano, T. Design and Fabrication of Ti–Zr-Hf-Cr-Mo and Ti–Zr-Hf-Co-Cr-Mo High-Entropy Alloys as Metallic Biomaterials. *Materials Science and Engineering: C* **2020,** *107*, 110322.

66. Yuan, Y.; Wu, Y.; Yang, Z.; Liang, X.; Lei, Z.; Huang, H.; Wang, H.; Liu, X.; An, K.; Wu, W.; Lu, Z. Formation, Structure and Properties of Biocompatible Tizrhfnbta High-Entropy Alloys. *Materials Research Letters* **2019,** *7* (6), 225-231.

67. Lin, J.; Ozan, S.; Li, Y.; Ping, D.; Tong, X.; Li, G.; Wen, C. Novel Ti-Ta-Hf-Zr Alloys with Promising Mechanical Properties for Prospective Stent Applications. *Scientific Reports* **2016,** *6* (1), 37901.

68. Sato, H.; Kikuchi, M.; Komatsu, M.; Okuno, O.; Okabe, T. Mechanical Properties of Cast Ti–Hf Alloys. *Journal of Biomedical Materials Research Part B: Applied Biomaterials* **2005,** *72B* (2), 362-367.

69. Okazaki, Y.; Gotoh, E. Comparison of Metal Release from Various Metallic Biomaterials in Vitro. *Biomaterials* **2005,** *26* (1), 11-21.

70. Kobayashi, E.; Doi, H.; Yoneyama, T.; Hamanaka, H.; Gibson, I. R.; Best, S. M.; Shelton, J. C.; Bonfield, W. Influence of Aging Heat Treatment on Mechanical Properties of Biomedical Ti–Zr Based Ternary Alloys Containing Niobium. *Journal of Materials Science: Materials in Medicine* **1998,** *9* (11), 625-630.

71. Rituerto Sin, J.; Neville, A.; Emami, N. Corrosion and Tribocorrosion of Hafnium in Simulated Body Fluids. *Journal of Biomedical Materials Research Part B: Applied Biomaterials* **2014,** *102* (6), 1157-1164.

72. Badawy, W. A.; Al-Kharafi, F. M. The Electrochemical Behaviour of Naturally Passivated Hafnium in Aqueous Solutions of Different Ph. *Journal of Materials Science* **1999,** *34* (10), 2483-2491.

73. Hussein, M. A.; Mohammed, A. S.; Al-Aqeeli, N. Wear Characteristics of Metallic Biomaterials: A Review. *Materials* **2015,** *8* (5), 2749-2768.

74. Aherwar, A.; Bahraminasab, M. Biocompatibility Evaluation and Corrosion Resistance of Tungsten Added Co-30cr-4mo-1ni Alloy. *Bio-Medical Materials & Engineering* **2017,** *28* (6), 687-701.

75. Karaali, A.; Mirouh, K.; Hamamda, S.; Guiraldenq, P. Microstructural Study of Tungsten Influence on Co–Cr Alloys. *Materials Science and Engineering: A* **2005,** *390* (1), 255-259.

76.   Salgado, A. J.; Coutinho, O. P.; Reis, R. L. Bone Tissue Engineering: State of the Art and Future Trends. *Macromolecular Bioscience* **2004,** *4* (8), 743-765.

77.   Clarke, B. Normal Bone Anatomy and Physiology. *Clinical Journal of the American Society of Nephrology* **2008,** *3* (Supplement 3), S131.

78.   Taichman, R. S. Blood and Bone: Two Tissues Whose Fates Are Intertwined to Create the Hematopoietic Stem-Cell Niche. *Blood* **2005,** *105* (7), 2631-2639.

79.   Manolagas, S. C. Birth and Death of Bone Cells: Basic Regulatory Mechanisms and Implications for the Pathogenesis and Treatment of Osteoporosis. *Endocrine Reviews* **2000,** *21* (2), 115-137.

80.   Buckwalter, J.; Glimcher, M.; Cooper, R.; Recker, R. Bone Biology. *The Journal of Bone and Joint Surgery* **1995,** *77* (8), 1256-1275.

81.   Sikavitsas, V. I.; Temenoff, J. S.; Mikos, A. G. Biomaterials and Bone Mechanotransduction. *Biomaterials* **2001,** *22* (19), 2581-2593.

82.   J. Gordon Betts, J. G.; Young, K. A.; Wise, J. A.; Johnson, E.; Poe, B.; Kruse, D. H.; Korol, O.; Johnson, J. E.; Womble, M.; DeSaix, P., *Anatomy and Physiology*. OpenStax: Houston, Texas, 2013.

83.   Marks, S.; Odgren, P.; Bilezikian, J.; Raisz, L.; Rodan, G. Principles of Bone Biology. *Academic, San Diego, CA* **1996**, 3.

84.   Weiner, S.; Wagner, H. D. The Material Bone: Structure-Mechanical Function Relations. *Annual Review of Materials Science* **1998,** *28* (1), 271-298.

85.   Weiner, S.; Traub, W.; Wagner, H. D. Lamellar Bone: Structure–Function Relations. *Journal of Structural Biology* **1999,** *126* (3), 241-255.

86.   Eanes, E. D. Crystal Growth of Mineral Phases in Skeletal Tissues. *Progress in Crystal Growth and Characterization* **1980,** *3* (1), 3-15.

87.   Christoffersen, J.; Landis, W. J. A Contribution with Review to the Description of Mineralization of Bone and Other Calcified Tissues in Vivo. *The Anatomical Record* **1991,** *230* (4), 435-450.

88.   Boskey, A. L. Biomineralization: An Overview. *Connective Tissue Research* **2003,** *44* (1), 5-9.

89.   Hoppe, A.; Güldal, N. S.; Boccaccini, A. R. A Review of the Biological Response to Ionic Dissolution Products from Bioactive Glasses and Glass-Ceramics. *Biomaterials* **2011,** *32* (11), 2757-2774.

90.   Palmer, L. C.; Newcomb, C. J.; Kaltz, S. R.; Spoerke, E. D.; Stupp, S. I. Biomimetic Systems for Hydroxyapatite Mineralization Inspired by Bone and Enamel. *Chemical Reviews* **2008,** *108* (11), 4754-4783.

91.   Mohd Pu'ad, N. A. S.; Abdul Haq, R. H.; Mohd Noh, H.; Abdullah, H. Z.; Idris, M. I.; Lee, T. C. Synthesis Method of Hydroxyapatite: A Review. *Materials Today: Proceedings* **2020,** *29*, 233-239.

92.   Szcześ, A.; Hołysz, L.; Chibowski, E. Synthesis of Hydroxyapatite for Biomedical Applications. *Advances in Colloid and Interface Science* **2017,** *249*, 321-330.

93.   Mostafa, N. Y.; Brown, P. W. Computer Simulation of Stoichiometric Hydroxyapatite: Structure and Substitutions. *Journal of Physics and Chemistry of Solids* **2007,** *68* (3), 431-437.

94.   Elliott, J. C., *Structure and Chemistry of the Apatites and Other Calcium Orthophosphates*. Elsevier: Amsterdam, The Netherlands, 1994; Vol. 18.

95.   Laurencin, D.; Wong, A.; Dupree, R.; Smith, M. E. Natural Abundance 43ca Solid-State Nmr Characterisation of Hydroxyapatite: Identification of the Two Calcium Sites. *Magnetic Resonance in Chemistry* **2008,** *46* (4), 347-350.

96.   Rey, C.; Collins, B.; Goehl, T.; Dickson, I. R.; Glimcher, M. J. The Carbonate Environment in Bone Mineral: A Resolution-Enhanced Fourier Transform Infrared Spectroscopy Study. *Calcified Tissue International* **1989,** *45* (3), 157-164.

97.   Wu, Y.; Glimcher, M. J.; Rey, C.; Ackerman, J. L. A Unique Protonated Phosphate Group in Bone Mineral Not Present in Synthetic Calcium Phosphates: Identification by Phosphorus-31 Solid State Nmr Spectroscopy. *Journal of Molecular Biology* **1994,** *244* (4), 423-435.

98.   Rey, C.; Shimizu, M.; Collins, B.; Glimcher, M. J. Resolution-Enhanced Fourier Transform Infrared Spectroscopy Study of the Environment of Phosphate Ion in the Early Deposits of a Solid Phase of Calcium Phosphate in Bone and Enamel and Their Evolution with Age: 2. Investigations in the V3 Po4 Domain. *Calcified Tissue International* **1991,** *49* (6), 383-388.

99.   Combes, C.; Cazalbou, S.; Rey, C. Apatite Biominerals. *Minerals* **2016,** *6* (2).

100.   Young, R. A. Implications of Atomic Substitutions and Other Structural Details in Apatites. *Journal of Dental Research* **1974,** *53* (2), 193-203.

101.   Posner, A. S. Crystal Chemistry of Bone Mineral. *Physiological Reviews* **1969,** *49* (4), 760-792.

102.   Trautz, O. R. X-Ray Diffraction of Biological and Synthetic Apatites. *Annals of the New York Academy of Sciences* **1955,** *60* (5), 696-712.

103.   Rey, C.; Lian, J.; Grynpas, M.; Shapiro, F.; Zylberberg, L.; Glimcher, M. J. Non-Apatitic Environments in Bone Mineral: Ft-Ir Detection, Biological Properties and Changes in Several Disease States. *Connective Tissue Research* **1989,** *21* (1-4), 267-273.

104.   The Nature and Composition of the Inorganic Phase. In *Biological Calcification: Normal and Pathological Processes in the Early Stages*, Bonucci, E., Ed. Springer Berlin Heidelberg: Berlin, Heidelberg, 2007; pp 67-103.

105.   Smith, C. B.; Smith, D. A. An X-Ray Diffraction Investigation of Age-Related Changes in the Crystal Structure of Bone Apatite. *Calcified Tissue Research* **1977,** *22* (1), 219-226.

106.   Arnold, S.; Plate, U.; Wiesmann, H. P.; Stratmann, U.; Kohl, H.; Höhling, H. J. Quantitative Analyses of the Biomineralization of Different Hard Tissues. *Journal of Microscopy* **2001,** *202* (3), 488-494.

107.   Posner, A. S.; Harper, R. A.; Muller, S. A.; Menczel, J. Age Changes in the Crystal Chemistry of Bone Apatite. *Annals of the New York Academy of Sciences* **1965,** *131* (2), 737-742.

108.   Burnell, J. M.; Teubner, E. J.; Miller, A. G. Normal Maturational Changes in Bone Matrix, Mineral, and Crystal Size in the Rat. *Calcified Tissue International* **1980,** *31* (1), 13-19.

109.   Glimcher, M. J., The Nature of the Mineral Phase in Bone: Biological and Clinical Implications. In *Metabolic Bone Disease and Clinically Related Disorders (Third Edition)*, Avioli, L. V.; Krane, S. M., Eds. Academic Press: San Diego, 1998; pp 23-52e.

110.   Prockop, D. J.; Kivirikko, K. I. Collagens: Molecular Biology, Diseases, and Potentials for Therapy. *Annual Review of Biochemistry* **1995,** *64* (1), 403-434.

111.   Cui, F.-Z.; Li, Y.; Ge, J. Self-Assembly of Mineralized Collagen Composites. *Materials Science and Engineering: R: Reports* **2007,** *57* (1), 1-27.

112.   Nair, A. K.; Gautieri, A.; Chang, S.-W.; Buehler, M. J. Molecular Mechanics of Mineralized Collagen Fibrils in Bone. *Nature Communications* **2013,** *4* (1), 1724.

113.   Hauschka, P. V.; Lian, J. B.; Cole, D. E.; Gundberg, C. M. Osteocalcin and Matrix Gla Protein: Vitamin K-Dependent Proteins in Bone. *Physiological Reviews* **1989,** *69* (3), 990-1047.

114.   Pacifici, M.; Oshima, O.; Fisher, L. W.; Young, M. F.; Shapiro, I. M.; Leboy, P. S. Changes in Osteonectin Distribution and Levels Are Associated with Mineralization of the Chicken Tibial Growth Cartilage. *Calcified Tissue International* **1990,** *47* (1), 51-61.

115.   Sodek, J.; Ganss, B.; McKee, M. D. Osteopontin. *Critical Reviews in Oral Biology & Medicine* **2000,** *11* (3), 279-303.

116.   Ganss, B.; Kim, R. H.; Sodek, J. Bone Sialoprotein. *Critical Reviews in Oral Biology & Medicine* **1999,** *10* (1), 79-98.

117.   Golub, E. E.; Boesze-Battaglia, K. The Role of Alkaline Phosphatase in Mineralization. *Current Opinion in Orthopaedics* **2007,** *18* (5).

118.   Florencio-Silva, R.; Sasso, G. R. d. S.; Sasso-Cerri, E.; Simões, M. J.; Cerri, P. S. Biology of Bone Tissue: Structure, Function, and Factors That Influence Bone Cells. *BioMed research international* **2015,** *2015*, 421746.

119.   Frost, H. M. Tetracycline-Based Histological Analysis of Bone Remodeling. *Calcified Tissue Research* **1969,** *3* (1), 211-237.

120.   Hauge, E. M.; Qvesel, D.; Eriksen, E. F.; Mosekilde, L.; Melsen, F. Cancellous Bone Remodeling Occurs in Specialized Compartments Lined by Cells Expressing Osteoblastic Markers. *Journal of Bone and Mineral Research* **2001,** *16* (9), 1575-1582.

121.   Roodman, G. D. Cell Biology of the Osteoclast. *Experimental Hematology* **1999,** *27* (8), 1229-1241.

122.   Chambers, T. J.; Fuller, K. Bone Cells Predispose Bone Surfaces to Resorption by Exposure of Mineral to Osteoclastic Contact. *Journal of Cell Science* **1985,** *76* (1), 155.

123.   Vaananen, H. K.; Zhao, H.; Mulari, M.; Halleen, J. M. The Cell Biology of Osteoclast Function. *Journal of Cell Science* **2000,** *113* (3), 377.

124.   Teitelbaum, S. L. Bone Resorption by Osteoclasts. *Science* **2000,** *289* (5484), 1504.

125.   Roodman, G. D. Advances in Bone Biology: The Osteoclast*. *Endocrine Reviews* **1996,** *17* (4), 308-332.

126.   Delaissé, J.-M.; Andersen, T. L.; Engsig, M. T.; Henriksen, K.; Troen, T.; Blavier, L. Matrix Metalloproteinases (Mmp) and Cathepsin K Contribute Differently to Osteoclastic Activities. *Microscopy Research and Technique* **2003,** *61* (6), 504-513.

127.   Salo, J.; Lehenkari, P.; Mulari, M.; Metsikkö, K.; Väänänen, H. K. Removal of Osteoclast Bone Resorption Products by Transcytosis. *Science* **1997,** *276* (5310), 270.

128.   Kennedy, P.; Jain, A.; Srinivasan, R.; Chaudhry, S. Calcium Homeostasis and Osteoporosis. *McMaster Pathophysiology Review* **2018**.

129.   Sims, N. A.; Gooi, J. H. Bone Remodeling: Multiple Cellular Interactions Required for Coupling of Bone Formation and Resorption. *Seminars in Cell & Developmental Biology* **2008,** *19* (5), 444-451.

130.   Matsuo, K.; Irie, N. Osteoclast–Osteoblast Communication. *Archives of Biochemistry and Biophysics* **2008,** *473* (2), 201-209.

131.   Lorget, F.; Kamel, S.; Mentaverri, R.; Wattel, A.; Naassila, M.; Maamer, M.; Brazier, M. High Extracellular Calcium Concentrations Directly Stimulate Osteoclast Apoptosis. *Biochemical and Biophysical Research Communications* **2000,** *268* (3), 899-903.

132.   Martin, T. J.; Sims, N. A. Osteoclast-Derived Activity in the Coupling of Bone Formation to Resorption. *Trends in Molecular Medicine* **2005,** *11* (2), 76-81.

133.   Locklin, R. M.; Oreffo, R. O. C.; Triffitt, J. T. Effects of Tgfβ and Bfgf on the Differentiation of Human Bone Marrow Stromal Fibroblasts. *Cell Biology International* **1999,** *23* (3), 185-194.

134.   Mackie, E. J. Osteoblasts: Novel Roles in Orchestration of Skeletal Architecture. *The International Journal of Biochemistry & Cell Biology* **2003,** *35* (9), 1301-1305.

135.   Robey, P. G., Chapter 14 - Bone Matrix Proteoglycans and Glycoproteins. In *Principles of Bone Biology (Second Edition)*, Bilezikian, J. P.; Raisz, L. G.; Rodan, G. A., Eds. Academic Press: San Diego, 2002; pp 225-237.

136.   Anderson, H. C. Matrix Vesicles and Calcification. *Current Rheumatology Reports* **2003,** *5* (3), 222-6.

137.   Lanyon, L. E. Osteocytes, Strain Detection, Bone Modeling and Remodeling. *Calcified Tissue International* **1993,** *53* (1), S102-S107.

138.   Prideaux, M.; Findlay, D. M.; Atkins, G. J. Osteocytes: The Master Cells in Bone Remodelling. *Current Opinion in Pharmacology* **2016,** *28*, 24-30.

139.   Dallas, S. L.; Prideaux, M.; Bonewald, L. F. The Osteocyte: An Endocrine Cell … and More. *Endocrine Reviews* **2013,** *34* (5), 658-690.

140.   Paquet, F.; Bailey, M. R.; Leggett, R. W.; Lipsztein, J.; Fell, T. P.; Smith, T.; Nosske, D.; Eckerman, K. F.; Berkovski, V.; Ansoborlo, E.; Giussani, A.; Bolch, W. E.; Harrison, J. D. Icrp Publication 134: Occupational Intakes of Radionuclides: Part 2. *Annals of the ICRP* **2016,** *45* (3-4), 7-349.

141.   Metabolic Data for Hafnium. *Annals of the ICRP* **1981,** *6* (2-3), 88-89.

142.   Metabolic Data for Tantalum. *Annals of the ICRP* **1981,** *6* (2-3), 90-92.

143.   Metabolic Data for Tungsten. *Annals of the ICRP* **1981,** *6* (2-3), 93-95.

144.   Metabolic Data for Titanium. *Annals of the ICRP* **1981,** *6* (2), 20-21.

145.   Metabolic Data for Vanadium. *Annals of the ICRP* **1981,** *6* (2), 22-24.

146.   Metabolic Data for Rhenium. *Annals of the ICRP* **1980,** *4* (3-4), 50-51.

147.   Metabolic Data for Technetium. *Annals of the ICRP* **1980,** *4* (3), 32-34.

148.   Metabolic Data for Chromium. *Annals of the ICRP* **1980,** *4* (3), 15-16.

149.   Metabolic Data for Zirconium. *Annals of the ICRP* **1979,** *2* (3, Part 1), 79-80.

150.   Metabolic Data for Manganese. *Annals of the ICRP* **1979,** *2* (3, Part 1), 71-72.

151.   Metabolic Data for Molybdenum. *Annals of the ICRP* **1979,** *2* (3, Part 1), 83-84.

152.   Metabolic Data for Niobium. *Annals of the ICRP* **1979,** *2* (3, Part 1), 81-82.

153.   Leggett, R.; Samuels, C. Biokinetic Models for Group Ivb Elements. *Journal of Radiological Protection* **2020,** *40* (4), 1123-1137.

154.   Miller, J. K.; Madsen, F. C.; Hansard, S. L. Absorption, Excretion, and Tissue Deposition of Titanium in Sheep. *Journal of Dairy Science* **1976,** *59* (11), 2008-2010.

155.   Edel, J.; Marafante, E.; Sabbioni, E. Retention and Tissue Binding of Titanium in the Rat. *Human Toxicology* **1985,** *4* (2), 177-185.

156.   Merritt, K.; Brown, S. A. Distribution of Titanium and Vanadium Following Repeated Injection of High-Dose Salts. *Journal of Biomedical Materials Research* **1995,** *29* (10), 1175-1178.

157.   Zhu, H.; Wang, N.; Zhang, Y.; Wu, Q.; Chen, R.; Gao, J.; Chang, P.; Liu, Q.; Fan, T.; Li, J.; Wang, J.; Wang, J. Element Contents in Organs and Tissues of Chinese Adult Men. *Health Physics* **2010,** *98* (1).

158.   Zeman, T.; Loh, E.-W.; Čierný, D.; Šerý, O. Penetration, Distribution and Brain Toxicity of Titanium Nanoparticles in Rodents' Body: A Review. *IET Nanobiotechnology* **2018,** *12* (6), 695-700.

159.   Kreyling, W. G.; Holzwarth, U.; Haberl, N.; Kozempel, J.; Hirn, S.; Wenk, A.; Schleh, C.; Schäffler, M.; Lipka, J.; Semmler-Behnke, M.; Gibson, N. Quantitative Biokinetics of Titanium Dioxide Nanoparticles after Intravenous Injection in Rats: Part 1. *Nanotoxicology* **2017,** *11* (4), 434-442.

160.   Kreyling, W. G.; Holzwarth, U.; Schleh, C.; Kozempel, J.; Wenk, A.; Haberl, N.; Hirn, S.; Schäffler, M.; Lipka, J.; Semmler-Behnke, M.; Gibson, N. Quantitative Biokinetics of Titanium Dioxide Nanoparticles after Oral Application in Rats: Part 2. *Nanotoxicology* **2017,** *11* (4), 443-453.

161.   Kreyling, W. G.; Holzwarth, U.; Haberl, N.; Kozempel, J.; Wenk, A.; Hirn, S.; Schleh, C.; Schäffler, M.; Lipka, J.; Semmler-Behnke, M.; Gibson, N. Quantitative Biokinetics of Titanium Dioxide Nanoparticles after Intratracheal Instillation in Rats: Part 3. *Nanotoxicology* **2017,** *11* (4), 454-464.

162.   Larenkov, A.; Bubenschikov, V.; Makichyan, A.; Zhukova, M.; Krasnoperova, A.; Kodina, G. Preparation of Zirconium-89 Solutions for Radiopharmaceutical Purposes:

Interrelation between Formulation, Radiochemical Purity, Stability and Biodistribution. *Molecules* **2019,** *24* (8).

163. Abou, D. S.; Ku, T.; Smith-Jones, P. M. In Vivo Biodistribution and Accumulation of 89zr in Mice. *Nuclear Medicine and Biology* **2011,** *38* (5), 675-681.

164. Backstrom, J.; Hammarstrom, L.; Nelson, A. Distribution of Zirconium and Niobium in Mice. Autoradiographic Study. *Acta Radiologica: Therapy, Physics, Biology* **1967,** *6* (2), 122-8.

165. Ishinishi, N.; Morishige, T. A Study on the Distribution of 95zr-95nb Administered Subcutaneously to Rats: Comparison between Young and Adult Rats. *Journal of Radiation Research* **1969,** *10* (3-4), 101-106.

166. Rama Sastry, B. V.; Owens, L. K.; Ball, C. O. T. Differences in the Distribution of Zirconium-95 and Niobium-95 in the Rat. *Nature* **1964,** *201* (4917), 410-411.

167. Ando, A.; Ando, I. Distribution of 95zr and 181hf in Tumor-Bearing Animals and Mechanism for Accumulation in Tumor and Liver. *International Journal of Radiation Applications and Instrumentation. Part B. Nuclear Medicine and Biology* **1986,** *13* (1), 21-29.

168. Taylor, D. M.; Seidel, A.; Doerfel, H. The Metabolism of Radiohafnium in Marmosets and Hamsters. *International Journal of Nuclear Medicine and Biology* **1985,** *12* (5), 387-391.

169. Taylor, D. M.; Lehmann, M.; Planas-Bohne, F.; Seidel, A. The Metabolism of Radiohafnium in Rats and Hamsters: A Possible Analog of Plutonium for Metabolic Studies. *Radiation Research* **1983,** *95* (2), 339-358.

170. Leggett, R.; O'Connell, C. Biokinetic Models for Group Vb Elements. *Journal of Radiological Protection* **2018,** *38* (2), 564-586.

171. Barceloux, D. G.; Barceloux, D. Vanadium. *Journal of Toxicology: Clinical Toxicology* **1999,** *37* (2), 265-278.

172. Amano, R.; Enomoto, S.; Nobuta, M.; Sakamoto, M.; Tsujioka, R.; Ambe, F. Bone Uptake of Vanadium in Mice: Simultaneous Tracing of V, Se, Sr, Y, Zr, Ru and Rh Using a Radioactive Multitracer. *Journal of Trace Elements in Medicine and Biology* **1996,** *10* (3), 145-148.

173. Roshchin, A. V.; Ordzhonikidze, E. K.; Shalganova, I. V. Vanadium--Toxicity, Metabolism, Carrier State. *Journal of hygiene, epidemiology, microbiology, and immunology* **1980,** *24* (4), 377-83.

174. Thompson, K. H.; Tsukada, Y.; Xu, Z.; Battell, M.; McNeill, J. H.; Orvig, C. Influence of Chelation and Oxidation State on Vanadium Bioavailability, and Their Effects on

Tissue Concentrations of Zinc, Copper, and Iron. *Biological Trace Element Research* **2002,** *86* (1), 31.

175.   Setyawati, I. A.; Thompson, K. H.; Yuen, V. G.; Sun, Y.; Battell, M.; Lyster, D. M.; Vo, C.; Ruth, T. J.; Zeisler, S.; McNeill, J. H.; Orvig, C. Kinetic Analysis and Comparison of Uptake, Distribution, and Excretion of 48v-Labeled Compounds in Rats. *Journal of Applied Physiology* **1998,** *84* (2), 569-575.

176.   Oberg, S. G.; Parker, R. D. R.; Sharma, R. P. Distribution and Elimination of an Intratracheally Administered Vanadium Compound in the Rat. *Toxicology* **1978,** *11*, 315-323.

177.   Sharma, R. P.; Flora, S. J. S.; Drown, D. B.; Oberg, S. G. Persistence of Vanadium Compounds in Lungs after Intratracheal Instillation in Rats. *Toxicology and Industrial Health* **1987,** *3* (3), 321-329.

178.   Sharma, R. P.; Oberg, S. G.; Parker, R. D. R. Vanadium Retention in Rat Tissues Following Acute Exposures to Different Dose Levels. *Journal of Toxicology and Environmental Health* **1980,** *6* (1), 45-54.

179.   Mravcová, A.; Jírová, D.; Jančí, H.; Lener, J. Effects of Orally Administered Vanadium on the Immune System and Bone Metabolism in Experimental Animals. *Science of The Total Environment* **1993,** *134*, 663-669.

180.   Strain, W. H.; Berliner, W. P.; Lankau, C. A.; McEvoy, R. K.; Pories, W. J.; Greenlaw, R. H. Retention of Radioisotopes by Hair, Bone and Vascular Tissue. *Journal of Nuclear Medicine* **1964,** *5* (9), 664.

181.   Durbin, P. W. Metabolic Characteristics within a Chemical Family. *Health Physics* **1959,** *2* (3), 225-238.

182.   Furchner, J. E.; Drake, G. A. Comparative Metabolism of Radionuclides in Mammals - Vi. Retention of 95nb in the Mouse, Rat, Monkey and Dog. *Health Physics* **1971,** *21* (2).

183.   Thomas, R. G.; Lie Thomas, R.; Scott, J. K. Distribution and Excretion of Niobium Following Inhalation Exposure of Rats. *American Industrial Hygiene Association Journal* **1967,** *28* (1), 1-7.

184.   Schneidereit, M.; Kriegel, H. Comparative Distribution on Niobium-95 in Maternal and Fetal Rats and Rabbits. *Experientia* **1986,** *42* (6), 619-620.

185.   Radchenko, V.; Bouziotis, P.; Tsotakos, T.; Paravatou-Petsotas, M.; la Fuente, A. d.; Loudos, G.; Harris, A. L.; Xanthopoulos, S.; Filosofov, D.; Hauser, H.; Eisenhut, M.; Ponsard, B.; Roesch, F. Labeling and Preliminary in Vivo Assessment of Niobium-Labeled Radioactive Species: A Proof-of-Concept Study. *Nuclear Medicine and Biology* **2016,** *43* (5), 280-287.

186.   Matthews, C. M.; Gartside, J. M. Tumour Uptake and Distribution of Niobium Isotopes in Rats. *British Journal of Cancer* **1965,** *19* (3), 551-559.

187.   Hamilton, J. G. The Metabolic Properties of the Fission Products and Actinide Elements. *Reviews of Modern Physics* **1948,** *20* (4), 718-728.

188.   Mraz, F. R.; Eisele, G. R. Gastrointestinal Absorption, Tissue Distribution, and Excretion of 95nb in Newborn and Weanling Swine and Sheep. *Radiation Research* **1977,** *72* (3), 533-536.

189.   Mraz, F. R.; Eisele, G. R. Gastrointestinal Absorption of 95nb by Rats of Different Ages. *Radiation Research* **1977,** *69* (3), 591-593.

190.   Ando, A.; Ando, I. Biodistribution of 95nb and 182ta in Tumor-Bearing Animals and Mechanisms for Accumulation in Tumor and Liver. *Journal of Radiation Research* **1990,** *31* (1), 97-109.

191.   Ando, A.; Ando, I.; Hiraki, T.; Hisada, K. Relation between the Location of Elements in the Periodic Table and Various Organ-Uptake Rates. *International Journal of Radiation Applications and Instrumentation. Part B. Nuclear Medicine and Biology* **1989,** *16* (1), 57-80.

192.   Shannon, R. Revised Effective Ionic Radii and Systematic Studies of Interatomic Distances in Halides and Chalcogenides. *Acta Crystallographica Section A* **1976,** *32* (5), 751-767.

193.   Fleshman, D. G.; Silva, A. J.; Shore, B. The Metabolism of Tantalum in the Rat. *Health Phys* **1971,** *21* (3), 385-92.

194.   Hiller, M. M.; Leggett, R. W. A Biokinetic Model for Trivalent or Hexavalent Chromium in Adult Humans. *Journal of Radiological Protection* **2019,** *40* (1), 19-39.

195.   Anderson, R. A. Chromium as an Essential Nutrient for Humans. *Regulatory Toxicology and Pharmacology* **1997,** *26* (1), S35-S41.

196.   Sayato, Y.; Nakamuro, K.; Matsui, S.; Ando, M. Metabolic Fate of Chromium Compounds. I. Comparitive Behavior of Chromium in Rate Administered with Na2cro4 and Crcl3. *Journal of Pharmacobio-Dynamics* **1980,** *3* (1), 17-23.

197.   Hopkins, L. L. Distribution in the Rat of Physiological Amounts of Injected Cr51(Iii) with Time. *American Journal of Physiology-Legacy Content* **1965,** *209* (4), 731-735.

198.   Kargacin, B.; Squibb, K. S.; Cosentino, S.; Zhitkovich, A.; Costa, M. Comparison of the Uptake and Distribution of Chromate in Rats and Mice. *Biological Trace Element Research* **1993,** *36* (3), 307.

199.   Witmer, C.; Harris, R.; Shupack, S. Chromium Content of Bone after Oral and Intraperitoneal (Ip) Administration of Chromium (Vi) to Rats. *Toxicologist* **1991,** *11*, 41.

200. Weber, H. Long-Term Study of the Distribution of Soluble Chromate-51 in the Rat after a Single Intratracheal Administration. *Journal of Toxicology and Environmental Health* **1983,** *11* (4-6), 749-764.

201. Sutherland, J. E.; Zhitkovich, A.; Kluz, T.; Costa, M. Rats Retain Chromium in Tissues Following Chronic Ingestion of Drinking Water Containing Hexavalent Chromium. *Biological Trace Element Research* **2000,** *74* (1), 41.

202. Kraintz, L.; Talmage, R. V. Distribution of Radioactivity Following Intravenous Administration of Trivalent Chromium 51 in the Rat and Rabbit. *Proceedings of the Society for Experimental Biology and Medicine* **1952,** *81* (2), 490-492.

203. Kirman, C. R.; Hays, S. M.; Aylward, L. L.; Suh, M.; Harris, M. A.; Thompson, C. M.; Haws, L. C.; Proctor, D. M. Physiologically Based Pharmacokinetic Model for Rats and Mice Orally Exposed to Chromium. *Chemico-Biological Interactions* **2012,** *200* (1), 45-64.

204. O'Flaherty, E. J.; Kerger, B. D.; Hays, S. M.; Paustenbach, D. J. A Physiologically Based Model for the Ingestion of Chromium(Iii) and Chromium(Vi) by Humans. *Toxicological Sciences* **2001,** *60* (2), 196-213.

205. Age-Dependent Doses to Members of the Public from Intake of Radionuclides: Part 2 Ingestion Dose Coefficients. *ICRP PUBLICATION* **1993,** *23* (3/4 Part 67), ALL.

206. Giussani, A. A Recycling Systemic Model for the Biokinetics of Molybdenum Radionuclides. *Science of The Total Environment* **2008,** *404* (1), 44-55.

207. Schroeder, H. A.; Balassa, J. J.; Tipton, I. H. Essential Trace Metals in Man: Molybdenum. *Journal of Chronic Diseases* **1970,** *23* (7), 481-499.

208. Sumino, K.; Hayakawa, K.; Shibata, T.; Kitamura, S. Heavy Metals in Normal Japanese Tissues. *Archives of Environmental Health: An International Journal* **1975,** *30* (10), 487-494.

209. Yoo, Y. C.; Ki Lee, S.; Yeol Yang, J.; Whan In, S.; Wook Kim, K.; Hyuck Chung, K.; Gyu Chung, M.; Young Choung, S. Organ Distribution of Heavy Metals in Autopsy Material from Normal Korean. *Journal of Health Science* **2002,** *48* (2), 186-194.

210. Neilands, J. B.; Strong, F. M.; Elvehjem, C. A. Molybdenum in the Nutrition of the Rat. *Journal of Biological Chemistry* **1948,** *172* (2), 431-439.

211. Rosoff, B.; Spencer, H. The Distribution and Excretion of Molybdenum-99 in Mice. *Health Phys* **1973,** *25* (2), 173-5.

212. Comar, C. L.; Singer, L.; Davis, G. K. Molybdenum Metabolism and Interrelationships with Copper and Phosphorus. *Journal of Biological Chemistry* **1949,** *180* (2), 913-922.

213.	Keith, L. S.; Moffett, D. B.; Rosemond, Z. A.; Wohlers, D. W. Atsdr Evaluation of Health Effects of Tungsten and Relevance to Public Health. *Toxicology and Industrial Health* **2007,** *23* (5-6), 347-387.

214.	Guandalini, G. S.; Zhang, L.; Fornero, E.; Centeno, J. A.; Mokashi, V. P.; Ortiz, P. A.; Stockelman, M. D.; Osterburg, A. R.; Chapman, G. G. Tissue Distribution of Tungsten in Mice Following Oral Exposure to Sodium Tungstate. *Chemical Research in Toxicology* **2011,** *24* (4), 488-493.

215.	Weber, W. M.; Marr, R.; Kracko, D.; Gao, Z.; McDonald, J. D.; Ui Chearnaigh, K. Disposition of Tungsten in Rodents after Repeat Oral and Drinking Water Exposures. *Toxicological & Environmental Chemistry* **2008,** *90* (3), 445-455.

216.	McDonald, J. D.; Weber, W. M.; Marr, R.; Kracko, D.; Khain, H.; Arimoto, R. Disposition and Clearance of Tungsten after Single-Dose Oral and Intravenous Exposure in Rodents. *Journal of Toxicology and Environmental Health, Part A* **2007,** *70* (10), 829-836.

217.	Lagarde, F.; Leroy, M. Metabolism and Toxicity of Tungsten in Humans and Animals. *Metal Ions in Biological Systems* **2002,** *39*, 741-59.

218.	Kelly, A. D. R.; Lemaire, M.; Young, Y. K.; Eustache, J. H.; Guilbert, C.; Molina, M. F.; Mann, K. K. In Vivo Tungsten Exposure Alters B-Cell Development and Increases DNA Damage in Murine Bone Marrow. *Toxicological Sciences* **2012,** *131* (2), 434-446.

219.	Wentworth, R. A. D. Mechanisms for the Reactions of Molybdenum in Enzymes. *Coordination Chemistry Reviews* **1976,** *18* (1), 1-27.

220.	Bawden, J. W.; Hammarström, L. E. Autoradiography of 99mo in Developing Rat Teeth and Bone. *European Journal of Oral Sciences* **1976,** *84* (3), 168-174.

221.	Pejović-Milić, A.; Aslam; Chettle, D. R.; Oudyk, J.; Pysklywec, M. W.; Haines, T. Bone Manganese as a Biomarker of Manganese Exposure: A Feasibility Study. *American Journal of Industrial Medicine* **2009,** *52* (10), 742-750.

222.	Andersen, M. E.; Gearhart, J. M.; Clewell, H. J. Pharmacokinetic Data Needs to Support Risk Assessments for Inhaled and Ingested Manganese. *Neurotoxicology* **1999,** *20* (2-3), 161-171.

223.	Scheuhammer, A. M.; Cherian, M. G. The Influence of Manganese on the Distribution of Essential Trace Elements. Ii. The Tissue Distribution of Manganese, Magnesium, Zinc, Iron, and Copper in Rats after Chronic Manganese Exposure. *Journal of Toxicology and Environmental Health* **1983,** *12* (2-3), 361-370.

224.	Furchner, J. E.; Richmond, C. R.; Drake, G. A. Comparative Metabolism of Radionuclides in Mammals-Iii Retention of Manganese-54 in the Mouse, Rat, Monkey and Dog. *Health Physics* **1966,** *12* (10).

225. O'Neal, S. L.; Hong, L.; Fu, S.; Jiang, W.; Jones, A.; Nie, L. H.; Zheng, W. Manganese Accumulation in Bone Following Chronic Exposure in Rats: Steady-State Concentration and Half-Life in Bone. *Toxicology Letters* **2014,** *229* (1), 93-100.

226. Budis, H.; Kalisinska, E.; Lanocha, N.; Kosik-Bogacka, D. I. The Concentration of Manganese, Iron and Strontium in Bone of Red Fox Vulpes Vulpes (L. 1758). *Biological Trace Element Research* **2013,** *155* (3), 361-369.

227. Brodziak-Dopierała, B.; Kwapuliński, J.; Sobczyk, K.; Wiechuła, D. The Content of Manganese and Iron in Hip Joint Tissue. *Journal of Trace Elements in Medicine and Biology* **2013,** *27* (3), 208-212.

228. Leggett, R. W. A Biokinetic Model for Manganese. *Science of The Total Environment* **2011,** *409* (20), 4179-4186.

229. Leggett, R.; Giussani, A. A Biokinetic Model for Systemic Technetium in Adult Humans. *Journal of Radiological Protection* **2015,** *35* (2), 297-315.

230. Jones, B. Metabolism of Technetium in Goats. *The International Journal of Applied Radiation and Isotopes* **1983,** *34* (5), 837-839.

231. Samuel, S. V.; Elaine, A. C. L.; Gláucio, F. D.; Mário, B.-F.; Luís Cristóvão, P. Sodium Pertechnetate (Na99mtco4) Biodistribution in Mice Exposed to Cigarette Smoke. *BMC Medical Physics* **2005,** *5* (1), 1.

232. Matthews, C. M. E.; Mallard, J. R. Distribution of 99mtc and Tumour/Brain Concentrations in Rats. *Journal of Nuclear Medicine* **1965,** *6*, 404-408.

233. Gerber, G. B.; van Hees, M.; Garten, C. T., Jr.; Vandecasteele, C. M.; Vankerkom, J.; van Bruwaene, R.; Kirchmann, R.; Colard, J.; Cogneau, M. Technetium Absorption and Turnover in Monogastric and Polygastric Animals. *Health Physics* **1989,** *57* (2), 315-9.

234. Holm, E.; Rioseco, J. 99tc in the Sub-Arctic Food Chain Lichen-Reindeer-Man. *Journal of Environmental Radioactivity* **1987,** *5* (5), 343-357.

235. Zuckier, L. S.; Dohan, O.; Li, Y.; Chang, C. J.; Carrasco, N.; Dadachova, E. Kinetics of Perrhenate Uptake and Comparative Biodistribution of Perrhenate, Pertechnetate, and Iodide by Nai Symporter–Expressing Tissues in Vivo. *Journal of Nuclear Medicine* **2004,** *45* (3), 500.

236. Hoerth, R. M.; Katunar, M. R.; Gomez Sanchez, A.; Orellano, J. C.; Ceré, S. M.; Wagermaier, W.; Ballarre, J. A Comparative Study of Zirconium and Titanium Implants in Rat: Osseointegration and Bone Material Quality. *Journal of Materials Science: Materials in Medicine* **2014,** *25* (2), 411-422.

237. Olmedo, D. G.; Tasat, D. R.; Guglielmotti, M. B.; Cabrini, R. L. Biodistribution of Titanium Dioxide from Biologic Compartments. *Journal of Materials Science: Materials in Medicine* **2008,** *19* (9), 3049-3056.

238. Buly, R. L.; Huo, M. H.; Salvati, E.; Brien, W.; Bansal, M. Titanium Wear Debris in Failed Cemented Total Hip Arthroplasty: An Analysis of 71 Cases. *The Journal of Arthroplasty* **1992,** *7* (3), 315-323.

239. Stulberg, B. N.; Merritt, K.; Bauer, T. W. Metallic Wear Debris in Metal-Backed Patellar Failure. *Journal of Applied Biomaterials* **1994,** *5* (1), 9-16.

240. Agins, H. J.; Alcock, N. W.; Bansal, M.; Salvati, E. A.; Wilson, P. D., Jr.; Pellicci, P. M.; Bullough, P. G. Metallic Wear in Failed Titanium-Alloy Total Hip Replacements. A Histological and Quantitative Analysis. *The Journal of Bone and Joint Surgery* **1988,** *70* (3).

241. Meachim, G.; Williams, D. F. Changes in Nonosseous Tissue Adjacent to Titanium Implants. *Journal of Biomedical Materials Research* **1973,** *7* (6), 555-572.

242. Passi, P.; Zadro, A.; Galassini, S.; Rossi, P.; Moschini, G. Pixe Micro-Beam Mapping of Metals in Human Peri-Implant Tissues. *Journal of Materials Science: Materials in Medicine* **2002,** *13* (11), 1083-1089.

243. Ektessabi, A. M.; Otsuka, T.; Tsuboi, Y.; Horino, Y.; Mokuno, Y.; Fujii, K.; Albrektsson, T.; Sennerby, L.; Johansson, C. Preliminary Experimental Results on Mapping of the Elemental Distribution of the Organic Tissues Surrounding Titanium-Alloy Implants. *Nuclear Instruments and Methods in Physics Research Section B: Beam Interactions with Materials and Atoms* **1996,** *109-110*, 278-283.

244. Ducheyne, P.; Willems, G.; Martens, M.; Helsen, J. In Vivo Metal-Ion Release from Porous Titanium-Fiber Material. *Journal of Biomedical Materials Research* **1984,** *18* (3), 293-308.

245. Grosse, S.; Haugland, H. K.; Lilleng, P.; Ellison, P.; Hallan, G.; Høl, P. J. Wear Particles and Ions from Cemented and Uncemented Titanium-Based Hip Prostheses—a Histological and Chemical Analysis of Retrieval Material. *Journal of Biomedical Materials Research Part B: Applied Biomaterials* **2015,** *103* (3), 709-717.

246. Cvijović-Alagić, I.; Cvijović, Z.; Bajat, J.; Rakin, M. Electrochemical Behaviour of Ti-6al-4v Alloy with Different Microstructures in a Simulated Bio-Environment. *Materials and Corrosion* **2016,** *67* (10), 1075-1087.

247. Ektessabi, A.; Shikine, S.; Kitamura, N.; Rokkum, M.; Johansson, C. Distribution and Chemical States of Iron and Chromium Released from Orthopedic Implants into Human Tissues. *X-Ray Spectrometry* **2001,** *30* (1), 44-48.

248. Brodziak-Dopierała, B.; Kwapuliński, J.; Sobczyk, K.; Wiechuła, D. Chromium Content in the Human Hip Joint Tissues. *Biomedical and Environmental Sciences* **2015,** *28* (2), 89-96.

249. Hart, A. J.; Quinn, P. D.; Sampson, B.; Sandison, A.; Atkinson, K. D.; Skinner, J. A.; Powell, J. J.; Mosselmans, J. F. W. The Chemical Form of Metallic Debris in Tissues

Surrounding Metal-on-Metal Hips with Unexplained Failure. *Acta Biomaterialia* **2010,** *6* (11), 4439-4446.

250. Dorr, L. D.; Bloebaum, R. O. Y.; Emmanual, J.; Meldrum, R. Histologic, Biochemical, and Ion Analysis of Tissue and Fluids Retrieved During Total Hip Arthroplasty. *Clinical Orthopaedics and Related Research®* **1990,** *261*.

251. Etcheverry, S. B.; Williams, P. A. M.; Baran, E. J. A Spectroscopic Study of the Interaction of the Vo2+ Cation with the Two Components of Chondroitin Sulfate. *Biological Trace Element Research* **1996,** *51* (2), 169-176.

252. Etcheverry, S. B.; Williams, P. A. M.; Baran, E. J. The Interaction of the Vanadyl (Iv) Cation with Chondroitin Sulfate A. *Biological Trace Element Research* **1994,** *42* (1), 43-52.

253. Doi, Y.; Aoba, T.; Okazaki, M.; Takahashi, J.; Moriwaki, Y. Organic-Bound Chromium in Enamel, Dentin, and Bone Studied by Electron Spin Resonance. *Journal of Dental Research* **1981,** *60* (6), 1053-1056.

254. Harris, J. R.; Reiber, A.; Therese, H. A.; Tremel, W. Molybdenum Blue: Binding to Collagen Fibres and Microcrystal Formation. *Micron* **2005,** *36* (5), 387-391.

255. Bibr, B.; Deyl, Z.; Lener, J.; Adam, M. Investigation on the Reaction of Molybdenum with Collagen in Vivo. *International Journal of Peptide and Protein Research* **1977,** *10* (3), 190-196.

256. Bibr, B.; Deyl, Z.; Lener, J.; Kucera, J.; Simkova, M. The Mechanism of Action of Molybdenum and Tungsten Upon Collagen Structures in Vivo. *Physiol Bohemoslov* **1987,** *36* (5), 417-24.

257. Kusaka, Y.; Gründer, W.; Rumpel, H.; Dannhauer, K. H.; Gersonde, K. Mr Microimaging of Articular Cartilage and Contrast Enhancement by Manganese Ions. *Magnetic Resonance in Medicine* **1992,** *24* (1), 137-148.

258. Rey, C.; Combes, C.; Drouet, C.; Cazalbou, S.; Grossin, D.; Brouillet, F.; Sarda, S. Surface Properties of Biomimetic Nanocrystalline Apatites; Applications in Biomaterials. *Progress in Crystal Growth and Characterization of Materials* **2014,** *60* (3), 63-73.

259. Cazalbou, S.; Combes, C.; Eichert, D.; Rey, C.; Glimcher, M. J. Poorly Crystalline Apatites: Evolution and Maturation in Vitro and in Vivo. *Journal of Bone and Mineral Metabolism* **2004,** *22* (4), 310-317.

260. Wang, J.; Bourgeois, D.; Meyer, D. Mimicking Bone–Metal Exchanges with Synthetic Nanocrystalline Apatites. *Materials Advances* **2020,** *1* (9), 3292-3301.

261. Cazalbou, S.; Eichert, D.; Ranz, X.; Drouet, C.; Combes, C.; Harmand, M. F.; Rey, C. Ion Exchanges in Apatites for Biomedical Application. *Journal of Materials Science: Materials in Medicine* **2005,** *16* (5), 405-409.

262. Badillo-Almaraz, V. E.; Ly, J. Calcium Sorption on Hydroxyapatite in Aqueous Solutions: Reversible and Nonreversible Components. *Journal of Colloid and Interface Science* **2003,** *258* (1), 27-32.

263. Haider, A.; Haider, S.; Han, S. S.; Kang, I.-K. Recent Advances in the Synthesis, Functionalization and Biomedical Applications of Hydroxyapatite: A Review. *RSC Advances* **2017,** *7* (13), 7442-7458.

264. Galow, A.-M.; Rebl, A.; Koczan, D.; Bonk, S. M.; Baumann, W.; Gimsa, J. Increased Osteoblast Viability at Alkaline Ph in Vitro Provides a New Perspective on Bone Regeneration. *Biochemistry and biophysics reports* **2017,** *10,* 17-25.

265. Tite, T.; Popa, A.-C.; Balescu, L. M.; Bogdan, I. M.; Pasuk, I.; Ferreira, J. M. F.; Stan, G. E. Cationic Substitutions in Hydroxyapatite: Current Status of the Derived Biofunctional Effects and Their in Vitro Interrogation Methods. *Materials* **2018,** *11* (11), 2081.

266. Ribeiro, C. C.; Barbosa, M. A.; Machado, A. A. S. C.; Tudor, A.; Davies, M. C. Modifications in the Molecular Structure of Hydroxyapatite Induced by Titanium Ions. *Journal of Materials Science: Materials in Medicine* **1995,** *6* (12), 829-834.

267. Ribeiro, C. C.; Gibson, I.; Barbosa, M. A. The Uptake of Titanium Ions by Hydroxyapatite Particles—Structural Changes and Possible Mechanisms. *Biomaterials* **2006,** *27* (9), 1749-1761.

268. Smirnov, V. V.; Antonova, O. S.; Smirnov, S. V.; Goldberg, M. A.; Komlev, V. S.; Barinov, S. M. Effect of Titanium and Zirconium Substitutions for Calcium on the Formation and Structure of Tricalcium Phosphate and Hydroxyapatite. *Inorganic Materials* **2017,** *53* (12), 1254-1260.

269. Chen, M.-H.; Hanagata, N.; Ikoma, T.; Huang, J.-Y.; Li, K.-Y.; Lin, C.-P.; Lin, F.-H. Hafnium-Doped Hydroxyapatite Nanoparticles with Ionizing Radiation for Lung Cancer Treatment. *Acta Biomaterialia* **2016,** *37,* 165-173.

270. Lima, T. A. R. M.; Brito, N. S.; Peixoto, J. A.; Valerio, M. E. G. The Incorporation of Chromium (Iii) into Hydroxyapatite Crystals. *Materials Letters* **2015,** *140,* 187-191.

271. Hughes, J. M.; Cameron, M.; Crowley, K. D. Ordering of Divalent Cations in the Apatite Structure: Crystal Structure Refinements of Natural Mn- and Sr-Bearing Apatite. *American Mineralogist* **1991,** *76* (11-12), 1857-1862.

272. Kasai, P. H. Electron Paramagnetic Resonance Study of Mn++ Ion in Polycrystalline Calcium Fluorophosphate. *The Journal of Physical Chemistry* **1962,** *66* (4), 674-680.

273. Pon-On, W.; Meejoo, S.; Tang, I. M. Substitution of Manganese and Iron into Hydroxyapatite: Core/Shell Nanoparticles. *Materials Research Bulletin* **2008,** *43* (8), 2137-2144.

274. Sutter, B.; Wasowicz, T.; Howard, T.; Hossner, L. R.; Ming, D. W. Characterization of Iron, Manganese, and Copper Synthetic Hydroxyapatites by Electron Paramagnetic Resonance Spectroscopy. *Soil Science Society of America Journal* **2002,** *66* (4), 1359-1366.

275. Sutter, B.; Ming, D. W.; Clearfield, A.; Hossner, L. R. Mineralogical and Chemical Characterization of Iron-, Manganese-, and Copper-Containing Synthetic Hydroxyapatites. *Soil Science Society of America Journal* **2003,** *67* (6), 1935-1942.

276. Warren, R. W. Epr of Mn2+ in Calcium Fluorophosphate. I. The Ca(Ii) Site. *Physical Review B* **1970,** *2* (11), 4383-4388.

277. Ohkubo, Y. Epr Spectra of Mn2+ Ions in Synthetic Calcium Fluoro-Chloro Phosphates. *Journal of Applied Physics* **1968,** *39* (11), 5344-5345.

278. Warren, R. W.; Mazelsky, R. Esr of Mn+ in Calcium Fluorophosphate. Ii. Modified Ca(Ii) Sites. *Physical Review B* **1974,** *10* (1), 19-25.

279. Medvecký, Ľ.; Štulajterová, R.; Parilák, Ľ.; Trpčevská, J.; Ďurišin, J.; Barinov, S. M. Influence of Manganese on Stability and Particle Growth of Hydroxyapatite in Simulated Body Fluid. *Colloids and Surfaces A: Physicochemical and Engineering Aspects* **2006,** *281* (1), 221-229.

280. Narasaraju, T. S. B.; Phebe, D. E. Some Physico-Chemical Aspects of Hydroxylapatite. *Journal of Materials Science* **1996,** *31* (1), 1-21.

281. George, G.; Gupta, S. K.; Rao, P. V. R.; Narasaraju, T. S. B. Preparation and Characterization of Phosphate and Arsenate Apatites of Strontium and Their Solid Solutions. *Journal of Materials Science* **1987,** *22* (6), 2274-2276.

282. Fleshman, D.; Krokz, S.; Silva, A. The Metabolism of Elements of High Atomic Number. *Univ. Calif. Radiat. Lab* **1966,** *14739*, 69-86.

283. Gupta, S. K.; Rao, P. V. R.; George, G.; Narasaraju, T. S. B. Determination of Solubility Products of Phosphate and Vanadate Apatites of Calcium and Their Solid Solutions. *Journal of Materials Science* **1987,** *22* (4), 1286-1290.

284. Kaneda, K.; Hara, T.; Hashimoto, N.; Mitsudome, T.; Mizugaki, T.; Jitsukawa, K. Creation of a Monomeric Vanadate Species in an Apatite Framework as an Active Heterogeneous Base Catalyst for Michael Reactions in Water. *Catalysis Today* **2010,** *152* (1), 93-98.

285. Petit, S.; Gode, T.; Thomas, C.; Dzwigaj, S.; Millot, Y.; Brouri, D.; Krafft, J.-M.; Rousse, G.; Laberty-Robert, C.; Costentin, G. Incorporation of Vanadium into the Framework of Hydroxyapatites: Importance of the Vanadium Content and Ph Conditions During the Precipitation Step. *Physical Chemistry Chemical Physics* **2017,** *19* (14), 9630-9640.

286. Boechat, C. B.; Eon, J.-G.; Rossi, A. M.; de Castro Perez, C. A.; da Silva San Gil, R. A. Structure of Vanadate in Calcium Phosphate and Vanadate Apatite Solid Solutions. *Physical Chemistry Chemical Physics* **2000,** *2* (18), 4225-4230.

287. Capanema, N. S. V.; Mansur, A. A. P.; Carvalho, S. M.; Silva, A. R. P.; Ciminelli, V. S.; Mansur, H. S. Niobium-Doped Hydroxyapatite Bioceramics: Synthesis, Characterization and in Vitro Cytocompatibility. *Materials (Basel, Switzerland)* **2015,** *8* (7), 4191-4209.

288. Tamai, M.; Isama, K.; Nakaoka, R.; Tsuchiya, T. Synthesis of a Novel B-Tricalcium Phosphate/Hydroxyapatite Biphasic Calcium Phosphate Containing Niobium Ions and Evaluation of Its Osteogenic Properties. *Journal of Artificial Organs* **2007,** *10* (1), 22-28.

289. Baradaran, S.; Nasiri-Tabrizi, B.; Shirazi, F. S.; Saber-Samandari, S.; Shahtalebi, S.; Basirun, W. J. Wet Chemistry Approach to the Preparation of Tantalum-Doped Hydroxyapatite: Dopant Content Effects. *Ceramics International* **2018,** *44* (3), 2768-2781.

290. Jehng, J.-M.; Wachs, I. E. Niobium Oxide Solution Chemistry. *Journal of Raman Spectroscopy* **1991,** *22* (2), 83-89.

291. Kalniņa, D.; Levina, A.; Pei, A.; Gross, K. A.; Lay, P. A. Synthesis, Characterization and in Vitro Anti-Cancer Activity of Vanadium-Doped Nanocrystalline Hydroxyapatite. *New Journal of Chemistry* **2019,** *43* (45), 17891-17901.

292. Fukui, K.; Fujisawa, Y.; Ohya-Nishiguchi, H.; Kamada, H.; Sakurai, H. In Vivo Coordination Structural Changes of a Potent Insulin-Mimetic Agent, Bis(Picolinato)Oxovanadium(Iv), Studied by Electron Spin-Echo Envelope Modulation Spectroscopy. *Journal of Inorganic Biochemistry* **1999,** *77* (3), 215-224.

293. Vega, E. D.; Pedregosa, J. C.; Narda, G. E. Interaction of Oxovanadium(Iv) with Crystalline Calcium Hydroxyapatite: Surface Mechanism with No Structural Modification. *Journal of Physics and Chemistry of Solids* **1999,** *60* (6), 759-766.

294. Dikanov, S. A.; Liboiron, B. D.; Thompson, K. H.; Vera, E.; Yuen, V. G.; McNeill, J. H.; Orvig, C. In Vivo Electron Spin−Echo Envelope Modulation (Eseem) Spectroscopy: First Observation of Vanadyl Coordination to Phosphate in Bone. *Journal of the American Chemical Society* **1999,** *121* (47), 11004-11005.

295. Dikanov, S. A.; Liboiron, B. D.; Orvig, C. Two-Dimensional (2d) Pulsed Electron Paramagnetic Resonance Study of Vo2+−Triphosphate Interactions: Evidence for Tridentate Triphosphate Coordination, and Relevance to Bone Uptake and Insulin Enhancement by Vanadium Pharmaceuticals. *Journal of the American Chemical Society* **2002,** *124* (12), 2969-2978.

296. Dikanov, S. A.; Liboiron, B. D.; Orvig, C. Vo2+–Hydroxyapatite Complexes as Models for Vanadyl Coordination to Phosphate in Bone. *Molecular Physics* **2013,** *111* (18-19), 2967-2979.

297. Afolaranmi, G. A.; Tettey, J. N. A.; Murray, H. M.; Meek, R. M. D.; Grant, M. H. The Effect of Anticoagulants on the Distribution of Chromium Vi in Blood Fractions. *The Journal of Arthroplasty* **2010,** *25* (1), 118-120.

298. Merritt, K.; Brown, S. A. Release of Hexavalent Chromium from Corrosion of Stainless Steel and Cobalt—Chromium Alloys. *Journal of Biomedical Materials Research* **1995,** *29* (5), 627-633.

299. Bolt, A. M.; Grant, M. P.; Wu, T. H.; Flores Molina, M.; Plourde, D.; Kelly, A. D. R.; Negro Silva, L. F.; Lemaire, M.; Schlezinger, J. J.; Mwale, F.; Mann, K. K. Tungsten Promotes Sex-Specific Adipogenesis in the Bone by Altering Differentiation of Bone Marrow-Resident Mesenchymal Stromal Cells. *Toxicological Sciences* **2016,** *150* (2), 333-346.

Chapter 2. Accumulation of Persistent Tungsten in Bone as *in situ* Generated Polytungstate

2.1. Preface

As described in Chapter 1, despite the clear demonstration of metal uptake into bone, little is known about how, or in what form, these metals accumulate. The aqueous chemistry of the early transition metals, specifically Group 5 and 6 metals, is complex. *In vivo* and *in situ* investigations are thus required to accurately determine metal distribution and speciation in bone.

In the following chapter, the distribution and speciation of Group 6 metal tungsten in bone is explored *in situ* using synchrotron radiation micro X-ray fluorescence (SR-μXRF) spectroscopy and micro X-ray absorption spectroscopy (μXAS) techniques. This work was published in *Communications Chemistry* (**2018**, 1:8). Data from Supplementary Information has been incorporated into the chapter.

2.2. Introduction

Tungsten is the only third row transition metal with a recognized natural bioinorganic chemistry.[1] The prevalent belief that it is innocuous, coupled with its many unique properties, has led to the pervasive adoption of tungsten in a surprising range of technologies.[2, 3] However, the recent association of a cluster of acute childhood lymphocytic leukemia cases in Fallon, Nevada, with elevated levels of tungsten in the community's ground water[4], has led to a reappraisal of its potential toxicity. As there remains a lack of toxicological data, tungsten was nominated as an emerging contaminant for further investigation by the US Environmental Protection Agency and National Toxicity Program.

When mice ingest solubilized tungsten in the form of orthotungstate (WO_4^{2-}), it rapidly accumulates in their bones.[5] Other bone-accumulating metals, such as lead and strontium,[6] substitute for calcium in hydroxyapatite, the calcium-phosphate matrix of bone, and can be removed using standard chelation therapy.[7] This treatment, however, is ineffective at removing anionic oxometallate anions of tungsten, which is retained in cortical bone tissue even after the source is removed.[3, 8] This suggests alternate speciation or accumulation mechanisms for tungsten

compared to other metals. To both understand the biological implications of accumulation and develop an effective treatment strategy, it is essential to determine if there is selective deposition in particular regions of bone tissue, as well as to establish the chemical form therein. Tungsten deposition may have a variety of detrimental consequences, specific to the type of bone tissue in which it is present.

Here we use synchrotron radiation micro X-ray fluorescence (SR-μXRF) spectroscopy and micro X-ray absorption near edge structure (μXANES) spectroscopy to show that tungsten is heterogeneously distributed in bone tissue and that the *in vivo* speciation of tungsten is in the form of *in situ* generated polytungstates.

2.3. Experimental

2.3.1. In vivo *Tungsten Exposure*

Animal experiments were performed under a McGill University Animal Care Committee approved protocol. Four-week-old male C57BL/6J mice were purchased from Charles Rivers Laboratories Inc. (Montréal, Quebéc) or bred in house and were given food and water *ad libitum*. After 1 week of acclimation, mice were divided into two treatment groups: control tap water or 1000mg/L tungsten. Mice were exposed for 1, 4 or 12 weeks. An additional study compared removal of tungsten for 8 weeks, following a 4-week exposure to 1000 mg/L tungsten. For studies where mice were exposed to 1000 mg/L tungsten, the appropriate amount of sodium tungstate dihydrate ($Na_2WO_4 \cdot 2H_2O$; Sigma- Aldrich) was dissolved in tap water and was replaced every 2 or 3 days to limit conversion to polytungstates. As we have previously published[8] no changes in animal weight, physical appearance, or water intake were observed in the tungsten-exposed group.

2.3.2. Bone Preparation for Cross-Sections.

Mice were euthanized by CO_2 asphyxiation followed by cardiac puncture or cervical dislocation. Tibia and femur bones were removed, bone marrow was flushed and the samples were stored at -80°C. To mount the samples, bones were cut in half, washed with 70%, 80%, 90%, 100% absolute alcohol followed by two washes with xylene and three washes of methyl methacrylate (MMA) before finally being set in MMA. 10μm cross-sections were cut using a diamond blade and set on Kapton tape for SR-μXRF measurement.

2.3.3. Bone Preparation for all Other Samples

Mice were euthanized by CO_2 asphyxiation followed by cardiac puncture or cervical dislocation. Tibia and femur bones were removed and the bones were placed for one week in a solution of 4% paraformaldehyde for fixation. Bones were then washed three times with a solution of 1% phosphate-buffered solution (PBS) at pH 7.4 and stored in the same solution. To mount the samples, bones were dehydrated using a series of alcohol washes followed by washes with xylene and MMA before finally being set in MMA. Using a diamond saw, samples were cut longitudinally before being polished using 600 grit silicon carbide paper and 6 μm and 1 μm diamond suspension. The surfaces were then carbon coated for backscattered electron imaging (BEI). Following measurement, thin sections of the samples were prepared by cutting with a diamond saw and further grinding down the back of the samples with 120 grit silicon carbide paper, leaving the surface untouched for SR-μXRF measurement. This preparation technique allowed for visualization of the surface using BEI, which was essential for comparing XRF maps to bone morphology. However, it also resulted in minute variations in sample thickness which made quantitative determinations of local concentration difficult due to difference in illuminated volume across the sample.

2.3.4. Backscattered Electron Imaging

Backscattered Electron Imaging experiments were done on a FEI Inspect F50 FE-SEM with EDAX Octane Super 60 mm2 SDD and TEAM EDS Analysis System. The BEI indicates the presence of dense, calcium-containing cortical and cancellous matrix but does not display lighter organic cartilage and bone marrow.

2.3.5. SR-μXRF and μXANES

SR-μXRF measurements in various modes were performed at two different synchrotron radiation facilities to study the (trace) elemental distribution in tibia and femur bone tissue. Control as well as 1- and 4-week tungsten-exposed samples were measured at the Canadian Light Source (CLS) in Saskatoon, Canada. Samples exposed to tungsten for 12 weeks continually and tungsten for 4 weeks followed by 8 weeks of tap water and were measured at the National Synchrotron Light Source II (NSLS-II) in Upton, USA. SR-μXRF experiments were carried out at the VESPERS beamline at CLS and at the 5ID beamline at NSLS-II. *In vivo* L_3-edge tungsten μ-

XANES spectra were collected at the SRX beamline, on bone samples at different eight locations (Figure 2.6). Owing to the observed congruency, all eight recorded spectra were merged using the Athena software package.

All SR-μXRF measurements on the VESPERS beamline at CLS were performed using the polychromatic incident beam ("pink beam" mode), which covered the energy range of 5-30 keV and with a beam size of 3 μm. Samples were mounted on a motorized stage at 45° angle in respect to the incident X-ray beam. A 4-element silicon drift Vortex detector was used to collect the XRF spectra, which was placed in the horizontal polarization plane at 90° to the incident X-ray beam (and 45° to the sample) with a sample-to-detector distance of 50 mm. The SR-μXRF maps were generated from deadtime-corrected XRF spectra with normalization to the flux of incident X-ray beam measured by an ion chamber.

The sub-micron resolution X-ray spectroscopy (SRX) beamline, located at 5-ID of the NSLS-II, is fed by an in-vacuum undulator. The high-brightness white beam is incident upon a harmonic rejection mirror and then into a fixed-exit Si(111) double-crystal monochromator, both of which deflect the beam horizontally. The monochromatic X-ray beam passes through a secondary source plane (In the "high flux" mode, the harmonic rejection mirror is bent to produce a ~70 micron image of the primary source in this plane, while in the "high energy resolution" mode, the mirror is flattened and an aperture forms the secondary source in the horizontal direction. The current work was performed in the "high-flux" geometry, which serves as the effective source for the final focusing optics, a Kirkpatrick-Baez mirror pair. These fixed-figure mirrors are designed to produce a slightly sub-micron X-ray spot on the sample. To collect an X-ray fluorescence map, the sample is scanned through this beam on a crossed pair of stages with a continuous travel range of 50 mm (H) x 40 mm (V) measured with a 5-nm encoder resolution. μ-XANES or EXAFS is accomplished by a coordinated motion of the undulator gap and the monochromator. The photon flux incident upon the sample is measured by an ion chamber, the fluorescence is measured by a 4-element silicon drift detector, and the transmitted flux may be measured on a diode behind the sample. All μ-XANES measurements were collected in fluorescence mode with incident energy of 12.4 keV.

VESPERS and 5-ID beamlines each had their individual advantages and disadvantages, however, their different specifications ultimately meant we could not perform quantitative comparisons between the data generated (Table S2.1.). The polychromatic beam at VESPERS

allowed the visualization of light elements such as calcium albeit with a lower detection limit. Tungsten specific incident energy and small spot size at 5-ID allowed higher limit of detection with a higher resolution and the ability to collect XANES spectra *in situ*.

2.3.6. XANES

X-ray Absorption experiments on reference samples were carried out at beamline 17C in the National Synchrotron Radiation Research Center (NSRRC), Hsinchu, Taiwan. BL17C is a wiggler beamline and photoflux is around 5×10^{10} at a 4 mm(H) × 2 mm(V) beam size. The sample was sealed in a cell with Mylar windows and the experimental beam size was 3 mm(H) × 2 mm(V). Samples were measured in transmission mode as a thin powder on film. The background subtraction and normalization of XAS data, according to $\chi(k) = [\mu(k) \times \mu_0(k)]/\Delta\mu_0(0)$, were done by the AUTOBK program;[9] where $\mu(k)$ is the measured absorption coefficient, $\mu_0(k)$ is the background, and $\Delta\mu_0(0)$ is the edge jump. The wave number is defined as $k = [2m(E-E_0)/(h/2\pi)]^{1/2}$, in which E, E_0, $h/2\pi$ and m are the photon energy, threshold energy, Planck constant, and mass of the electron, respectively. For XANES data analysis, the pre-edge peak is isolated from the normalized XAS spectrum.

Spectra were aligned using the Athena software package (v0.9.24) and second derivatives calculated using the GraphPad Prism (v6.07) software package. Energy calibration of all recorded spectra (samples and standards) was performed using a tungsten foil as the reference ($E_0 = 10207$ eV) in the Athena software package.

2.3.7. Data Processing

XRF data obtained from the NSLS-II were deconvoluted with the PyXRF software package (https://github.com/NSLS-II-HXN/PyXRF). XRF data obtained from CLS were subjected to the same analysis but were first converted into HDF5 format using an in-house python script. Data were normalized by incident beam count values and graphed in OriginPro 9. A histogram analysis was performed on the intensity data to determine upper and lower limits of SR-μXRF plots. These values were selected such as to exclude the bottom and top 0.05% of the outlying data.

2.4. Results and Discussion

2.4.1. Distribution of Tungsten in Bone Tissue

SR-μXRF is a non-destructive technique that has been applied in diverse fields including archeology, forensics, anthropology, and geology to simultaneously identify and spatially resolve multiple trace elements ranging from the macroscopic to microscopic scale.[6] While this technique has successfully been applied to probe the accumulation of several heavy metals in bone, it has not been used to determine the spatial distribution of bone-accumulated tungsten. The localized distribution of tungsten throughout all the main components of long bone tissue (cancellous, cortical and bone marrow) for mice exposed to 1000 ppm tungsten via sodium tungstate (Na_2WO_4) in drinking water over the course of 1, 4, and 12 weeks was thus determined using SR-μXRF. The spectra obtained were deconvoluted to visualize elemental distribution in each of the scanned XRF images.
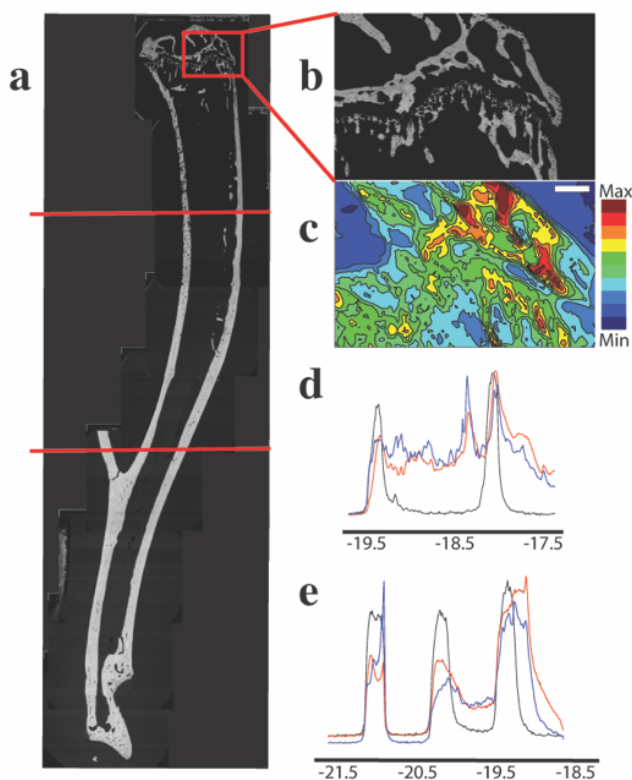
Figure 2.1. Tungsten distribution throughout mouse tibia. (a) BEI of mouse tibia after 4 weeks of exposure to 1000 ppm tungsten via Na_2WO_4 in drinking water. (b) BEI expansion of tibia head. (c) SR-μXRF map of tungsten distribution in area indicated in (b), scale bar 200 μm. (d,e) SR-μXRF linescans of the upper and lower lines marked in (a) respectively (calcium: black, tungsten: red, zinc: blue). Areas with calcium content correspond to cortical bone. X-axis is position (mm) and y-axis relative X-ray fluorescence intensity for each element. See Table S2.1 for intensity values.

With this technique, we observe localized, concentrated regions of tungsten in all of the main components of bone tissue (Figure 2.1.). These results were consistent along the length of both long bones, tibia and femur, and across all exposure times (Figure 2.2.). Tungsten was found in the marrow and cancellous tissue at the end of long bone, with intensities ~10 fold higher than background levels (Figure 2.1.c, Table S2.1). These tissues are the site of essential bone functions, such as growth and immune cell formation. Whether tungsten interferes in these processes is under investigation, however studies have shown that mice exposed to tungsten have increased DNA damage in both whole marrow and isolated B lymphocytes, a type of white blood cell.[8] Tungsten is also incorporated into cortical bone tissue (Figure 2.1.d,e and Figure 2.3), which may affect bone structure and integrity. Higher concentrations within cortical tissue compared to bone marrow indicate a mechanism of incorporation working against the concentration gradient of tungsten in blood.
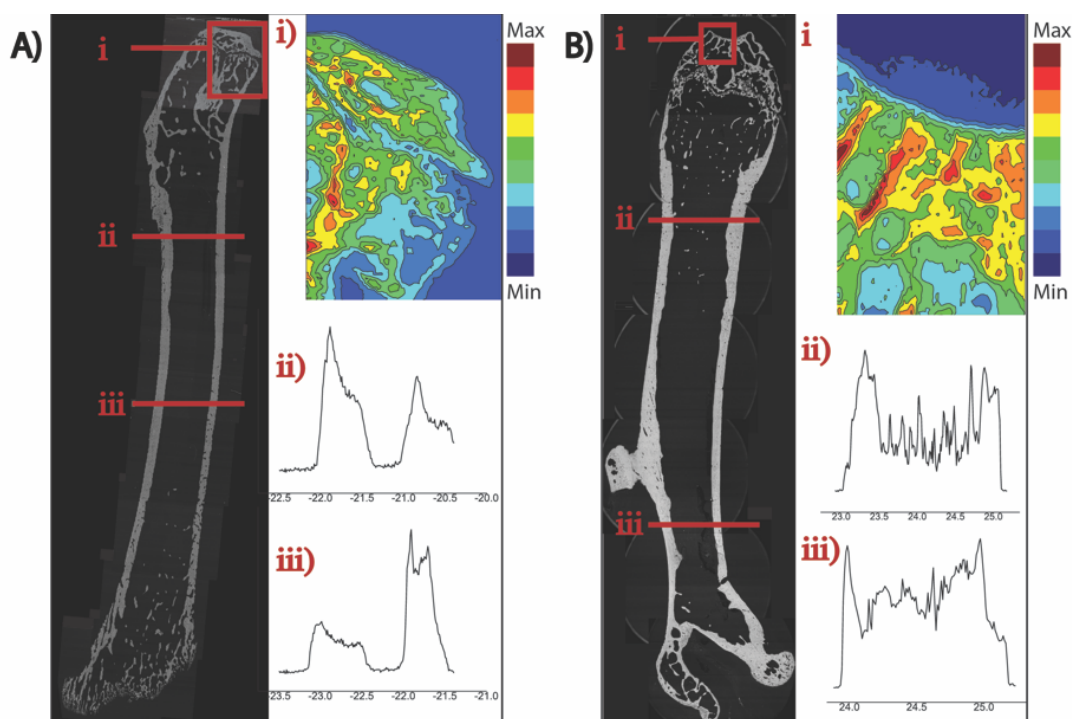
Figure 2.2. Tungsten distribution in mice exposed for (a) one week and (b) 12 weeks of 1000ppm of tungsten (Na$_2$WO$_4$) dissolved in water. SR-μXRF contour plots of the femur head (i) and linescans of the femur shaft (ii, iii) are indicated on the BEI image. See Table S2.1. for intensity values.

The heterogeneity of tungsten deposition has important implications for the mechanism of uptake. This localization is particularly evident when comparing the calcium (Figure 2.3.a,b) and tungsten (Figure 2.3.c,d) distributions of a tibia shaft cross-section after four weeks of tungsten

exposure (bone marrow removed). Calcium displays a relatively uniform distribution, which arises due to the prominent distribution of calcium in hydroxyapatite.[6] However, while calcium and most other trace elements detected with SR-μXRF display uniform distribution (Figure S2.1.), tungsten's unique localized deposition suggests that tungsten is incorporated during bone growth and remodeling. This hypothesis is supported by the negligible tungsten uptake in older mice where bone remodeling due to growth is substantially reduced.[7] The similar heterogeneity of zinc provides further support (Figure 2.3.e,f).[6] Zinc is an excellent marker for bone growth and remodeling as it is known to deposit between zones of bone calcification.[6, 10] The heterogeneous accumulation of both tungsten and zinc at the inner and outer edges of the cortical bone tissue is likely connected to the changing width, and thus increased remodeling activity, of the long bone in these young, growing mice.
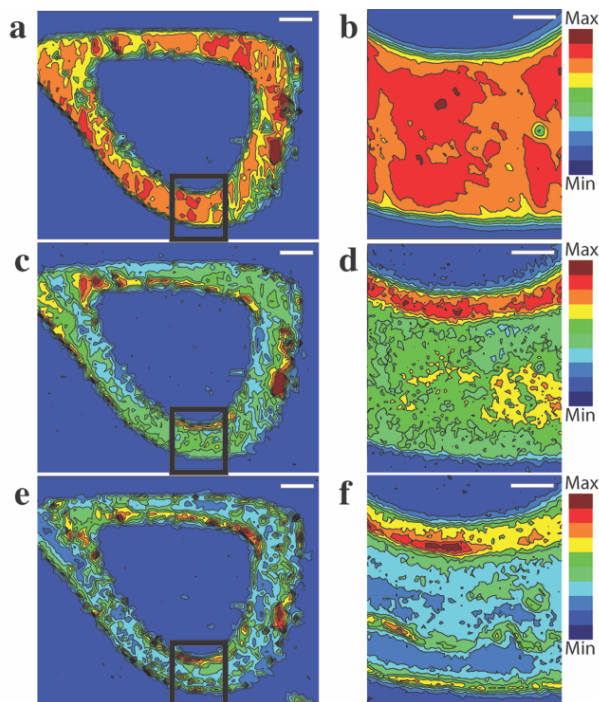
Figure 2.3. Comparative maps of Ca, W and Zn distribution in mouse tibia cross-section. SR-μXRF images collected simultaneously of mouse tibia after four weeks of exposure to tungsten (1000 ppm): (a,b) Ca, (c,d) W, (e,f) Zn. (a,c,e) Cross-sections of shaft with bone marrow removed from interior (20 μm step size). Scale bars 200 μm (b,d,f). Magnification of square indicated in (a,c,e) respectively (10 μm step size). Scale bars 50 μm. See Table S2.1. for intensity values.

2.4.2. Retention of Tungsten in Bone Tissue

Further retention experiments solidified the connection of tungsten uptake to bone remodeling. After an exposure regimen of 4 weeks of 1000 ppm tungsten (Na_2WO_4), followed by

8 weeks of tap water, tungsten deposition was mapped throughout mouse bone. Similar to the findings reported for the tibia above, tungsten was found throughout the outer cortical shell, inner cancellous tissue and bone marrow of the femur (Figure 2.4.a-c) after four weeks of exposure. However, after the source was removed, tungsten remained only in the outer cortical shell and was not detectable in the cancellous tissue or bone marrow (Figure 2.4.d-f). This is especially evident in the SR-μXRF overlay plots where tungsten (green) is present both in the calcium (red) containing cancellous bone tissue and in the bone marrow following four weeks of exposure (Figure 2.4.c), but no overlap is observed in this region when mice are given tungsten-free water for a further eight weeks (Figure 2.4.f). The same trend is evident within the bone shaft (Figure. 2.5.). The retention of tungsten only in cortical bone is consistent with remodeling activity in these tissues since cancellous bone has significantly higher rates of remodeling compared to cortical bone.[11] Thus, while cancellous bone quickly accumulates tungsten, it is also the first tissue to replace tungsten impregnated tissue with new bone once the source is removed. By contrast, retention is observed within cortical bone, which suggests that this tissue may act as a reservoir and a source of chronic tungsten exposure even after the original source is removed.
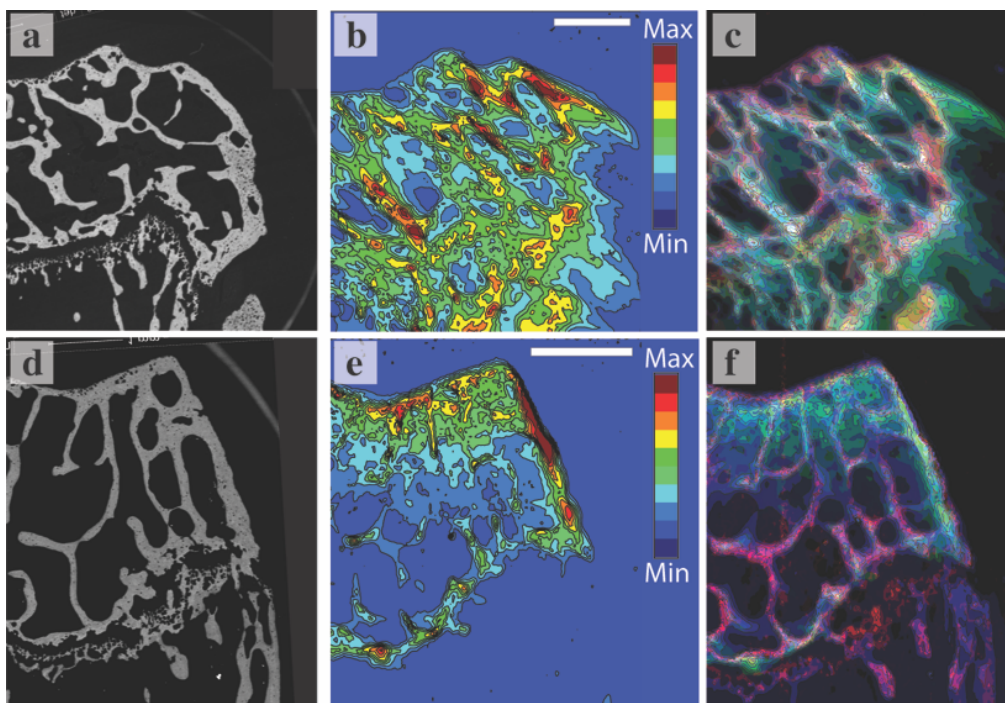
Figure 2.4. Tungsten retention in mouse femur head. (a-c) Femur head of mouse exposed to four weeks of tungsten (1000 ppm). (d-f) Femur head of mouse exposed to four weeks of tungsten (1000 ppm) followed by eight weeks of non-contaminated tap water. (a,d) BEI corresponding to SR-μXRF images. (b,e) Tungsten deposition map generated using SR-μXRF. Scale bars 500 μm. (c,f) Overlay images of calcium (red), tungsten (green), and zinc (blue) elements determined from SR-μXRF. See Table S2.1. for intensity values.
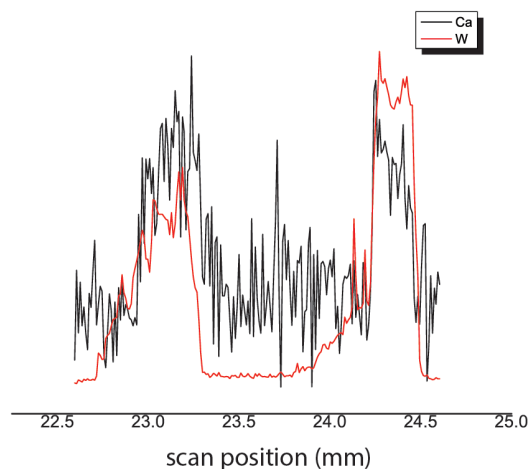
Figure 2.5. SR-μXRF linescan across femur shaft of mouse exposed to 4 weeks of tungsten followed by 8 weeks of tap water. Tungsten (red) is retained in cortical bone (indicated by higher calcium (black) intensities) but not in bone marrow. Images are taken at NSLS-II where the beamline is tuned to tungsten specific excitation resulting in a weaker calcium signal. X-axis is location on bone (mm) and y-axis is relative signal intensity. See Table S2.1. for values.

2.4.3. Chemical Speciation of Tungsten **in vivo**

The potential toxicity of tungsten within bone tissue is likely influenced by its chemical form therein. Indeed, speciation-specific toxicity in aquatic organisms has been reported for mono- and polytungstate species.[2] To identify the local coordination structure of tungsten within bone samples, eight SR-μXANES measurements were recorded across varying regions of cancellous and cortical tissues in tibia and femur samples (Figure 2.6.). The essentially identical spectra obtained (Figure 2.7.) are indicative of a remarkably consistent speciation profile and suggest that the chemical form of tungsten within this biological tissue is not influenced by environmental differences within bone physiology nor by the removal of the tungsten source following four weeks of exposure. The local concentration also does not appear to affect its speciation since spectra were recorded in areas displaying both high and low tungsten fluorescence intensity.
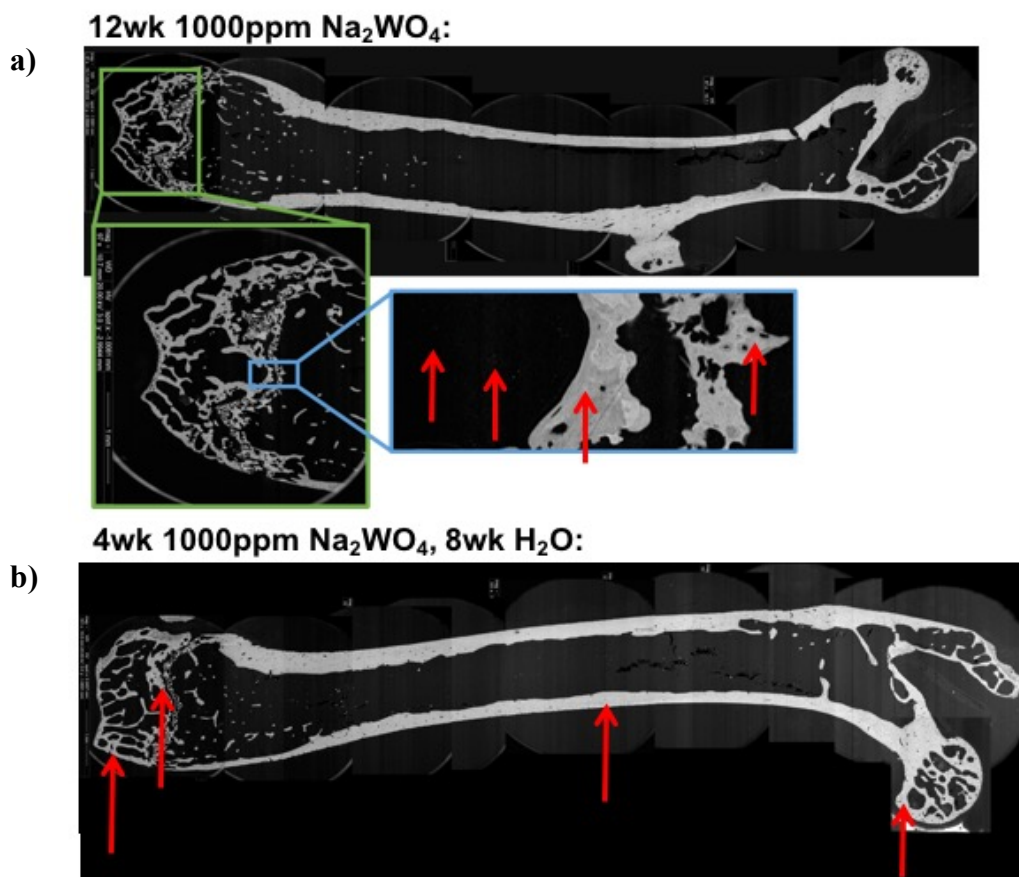
Figure 2.6. Location of XANES measurements in bone. (a) Femur of 12-week exposure to 1000ppm of tungsten; (b) Femur of 4-week 1000 ppm tungsten plus 8 weeks tap water.
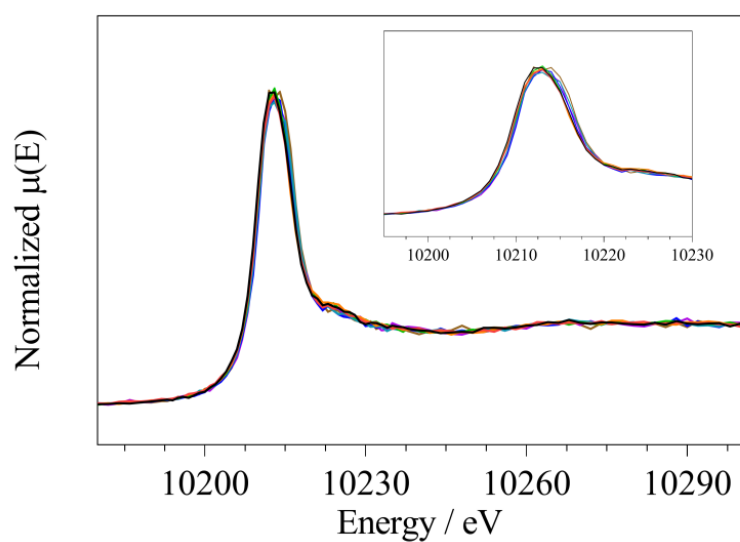
Figure 2.7. L_3 edge XANES spectra recorded for tungsten in bone samples at positions indicated by red arrows in Figure 2.6. Inset shows expansion of the pre- and post-edge region.
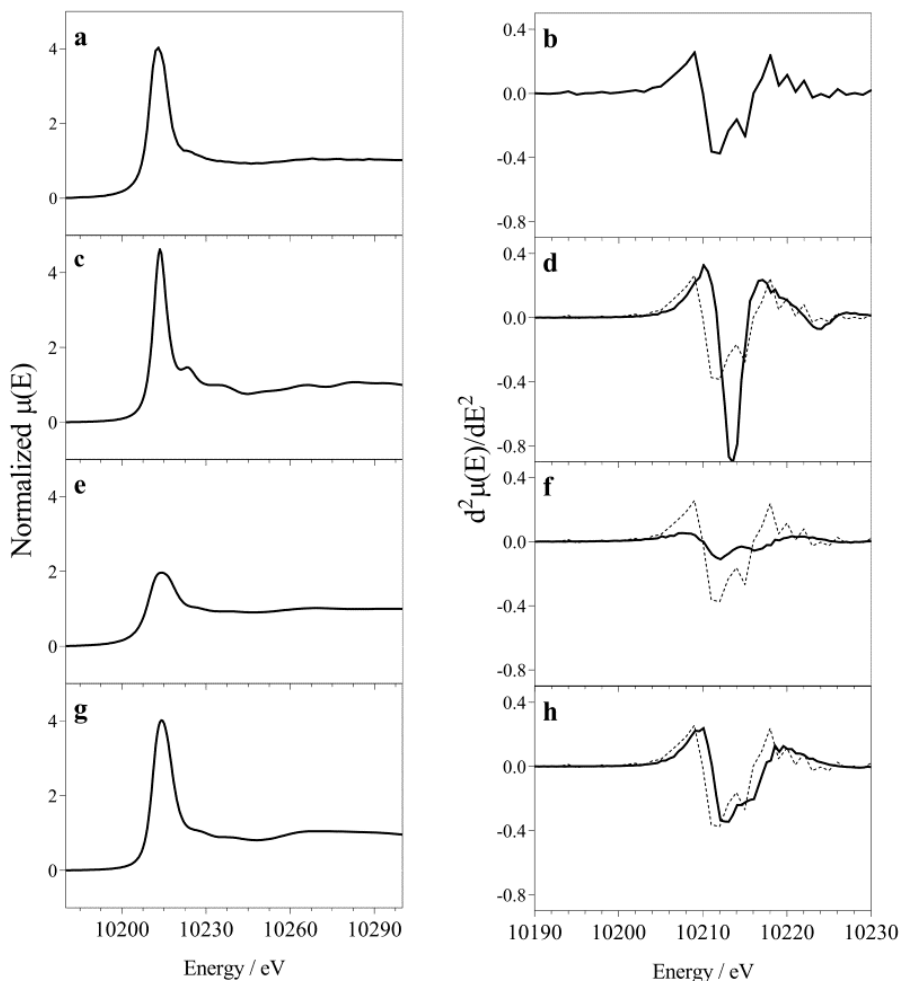
Figure 2.8. Averaged tungsten L_3-edge μ-XANES spectra (a,c,e,g) with their second derivatives (b,d,f,h) recorded for bone samples (a, b) and compared with XANES spectra of tungsten standards: sodium tungstate (c, d); ammonium paratungstate B (e, f); and phosphotungstate ($H_3PW_{12}O_{40}$) (g, h). To facilitated comparison, the spectrum in b is displayed as dashed lines in d, f and g.

There are, however, marked differences between the averaged XANES spectrum of tungsten in bone samples and that recorded for the form in which was administered, namely sodium tungstate (Figure 2.8.a vs c). This indicates that there is a change in tungsten speciation during uptake and/or deposition in bone tissue. A comparison of the second derivative of the XANES spectra more clearly highlights this difference (Figure 2.8.b vs d) but, more importantly, provides structural information regarding the coordination geometry around tungsten and can be used to identify a specific species.[12] The two closely spaced 2nd derivative minima observed for the bone sample at 10.211 and 10.215 keV are not consistent with a tetrahedral geometry which, as seen for sodium tungstate (Figure 2.8.d), produces a single sharp minimum. Instead, this feature is

indicative of a tungstate species that adopts a distorted octahedral geometry, similar to that observed in crystal structures of various polytungstates. The poor congruency between the spectra recorded for tungsten in bone samples and that of paratungstate B ($H_2W_{12}O_{42}^{10-}$), however, indicates condensation of ingested sodium tungstate into this polytungstate form does not occur (Figure 2.8.f). By contrast, close agreement is observed with the heteropolytungstate, phosphotungstate ($H_3PW_{12}O_{40}$, Figure 2.8.h). This molecule consists of twelve oxo-bridged tungsten atoms that surround and share ligation of a phosphate anion in what is referred to as a Keggin structure.[2] The similarity of the phosphotungstate XANES spectrum to that measured for tungsten in the bone samples suggests that the majority of tungsten present within bone tissue exists in a similar local coordination environment. The low pH conditions and high phosphate concentrations present during the bone remodeling processes could certainly favor the formation of phosphotungstate within bone tissue,[13] but the formation of additional tungstate species in minor quantities cannot be discounted. The low pH in gastric juice will favor polytungstate formation, but the ambient low concentrations of tungstate in the stomach is expected to limit polytungstate formation. This finding has important implications for tungsten toxicity since phosphotungstate is a well-established redox catalyst.[2, 14] It is also a new mechanism for the *in vivo* toxification of a soluble metal with the other recognized mechanism being metal methylation.[15]

2.5. Conclusion

In summary, we present the novel finding of site-specific, heterogeneous tungsten accumulation attaining levels ~ 10 fold greater than the background level. These levels are persistent, even once dietary exposure ceases. Furthermore, SR-μXANES studies indicate that tungsten in bone tissue is similar to the heteropolytungstate species phosphotungstate. This is alarming on a number of levels. Phosphotungstate is a known redox active catalyst and thus, if formed during bone remodeling, may have numerous deleterious biochemistries affecting essential bone functions, including growth, structure and immune cell formation. As ongoing studies continue to implicate tungsten in a variety of medical conditions, including promoting tumorigenesis, it is a concern that the World Health Organization has no water regulations for tungsten.[3, 4] The findings reported are essential for ongoing efforts to understand tungsten's effects on various biological processes and are crucial for the development of new, effective therapeutic methods for its mobilization and removal.

2.6 Supplemental Information

Figure		Element	Min Value	Max Value	Tungsten Exposure[ii]	Synchrotron	Sample Preparation
2.1.	c	W	3.15E-03	4.44E-02	A	CLS	Polished
	d	Ca	0	6.75E-03			
		W	0	5.03E-02			
		Zn	0	2.95E-02			
	e	Ca	0	7.33E-03			
		W	0	3.03E-02			
		Zn	0	2.15E-02			
2.2.	ai	W	5.00E-04	3.09E-02	C	CLS	Polished
	aii		0	2.33E-02			
	aiii		0	2.61E-02			
	bi		1.25E-04	3.06E-01	D	NSLS-II	Polished
	bii		7.50E-04	6.13E-02			
	biii		7.50E-04	4.83E-02			
2.3.	a	Ca	0	2.11E+00	A	CLS	10μm section
	b		3.50E-02	1.36E+00			
	c	W	9.85E-03	4.16E-02			
	d		1.05E-02	3.35E-02			
	e	Zn	3.45E-03	2.16E-02			
	f		3.85E-03	2.30E-02			
2.4.	b	W	1.75E-04	2.04E-02	A	CLS	Polished
	e		1.25E-04	5.99E-02	B	NSLS-II	Polished
2.5.		W	2.50E-04	9.33E-02	B	NSLS-II	Polished
		Ca	5.88E-03	3.46E-02			
S2.1.		W	9.85E-03	4.16E-02	A	CLS	10μm section
		Zn	3.45E-03	2.16E-02			
		Ca	0	2.11E+00			
		K	1.50E-04	1.53E-02			
		S	1.30E-04	3.13E-03			
		Ni	2.30E-03	3.34E-02			
		Cl	1.70E-04	2.05E-03			

[ii] A = 4wks, B= 4wks tungsten followed by 8 wks tap water, C = 1wk, D = 12wks.

Table S2.1. Maximum and minimum values used for XRF image scaling for bone samples obtained following exposure of mice to tungsten via 1000 ppm Na_2WO_4 dissolved in drinking water. Quantitative comparison between samples is not directly possible due to variations in illuminated volume (sample thickness) and beamline.
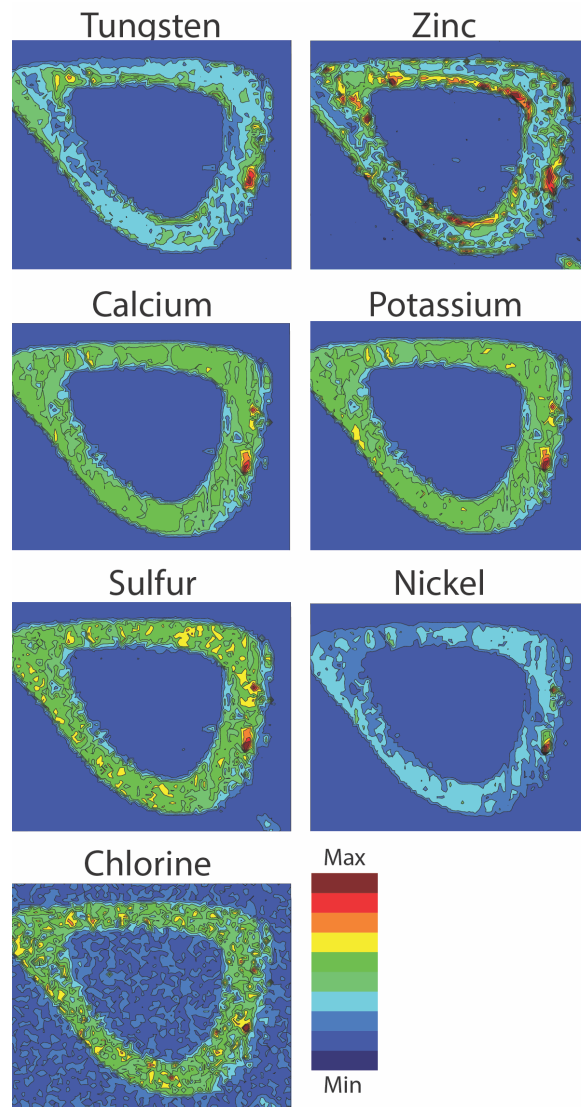
Figure S2.1. SR-μXRF images for detectable elements collected at CLS from tibia after 4 weeks of tungsten exposure. See Table S2.1. for intensity values.

2.7. References

1. *Molybdenum and Tungsten Enzymes*. Royal Society of Chemistry: Cambridge, 2016.

2. Strigul, N. Does Speciation Matter for Tungsten Ecotoxicology? *Ecotoxicology and Environmental Safety* **2010,** *73* (6), 1099-1113.

3. Bolt, A. M.; Sabourin, V.; Molina, M. F.; Police, A. M.; Negro Silva, L. F.; Plourde, D.; Lemaire, M.; Ursini-Siegel, J.; Mann, K. K. Tungsten Targets the Tumor Microenvironment to Enhance Breast Cancer Metastasis. *Toxicological Sciences* **2015,** *143*, 165-177.

4.   Lemus, R.; Venezia, C. F. An Update to the Toxicological Profile for Water-Soluble and Sparingly Soluble Tungsten Substances. *Critical reviews in toxicology* **2015,** *45* (5), 388-411.

5.   Guandalini, G. S.; Zhang, L.; Fornero, E.; Centeno, J. A.; Mokashi, V. P.; Ortiz, P. A.; Stockelman, M. D.; Osterburg, A. R.; Chapman, G. G. Tissue Distribution of Tungsten in Mice Following Oral Exposure to Sodium Tungstate. *Chemical Research in Toxicology* **2011,** *24* (4), 488-493.

6.   Pemmer, B. R., A.; Wastl, A.; Hofstaetter, J. G.; Wobrauschek, P.; Simon, R.; Thaler, H. W.; Roschger, P.; Klaushofer, K.; Streli, C. Spatial Distribution of the Trace Elements Zinc, Strontium and Lead in Human Bone Tissue. *Bone* **2013,** *57*, 184-193.

7.   Bolt, A. M.; Grant, M. P.; Wu, T. H.; Flores Molina, M.; Plourde, D.; Kelly, A. D. R.; Negro Silva, L. F.; Lemaire, M.; Schlezinger, J. J.; Mwale, F.; Mann, K. K. Tungsten Promotes Sex-Specific Adipogenesis in the Bone by Altering Differentiation of Bone Marrow-Resident Mesenchymal Stromal Cells. *Toxicological Sciences* **2016,** *150*, 333-346.

8.   Kelly, A. D. R.; Lemaire, M.; Young, Y. K.; Eustache, J. H.; Guilbert, C.; Molina, M. F.; Mann, K. K. In Vivo Tungsten Exposure Alters B-Cell Development and Increases DNA Damage in Murine Bone Marrow. *Toxicological Sciences* **2013,** *131*, 434-446.

9.   Harrop, T. C.; Song, D.; Lippard, S. J. Interaction of Nitric Oxide with Tetrathiolato Iron (Ii) Complexes : Relevance to the Reaction Pathways of Iron Nitrosyls in Sulfur-Rich Biological Coordination Environments. *Journal of the American Chemical Society* **2006,** *128* (11), 3528-3529.

10.   Gomez, S.; Rizzo, R.; Pozzi-Mucelli, M.; Bonucci, E.; Vittur, F. Zinc Mapping in Bone Tissues by Histochemistry and Synchrotron Radiation–Induced X-Ray Emission: Correlation with the Distribution of Alkaline Phosphatase. *Bone* **1999,** *25* (1), 33-38.

11.   Clarke, B. Normal Bone Anatomy and Physiology. *Clinical Journal of the American Society of Nephrology* **2008,** *3* (Supplement 3), S131.

12.   Hur, H.; Reeder, R. J. Tungstate Sorption Mechanisms on Boehmite: Systematic Uptake Studies and X-Ray Absorption Spectroscopy Analysis. *Journal of Colloid and Interface Science* **2016,** *461*, 249-260.

13.   Blair, H. C. How the Osteoclast Degrades Bone. *Bioessays* **1998,** *20*, 837-846.

14.   Hill, C. L., Polyoxometalates: Reactivity. In *Comprehensive Coordination Chemistry II*, McCleverty, J. A.; Meyer, T. J., Eds. Elsevier Inc.: San Diego, 2004; pp 679-759.

15.   Drobna, Z.; Styblo, M.; Thomas, D. J., An Overview of Arsenic Metabolism and Toxicity. In *Current Protocols in Toxicology*, John Wiley & Sons, Inc.: Hoboken, NJ, USA, 2009; pp 4.31.1-4.31.6.

Chapter 3. Addressing K/L-edge Overlap in Elemental Analysis from µXRF: Bioimaging of Tungsten and Zinc in Bone Tissue Using Synchrotron Radiation and LA-ICP-MS

3.1. Preface

In Chapter 2, we demonstrated that SR-µXRF can be used to map tungsten and zinc distribution in bone tissue *in situ*. However, the heterogeneity of the bone samples and overlap of the tungsten L-edge with the zinc K-edge signals complicates SR-µXRF data analysis, introduces minor artefacts into the resulting element maps, and decreases image sensitivity and resolution. In this chapter, we employ laser ablation inductively coupled plasma mass spectrometry (LA-ICP-MS) to untangle the problem created by the K/L-edge overlap of the tungsten/zinc pair and confirm the SR-µXRF results. This work was published in *Analytical and Bioanalytical Chemistry* (**2020**, *412*, 259-265). Data from Supplementary Information has been incorporated into the chapter.

3.2. Introduction

High-resolution elemental mapping is a powerful technique for visualizing metal distribution within biological tissue. SR-µXRF is a proven method for imaging elements in biological samples as it is (i) non-destructive; (ii) capable of sub-micrometer spatial resolution; and (iii) can detect multiple elements simultaneously.[1, 2] Furthermore, SR-µXRF can be paired with X-ray diffraction (XRD) or X-ray Absorption Spectroscopy (XAS) techniques, such as XANES spectroscopy, to inform *in situ* speciation/local structure.[3, 4] Due to these powerful abilities, SR-µXRF has been used to map elemental distribution in many biological applications, including bone tissue.[2, 5]

Tungsten is an emerging contaminant[6-9] that preferentially accumulates in bone.[10] Bone is a reservoir for many essential trace elements in the body, including zinc and iron, which are indispensable in maintaining normal physiological function.[11] Unfortunately, bone also acts as a long term accumulation site for heavy metals, such as lead, resulting in a chronic source of low-dose exposure and a variety of acute toxicities.[12] Our recent work on probing tungsten uptake in bone successfully used SR-µXRF in combination with µ-XANES to demonstrate that tungsten is heterogeneously deposited in a chemical form resembling phosphotungstate,[13] a known redox active catalyst.[14] Alarmingly, polyoxotungstates have been shown to be significantly more toxic

than monotungstate [WO_4^{2-}].[7] While research into the health implications of tungsten's presence in bone are ongoing, studies suggest that this metal may act as a tumor promoter by increasing DNA damage in bone marrow-resident B lymphocytes.[15] Preventing and treating accumulation of any toxic material in bone requires a fundamental understanding of its toxicokinetics, including mode of action and mechanism of uptake. Investigations into the specific distribution and speciation of tungsten in bone tissue are therefore essential for directing toxicological studies.

While we successfully used SR-μXRF to determine tungsten localization in bone, resolution was strongly affected by both the heterogenous sample and signal overlap between tungsten ($L\alpha_1 = 8.398$ keV) and zinc ($K\alpha_1 = 8.639$ keV) edges.[13] SR-μXRF is strongly dependent on sample preparation, including surface integrity and sample thickness.[2] The variable thickness and composition of bone samples leads to higher illuminated volumes, which can strongly effect image resolution and quantitative ability. Although X-ray spectroscopy is renowned for its spectacular ability to discriminate elements by their markedly different and unique K-edge energy bands, the energy of the K shell climbs out of the range of many X-ray spectrometers and beamlines for the heavier elements. As a consequence, heavy element L-edge spectroscopy is often employed with the resulting problem arising of overlap with lighter element K edges. Table 3.1. contains the element pairs affected by this overlap where the energy difference in the K/L pairs is shown in eV. In favorable cases where the K and L edges are separated by more than 0.5 keV, the spectra can be easily deconvoluted with singular value decomposition analysis as well as employing other bands of the L edge. This overlap requires careful mathematical fitting to assign localization to both elements but may still lead to decreasing resolution and sensitivity when imaging and/or analyzing.[2] Lastly, SR-μXRF is further limited by competitive access to synchrotron facilities.

Laser ablation inductively coupled plasma mass spectrometry (LA-ICP-MS) is an attractive, alternate visualization technique, which can overcome these difficulties as: i) elemental map resolution is not affected by inconsistencies in sample thickness ; ii) spectral interferences relate to mass, and low mass major and micro-elements generally do not interfere with higher mass trace elements, such as tungsten; iii) it has low limits of detection (0.1 μg/g); and iv) is comparatively faster and uses more readily available instrumentation than SR-μXRF.[1, 16] Consequently, LA-ICP-MS is well-suited for the investigation of elemental distribution in biological materials.[17-20] Spatial resolution, however, is limited by the laser system, with spot sizes

between 5 and 150 μm.[1] While quantitative analysis of metal concentrations in bone is possible,[21] it is strongly dependent on matrix-matched reference samples containing the metal of interest.

In this study, we compare and contrast SR-μXRF and LA-ICP-MS techniques for mapping tungsten and zinc distribution in bone tissue. Not only does LA-ICP-MS give better resolution due to the lack of any interferences on tungsten, but lower detection limits and the lack of sample thickness and heterogeneity considerations lead to higher image resolution, sensitivity and the visualization of key biological features not obvious when using SR-μXRF alone.

3.3 Experimental

3.3.1. Tungsten Exposure

Animal experiments were performed in the Lady Davis Institute Animal Care Facility following the guidelines of the McGill University Animal Care Committee approved protocol. Four-week-old male C57BL/6 J mice were purchased from Charles Rivers Laboratories Inc. (Montréal, Canada) or bred in house and were given food and water ad libitum. After 1 week of acclimation, mice were divided into three treatment groups of three mice each: control tap water, 15 or 1000 mg/L tungsten. Mice were exposed for four weeks. For tungsten exposures, the appropriate amount of sodium tungstate dihydrate ($Na_2WO_4 \cdot 2H_2O$; Sigma- Aldrich) was dissolved in tap water and was replaced every 2 or 3 days to limit conversion to polytungstates. Exposure groups were housed in different cages at the Lady Davis Institute animal facility. Daily water consumption between groups did not differ (+/- 0.16 ml/g).[15] Daily and total body tungsten exposure for 15 mg/L: 1.5 mg/kg and 42 mg/kg, respectively; for 1000 mg/L: 100 mg/kg and 2800 mg/kg, respectively. As we have previously published,[15] no changes in animal weight, physical appearance, or water intake were observed in the tungsten-exposed group. Though both 15 mg/L and 1000 mg/L are higher than background tungsten concentrations in environmental water measurements,[22] these concentrations were chosen in order to have significant accumulation in bone, which could be subsequently visualized with SR-μXRF and LA-ICP-MS techniques.

3.3.2. Preparation of Histological Samples

In order to probe elemental localization in relation to fine differences in the bone morphology, samples must possess a high integrity surface. Consequently, sample preparation is critical when measuring elemental distribution. In SR-μXRF, image resolution is additionally dependent on sample thickness due to the penetration depth of the X-rays.[2, 23] Bone is a particularly

challenging medium to prepare due to its hard, heterogeneous and brittle composition. Standard histology procedures for preparing thin bone sections often include a decalcification step to soften bone tissue before sectioning.[24] Decalcification, however, is undesirable for elemental mapping for two reasons: i) visualization of calcium is an essential reference element; and ii) decalcification may alter elemental distribution in the bone. Without the decalcification step, however, thin-sectioning results in a rough and uneven bone surface, which prevents correlation between element distribution and bone morphology (Figure 3.1.). To address this, we developed an adapted polishing method, as previously reported,[13] that delivers a higher integrity surface with a thickness profile of 100-250 μm.
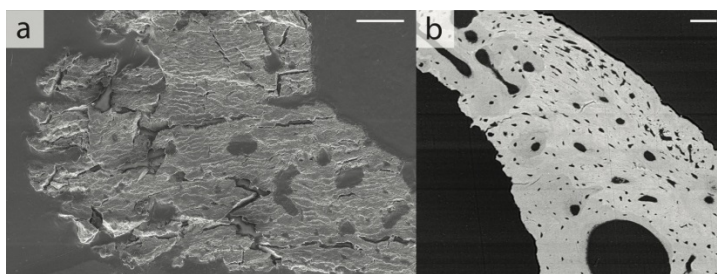
Figure 3.1. Backscattered electron image (BEI) of bone tibia cross-section, (a) prepared using thin-sectioning method and (b) via polishing method. Scale bar = 50 μm.

Following exposure regimen, sample thin-sections (100-250 μm) were prepared and imaged with backscattered electron imaging (BEI), using the fixation and polishing method previously reported.[13] BEI shows dense, calcium-containing cortical and cancellous bone but not lighter organic cartilage and bone marrow, providing a reference image of bone morphology.

3.3.3. Synchrotron Radiation Micro X-ray Fluorescence (SR-μXRF) Analysis

SR-μXRF measurements on the VESPERS beamline at the Canadian Light Source (CLS) were performed using parameters previously reported.[13] Data processing was based on same publication. XRF data was converted into HDF5 format using an in-house python script (https://github.com/davidkuter/XRF) and deconvoluted with the PyXRF software package (https://github.com/NSLS-II-HXN/PyXRF).[25] The data was normalized by incident beam count values and plotted in MatLab R2017b. The bottom and top 0.5% of the outlying intensity data was excluded using a histogram analysis.

3.3.4. LA-ICP-MS Analysis

Analysis of elemental distribution in bone was performed with LA-ICP-MS at the Dartmouth Trace Element Analysis Lab. LA was carried out with a NWR213 laser (Elemental Scientific Lasers, Bozeman, Montana). Elemental detection was performed with an Agilent 7900 ICP-MS (Santa Clara, CA) set to monitor S, Ca, Fe, Zn, W, Zn (at m/z 34, 43, 56, 66 and 182, respectively) in hydrogen mode. Sampling parameters included laser settings of 15 µm spot diameter, laser scan speed of 30 µm/sec firing at 20 Hz and laser power set at 50% equating to a fluence of 12.9 J/cm^2. Data were collected as time resolved intensity of S, Ca, Fe, Zn, W, Zn with a sampling period of 0.5 seconds so that each data pass of the ICP-MS corresponded to 15 µm on the sample. A 15 µm spot size was chosen as it provided ample resolution for elemental imaging in bone. LA-ICP-MS data was plotted using MatLab (https://github.com/davidkuter/ICP-MS). A histogram analysis was performed on the intensity data to determine upper and lower limits of LA-ICP-MS plots. These values were selected such as to exclude the bottom and top 0.5% of the outlying data.

3.4. Results and Discussion

Figure 3.2. compares the elemental maps obtained using SR-µXRF and LA-ICP-MS on the same section of the proximal tibia of a mouse exposed to 1000 ppm of tungsten. BEI images (Figure 3.2.a,e) and calcium elemental maps (Figure 3.2.b,i) provide a reference indicating the location of calcified tissue. Both SR-µXRF and LA-ICP-MS demonstrate a heterogenous distribution of tungsten (Figure 3.2.c,j) and zinc (Figure 3.2.d,k), comparable to the distribution previously reported using SR-µXRF.[13] The consistency of the results for both techniques validates the use of LA-ICP-MS as a suitable alternative to SR-µXRF for determining elemental distribution in bone.
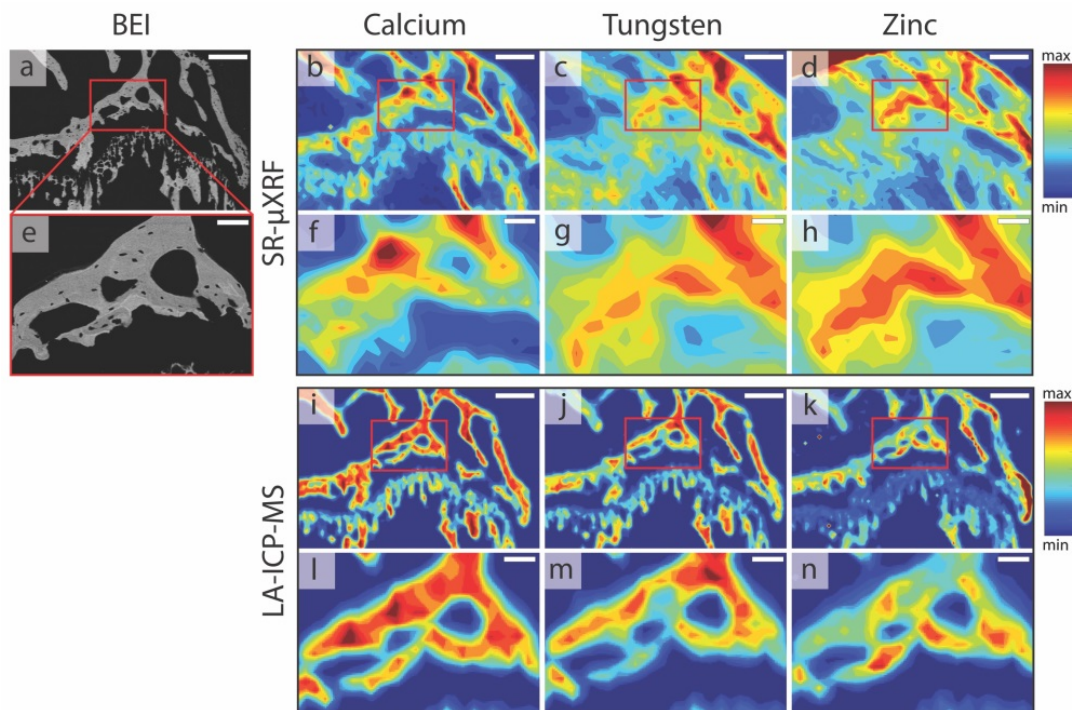
Figure 3.2. SR-μXRF (b-d, f-h; 20 μm step size) and LA-ICP-MS (i-n; 15 μm step size) elemental distribution maps of an identical longitudinally sliced murine proximal tibia sample from a mouse exposed for 4 weeks to 1000 ppm tungsten in drinking water. Calcium, tungsten, and zinc distribution maps are pictured in the left, center and right columns respectively. BEI image (a,e) for comparison. Magnified sections (e-h, l-n; scale bar = 50 μm) of each map indicated by red boxes in (a-e, i-k, scale bar = 200 μm) respectively. Intensity values are given in Table S3.1. Exact image registration between the two techniques stems from distinctive bone tissue ultrastructure and the BEI images a and e.

3.4.1. Improvements in Image Resolution

The most significant difference between the maps generated by these two techniques is the vast improvement in image resolution for LA-ICP-MS (approximately ten-fold) despite the similar spatial resolution used for SR-μXRF and LA-ICP-MS (20 μm vs 15 μm spot-size, respectively). Image resolution improvement factor (IRIF) is calculated by dividing the smallest distinguishable features in SR-μXRF by that of LA-ICP-MS as shown in Equation 3.1. X and Y variables for Equation 3.1. are demonstrated in Figure 3.3. Herein, we define image resolution as the detail the image holds and extent to which individual features can be distinguished from each other. Even at higher magnification (approximately four-fold), LA-ICP-MS maps (Figure 3.2.l-n) remain clear and individual features, including differences in elemental distribution, can be clearly correlated with the surface morphology shown in BEI images. Magnified SR-μXRF maps (Figure 3.2.f-h),

however, lose definition to such an extent that meaningful comparison with the BEI image is impossible.

$$\text{IRIF} = \frac{\text{Minimum distiguishable feature SR}-\mu\text{XRF }(\mu m)}{\text{Minimum distiguishable feature LA}-\text{ICP}-\text{MS }(\mu m)} = \frac{X}{Y} \; \frac{70.8 \;\mu m}{7.6 \;\mu m} = 9.3 \qquad \textbf{Equation 3.1}.$$
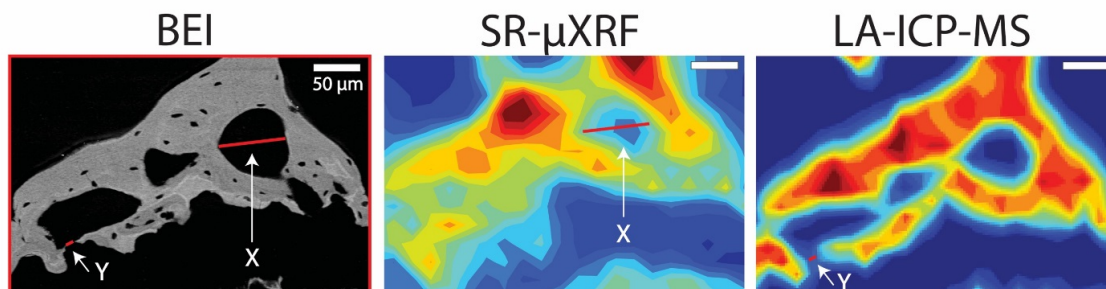
Figure 3.3. X and Y coordinates for Equation 3.1. From left to right: BEI, SR-µXRF and LA-ICP-MS calcium distribution maps of the identical longitudinally sliced murine proximal tibia sample. These images are the same magnified sections as indicated in Figure 3.2.
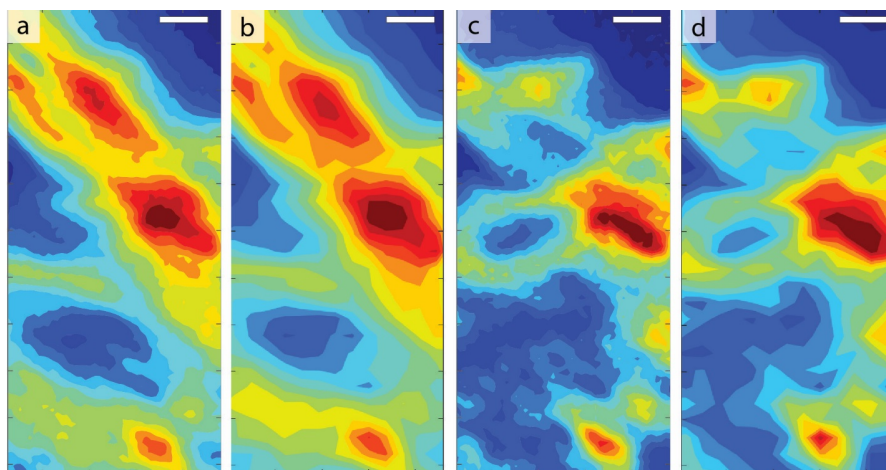
Figure 3.4. Comparison of SR-µXRF resolution at two different step sizes. Tungsten (a-b) and (calcium c-d) SR-µXRF maps of longitudinally sliced murine femoral knee section. Maps (a,c) are collected at a higher resolution of 5 µm step size compared to the lower resolution maps (b,d) which have a 18 µm step size. Scale bar = 50 µm. Intensity values in Table S3.1.

While SR-µXRF techniques are capable of achieving higher spatial resolution than LA-ICP-MS, theoretically leading to better image resolution, this is strongly dependent on the sample.[1] For bone samples, using smaller spot sizes did not significantly improve the image resolution of the elemental maps (Figure 3.4.), which can be explained by two factors. The first is inconsistencies in the X-ray illuminated volume arising from the inherent heterogeneity of bone tissue and the thick, non-uniform sample produced by polishing in the necessary preparatory process.[23] Though polished bone samples provide the high integrity surface essential for high resolution imaging, this preparation technique results in thicker samples. Increasing sample

thickness results in a larger illuminated volume as seen in Figure 3.5. A larger illuminated volume for a heterogeneous sample such as bone can significantly decrease resolution as the sample changes within the sampled area. Conversely, inconsistent thickness does not affect LA-ICP-MS resolution as this method uses a flat-top ablation profile which gives an ablation pit with a uniform thickness of less than 10 μm - much less than the sample thickness. Image resolution is dependent on surface flatness and integrity, not sample depth or heterogeneity.
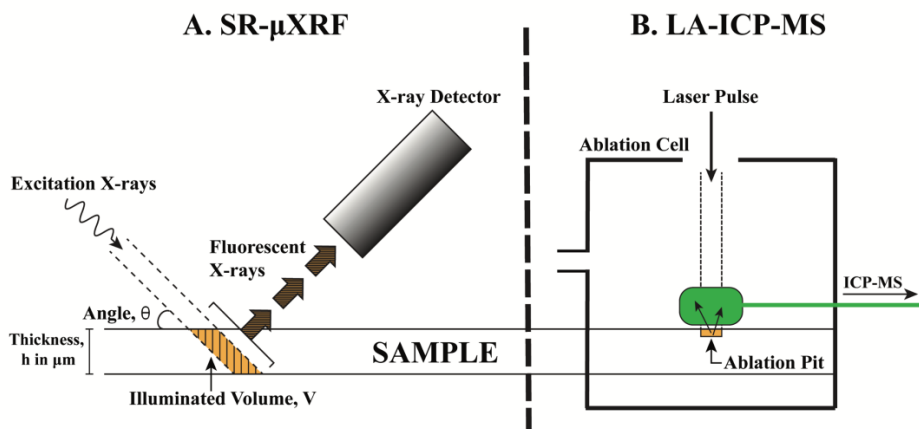
Figure 3.5. Setup of SR- μXRF versus LA-ICP-MS. In (a), the typical SR- μXRF detector/source geometry of θ = 45° with respect to sample is shown. The beam size and sample thickness both contribute to the large illuminated volume that contributes to the loss of resolution in SR-μXRF. The two volume cell setup that was used for LA-ICP-MS is displayed in (b).

3.4.2. Addressing Imperfect SR-μXRF Deconvolution

Secondly, differences in attainable image resolution between LA-ICP-MS and SR-μXRF also arise from differences in signal collection and processing for each technique. In LA-ICP-MS, counts from each detected element are separated based on their mass-charge ratio and collected independently.[20] Spectral interference, therefore, is caused by identical mass-charge ratios of the analyte of interest and the interferent. In SR-μXRF, by contrast, signal is generated by the fluorescence excitation of every element present, resulting in several characteristic X-ray fluorescence lines that need to be deconvoluted using fitting software to obtain individual element maps.[2] While elemental emission lines are unique, they can overlap with other elements because of limitations in the energy resolution of the detector and, even with deconvolution, can cause cross-interferences between individual elemental maps (Table 3.1.). This is certainly the case for the principal α_1 lines for the tungsten L-edge and zinc K-edges at 8.398 and 8.639 keV

respectively.[2] The systematic errors introduced by the complicated deconvolution analysis contribute to the reduced image resolution.

Element Kα₁ Edge (Z)	Δ Edge Less than 0.1 keV		Δ Edge Less than 0.25 keV	
	L Edge Element (Z)	ΔkeV	L Edge Element (Z)	ΔkeV
K (19)	-	-	Sn (50)	0.13
Ca (20)	Sb (51)	0.088	Sn (50)	0.248
Ca (20)	Te (52)	0.076	I (53)	0.246
Sc (21)	Xe (54)	0.017	I (53)	0.155
Sc (21)	-	-	Cs (55)	0.192
Ti (22)	Ba (56)	0.046	La (57)	0.135
V (23)	Pr (59)	0.082	Ce (58)	0.114
Cr (24)	Pm (61)	0.017	Nd (60)	0.187
Mn (25)	Eu (63)	0.051	Gd (64)	0.153
Fe (26)	Dy (65)	0.093	Tb (65)	0.132
Co (27)	Er (68)	0.018	Ho (67)	0.211
Ni (28)	Yb (70)	0.064	Lu (71)	0.175
Cu (29)	Ta (73)	0.1	Hf (72)	0.147
Zn (30)	Re (75)	0.015	W (74)	0.239
Ga (31)	Ir (77)	0.076	Pt (78)	0.191
Ge (32)	Hg (80)	0.103	Au (79)	0.173
As (33)	Pb (82)	0.008	Tl (81)	0.074
Se (34)	Po (84)	0.093	At (85)	0.203
Br (35)	Fr (87)	0.107	Rn (86)	0.197
Kr (36)	Ac (89)	0.004	-	-
Rb (37)	Pa (91)	0.105	U (92)	0.218
Sr (37)	Pu (94)	0.117	Np (93)	-0.219

Table 3.1. Close Kα₁ /Lα₁ Edge overlaps distinguished by differences in edge energies in keV. Energies taken from the ALS X-ray Data Booklet.[26] Particularly close overlapping pairs such as As/Pb and Ca/Sn have been discussed before.[2]

An additional consequence of the zinc/tungsten overlap in SR-µXRF measurements is demonstrated in Figure 3.6. Deconvolution works reasonably well for samples with high tungsten accumulation, where differences in tungsten and zinc accumulation are clearly visible in the femoral head of a mouse exposed to 1000 ppm tungsten (Figure 3.6.a, b). However, in control samples where mice are not exposed to tungsten, a moderate tungsten signal is still calculated in elemental maps generated using SR-µXRF (Figure 3.6.c). The lack of a tungsten signal in the LA-ICP-MS image (Figure 3.6.g), on the other hand, indicates that the low tungsten levels calculated

by SR-μXRF is an artefact. Given the SR-μXRF tungsten signal's close resemblance to the corresponding zinc map (Figure 3.6.d), this "phantom" tungsten signal likely arises from residual zinc signal owing to imperfect spectral deconvolution.
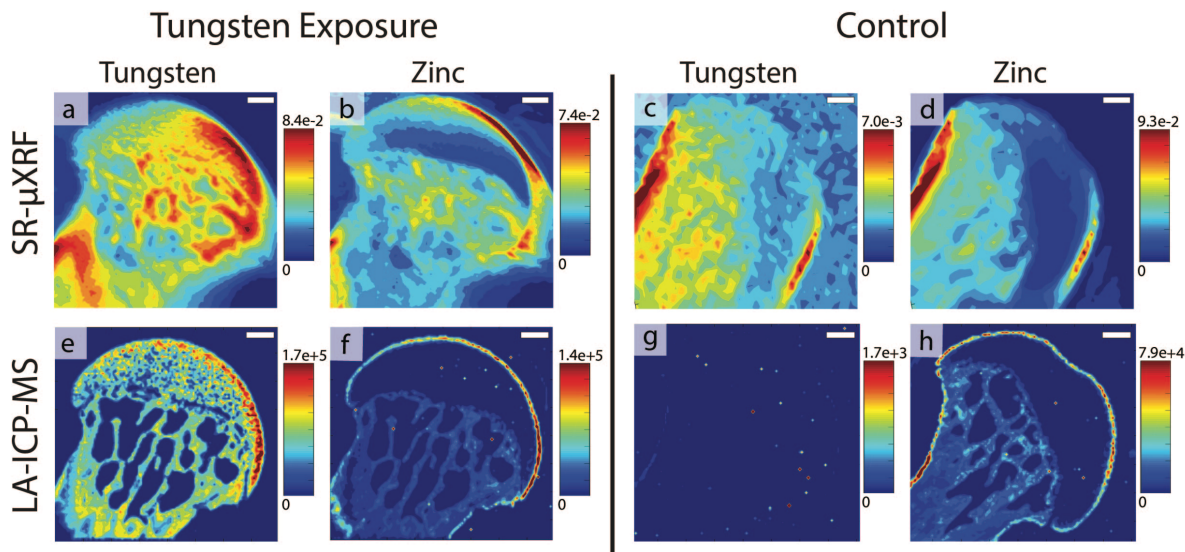
Figure 3.6. Comparison of elemental maps from control and tungsten exposed mouse. (a-d) SR-μXRF and (e-h) LA-ICP-MS tungsten and zinc distribution maps of longitudinally sliced murine femoral head from a mouse exposed to (a,b,e,f) 1000 ppm of tungsten and (c,d,g,h) tap water as a control for four weeks. Intensity scale is in normalized counts for SR-μXRF and counts for LA-ICP-MS and cannot be compared between the two techniques. Step size: (a,b) 16 μm; (c,d) 41 μm; (e-h) 15 μm. Scale bars = 200 μm

Though deconvolution does not attain perfect separation of the tungsten and zinc signals, the amount of signal that zinc adds to tungsten is negligible at high tungsten concentrations. There is approximately a ten-fold difference between the maximum tungsten intensity in the control and high tungsten sample (Figure 3.6.a,c), indicating the degree to which zinc may contribute to the observed tungsten signal. Furthermore, when the upper limit of the tungsten control is used as the lower limit in the high tungsten map, there is no significant difference in tungsten distribution (Figure 3.7.). Thus, when comparing areas of the bone with similar tungsten and zinc distribution patterns, such as the cortical bone,[13] we can conclude that these similarities are genuine for samples exposed to high concentrations of tungsten. This is further validated by comparison with LA-ICP-MS, where we see a similar distribution trend for tungsten and zinc (Figure 3.8.). However, for samples exposed to lower tungsten concentrations, it would not be possible to use SR-μXRF since the zinc interference becomes more pronounced and its contribution to the overall signal cannot be ignored. LA-ICP-MS, on the other hand, has the substantial advantage that heavy elements (requiring analysis by L lines in SR-XRF) are generally not affected by any instrumental

interferences in ICP-MS which simplifies data processing and removes any uncertainty about validity of the observed signals during data analysis.
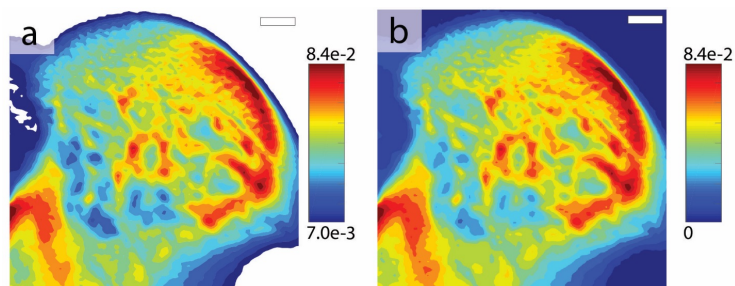
Figure 3.7. SR-µXRF tungsten elemental distribution map with background removed. Image (b) corresponds to Figure 3.6.a of longitudinally sliced murine femoral head from mouse exposed to 1000 ppm of tungsten with lower limit = 0. In (a) the same map as (b) but with the lower limit corresponding to upper limit from control sample, Figure 3C. White background indicates counts below the lower limit. 16 µm step size. Scale bars = 200 µm.
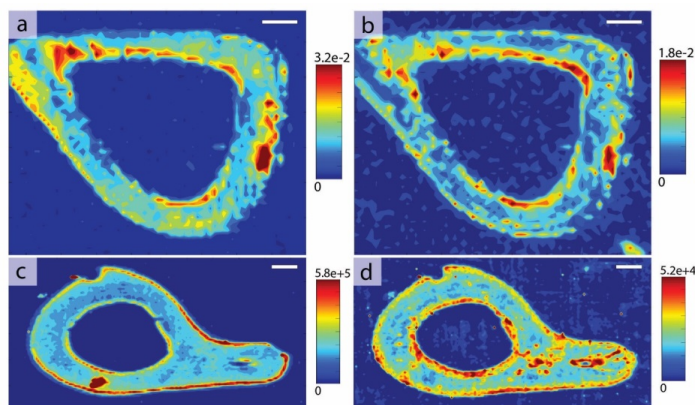
Figure 3.8. Similar distribution trends for tungsten and zinc in cortical bone. (a-b) SR-µXRF[13] and (c-d) LA-ICP-MS maps of murine tibia and femur cross-sections, respectively, from mouse exposed to 1000 ppm of tungsten for four weeks. Similar tungsten (a,c) and zinc (b,d) distribution trends are observed. Intensity scale is in normalized counts for SR-µXRF and counts for LA-ICP-MS and cannot be compared between the two techniques. Step size: (a,b) 20 µm; (c,d) 15 µm. Scale bars = 200 µm.

3.4.3. Improved Sensitivity

Finally, LA-ICP-MS has the significant advantage, compared to SR-µXRF, of higher sensitivity to trace elemental concentrations.[27] This is especially the case for heavy elements, such as tungsten which have high ion transmission through the mass spectrometer, when contrasting the signal from the less sensitive L-line in SR-µXRF to that of primary isotope detected using LA-ICP-MS. Several studies have utilized the high sensitivity capabilities of LA-ICP-MS to supplement XRF studies of heterogeneous samples.[27-29] While visualization of tungsten

distribution in bone tissue was readily accomplished using both SR-µXRF and LA-ICP-MS methods when mice were exposed to 1000 ppm in water, this exposure regime greatly exceeds normal environmental contamination levels.[30, 31] Even at a significantly lower exposure regimen of 15 ppm, a notable tungsten accumulation is still observed using LA-ICP-MS (Figure 3.9.). Furthermore, tungsten distribution is similar at both low and high concentrations, indicating that anatomical accumulation sites are not dependent upon exposure concentration. By contrast, no significant tungsten signal beyond the limit of W/Zn deconvolution was detected across numerous line-scans using SR-µXRF at the low tungsten regime (consequently a full SR-µXRF map was not collected). The increased sensitivity, along with a higher sampling speed, for LA-ICP-MS over SR-µXRF is thus a considerable advantage when looking at biological samples which often contain only trace levels of many elements. The ability to probe trace element distribution across bone is significant, as bone is the reservoir for many elements in the body.[11]
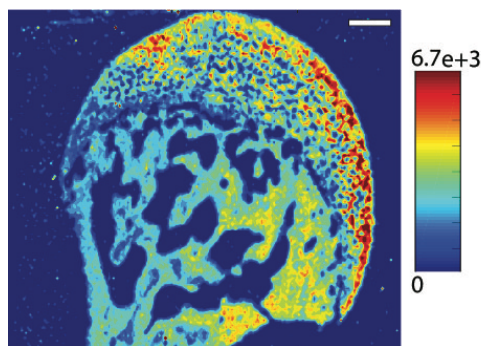
Figure 3.9. LA-ICP-MS tungsten distribution map at low concentration. Longitudinally sliced murine femoral head from mouse exposed to 15 ppm tungsten in drinking water for four weeks. 15µm step size. Intensity scale in counts. Scale bars = 200 µm

3.5. Conclusion

Although SR-µXRF is a powerful elemental mapping technique, K/L edge overlap for many element combinations can complicate the image analysis and interpretation. In this case the unexpected convergence of zinc and tungsten biochemistry in bone reformation was discovered and revealed by SR-µXRF. However, the overlap of the tungsten L-edge with zinc K-edge signals along with the heterogeneity and thickness of the bones samples negatively impact the image resolution and sensitivity when determining tungsten and zinc localization in bone using SR-µXRF. This study finds that LA-ICP-MS is a reliable alternative method for the visualization of

these metals in bone tissue and largely confirms SR-μXRF findings of heterogeneous tungsten accumulation. Furthermore, LA-ICP-MS provides higher image resolution while being significantly more sensitive to lower concentrations of trace elements. These qualities, along with the ability to analyze multiple samples in a relatively short time frame, is important when investigating inherently heterogeneous biological samples. Lastly, LA-ICP-MS also has the ability to quantitatively determine metal concentration in bone, as has been demonstrated with lead.[21] To realize this possibility with tungsten bone deposits, the development of suitable matrix-matched reference samples is currently underway. It is noteworthy to mention that, although LA-ICP-MS provides superior imaging capability for elemental distribution in bone, SR-μXRF remains attractive as a complementary technique due to its non-destructive nature and capability of being paired with XRD and XAS techniques to determine speciation *in situ*.

3.6. Supplemental information

Figure		Technique	Element	Minimum Intensity	Maximum Intensity
3.2.	c,f	SR-μXRF	Calcium	0	4.70E-02
	d,g		Tungsten	0	4.00E-02
	e,h		Zinc	0	7.30E-03
	i,l	LA-ICP-MS	Calcium	0	3.16E+05
	j,m		Tungsten	0	1.79E+05
	k,n		Zinc	0	8.37E+04
3.4.	a	SR-μXRF	Tungsten	0	5.35E-02
	b		Tungsten	0	2.00E-02
	c		Calcium	0	1.04E-02
	d		Calcium	0	3.73E-03

Table S3.1. Maximum intensity values used for scaling SR-μXRF and LA-ICP-MS maps (Figure 3.2. and Figure 3.4.). Intensity scale is in normalized counts for SR-μXRF and counts for LA-ICP-MS and cannot be compared between the two techniques.

3.7. References

1.   Ackerman, C. M.; Lee, S.; Chang, C. J. Analytical Methods for Imaging Metals in Biology: From Transition Metal Metabolism to Transition Metal Signaling. *Analytical Chemistry* **2017,** *89*, 22-41.

2.   Pushie, M. J.; Pickering, I. J.; Korbas, M.; Hackett, M. J.; George, G. N. Elemental and Chemically Specific X-Ray Fluorescence Imaging of Biological Systems. *Chemical Reviews* **2014,** *114*, 8499-8541.

3.   Meirer, F.; Pemmer, B.; Pepponi, G.; Zoeger, N.; Wobrauschek, P.; Sprio, S.; Tampieri, A.; Goettlicher, J.; Steininger, R.; Mangold, S.; Roschger, P.; Berzlanovich, A.; Hofstaetter, J. G.; Streli, C. Assessment of Chemical Species of Lead Accumulated in Tidemarks of Human Articular Cartilage by X-Ray Absorption near-Edge Structure Analysis. *Journal of synchrotron radiation* **2011,** *18*, 238-244.

4.   Barrea, R. A.; Antipova, O.; Gore, D.; Heurich, R.; Vukonich, M.; Kujala, N. G.; Irving, T. C.; Orgel, J. P. R. O. X-Ray Micro-Diffraction Studies on Biological Samples at the Biocat Beamline 18-Id at the Advanced Photon Source. *Journal of synchrotron radiation* **2014,** *21* (Pt 5), 1200-1205.

5.   Pemmer, B.; Roschger, A.; Wastl, A.; Hofstaetter, J. G.; Wobrauschek, P.; Simon, R.; Thaler, H. W.; Roschger, P.; Klaushofer, K.; Streli, C. Spatial Distribution of the Trace Elements Zinc, Strontium and Lead in Human Bone Tissue. *Bone* **2013,** *57*, 184-193.

6.   Koutsospyros, A.; Braida, W.; Christodoulatos, C.; Dermatas, D.; Strigul, N. A Review of Tungsten: From Environmental Obscurity to Scrutiny. *J Hazard Mater* **2006,** *136* (1), 1-19.

7.   Strigul, N. Does Speciation Matter for Tungsten Ecotoxicology? *Ecotoxicology and Environmental Safety* **2010,** *73*, 1099-1113.

8.   Bolt, A. M.; Sabourin, V.; Molina, M. F.; Police, A. M.; Negro Silva, L. F.; Plourde, D.; Lemaire, M.; Ursini-Siegel, J.; Mann, K. K. Tungsten Targets the Tumor Microenvironment to Enhance Breast Cancer Metastasis. *Toxicological Sciences* **2015,** *143*, 165-177.

9.   Lemus, R.; Venezia, C. F. An Update to the Toxicological Profile for Water-Soluble and Sparingly Soluble Tungsten Substances. *Critical Reviews in Toxicology* **2015,** *45*, 388-411.

10.   Guandalini, G. S.; Zhang, L.; Fornero, E.; Centeno, J. A.; Mokashi, V. P.; Ortiz, P. A.; Stockelman, M. D.; Osterburg, A. R.; Chapman, G. G. Tissue Distribution of Tungsten in Mice Following Oral Exposure to Sodium Tungstate. *Chemical Research in Toxicology* **2011,** *24*, 488-493.

11.   Aaseth, J.; Boivin, G.; Andersen, O. Osteoporosis and Trace Elements – an Overview. *Journal of Trace Elements in Medicine and Biology* **2012,** *26* (2), 149-152.

12.   Pounds, J. G.; Long, G. J.; Rosen, J. F. Cellular and Molecular Toxicity of Lead in Bone. *Environmental health perspectives* **1991,** *91*, 17-32.

13.   VanderSchee, C. R.; Kuter, D.; Bolt, A. M.; Lo, F.-C.; Feng, R.; Thieme, J.; Chen-Wiegart, Y. K.; Williams, G.; Mann, K. K.; Bohle, D. S. Accumulation of Persistent

Tungsten in Bone as in Situ Generated Polytungstate. *Communications Chemistry* **2018,** *1*, 8.

14. Wang, S.-S.; Yang, G.-Y. Recent Advances in Polyoxometalate-Catalyzed Reactions. *Chemical Reviews* **2015,** *115* (11), 4893-4962.

15. Kelly, A. D. R.; Lemaire, M.; Young, Y. K.; Eustache, J. H.; Guilbert, C.; Molina, M. F.; Mann, K. K. In Vivo Tungsten Exposure Alters B-Cell Development and Increases DNA Damage in Murine Bone Marrow. *Toxicological Sciences* **2013,** *131*, 434-446.

16. Diwakar, P. K.; Gonzalez, J. J.; Harilal, S. S.; Russo, R. E.; Hassanein, A. Ultrafast Laser Ablation Icp-Ms: Role of Spot Size, Laser Fluence, and Repetition Rate in Signal Intensity and Elemental Fractionation. *Journal of Analytical Atomic Spectrometry* **2014,** *29* (2), 339-346.

17. Austin, C.; Smith, T. M.; Bradman, A.; Hinde, K.; Joannes-Boyau, R.; Bishop, D.; Hare, D. J.; Doble, P.; Eskenazi, B.; Arora, M. Barium Distributions in Teeth Reveal Early-Life Dietary Transitions in Primates. *Nature* **2013,** *498*, 216-219.

18. Trog, S.; El-Khatib, A. H.; Beck, S.; Makowski, M. R.; Jakubowski, N.; Linscheid, M. W. Complementarity of Molecular and Elemental Mass Spectrometric Imaging of Gadovist™ in Mouse Tissue. *Analytical and Bioanalytical Chemistry* **2019,** *411* (3), 629–637.

19. Halbach, K.; Wagner, S.; Scholz, S.; Luckenbach, T.; Reemtsma, T. Elemental Imaging (La-Icp-Ms) of Zebrafish Embryos to Study the Toxicokinetics of the Acetylcholinesterase Inhibitor Naled. *Analytical and Bioanalytical Chemistry* **2019,** *411* (3), 617-627.

20. Sussulini, A.; Becker, J. S.; Becker, J. S. Laser Ablation Icp-Ms: Application in Biomedical Research. *Mass Spectrometry Reviews* **2017,** *36* (1), 47-57.

21. Bellis, D. J.; Hetter, K. M.; Jones, J.; Amarasiriwardena, D.; Parsons, P. J. Calibration of Laser Ablation Inductively Coupled Plasma Mass Spectrometry for Quantitative Measurements of Lead in Bone. *Journal of Analytical Atomic Spectrometry* **2006,** *21*, 948-954.

22. ATSDR, Toxicological Profile for Tungsten. U.S. Department of Health and Human Services, P. H. S., Ed. Atlanta, GA, 2015; pp 11-12.

23. Szczerbowska-Boruchowska, M. Sample Thickness Considerations for Quantitative X-Ray Fluorescence Analysis of the Soft and Skeletal Tissues of the Human Body – Theoretical Evaluation and Experimental Validation. *X-ray Spectrometry* **2012,** *41* (5), 328-337.

24. Skinner, R. A., Decalcification of Bone Tissue. In *Handbook of Histology Methods for Bone and Cartilage*, An, Y. H.; Martin, K. L., Eds. Humana Press: Totowa, NJ, 2003; pp 167-184.

25.   Li, L.; Yan, H.; Xu, W.; Yu, D.; Heroux, A.; Lee, W.-K.; Campbell, S. I.; Chu, Y. S. In *Pyxrf: Python-Based X-Ray Fluorescence Analysis Package*, SPIE Optical Engineering + Applications, SPIE: 2017; p 8.

26.   Thompson, A. C., *Center for X-Ray Optics and Advanced Light Source X-Ray Data Booklet*. Third Edition ed.; Lawrence Berkeley National Laboratory: Berkeley, California, 2009.

27.   Blaske, F.; Reifschneider, O.; Gosheger, G.; Wehe, C. A.; Sperling, M.; Karst, U.; Hauschild, G.; Höll, S. Elemental Bioimaging of Nanosilver-Coated Prostheses Using X-Ray Fluorescence Spectroscopy and Laser Ablation-Inductively Coupled Plasma-Mass Spectrometry. *Analytical Chemistry* **2014,** *86*, 615-620.

28.   Wang, H. A. O.; Grolimund, D.; Loon, L. R. V.; Barmettler, K.; Borca, C. N.; Aeschlimann, B. Quantitative Chemical Imaging of Element Diffusion into Heterogeneous Media Using Laser Ablation Inductively Coupled Plasma Mass Spectrometry, Synchrotron Micro-X-Ray Fluorescence, and Extended X-Ray Absorption Fine Structure Spectroscopy. *Analytical Chemistry* **2011,** *83*, 6259-6266.

29.   Davies, K. M.; Hare, D. J.; Bohic, S.; James, S. A.; Billings, J. L.; Finkelstein, D. I.; Doble, P. A.; Double, K. L. Comparative Study of Metal Quantification in Neurological Tissue Using Laser Ablation-Inductively Coupled Plasma-Mass Spectrometry Imaging and X-Ray Fluorescence Microscopy. *Analytical Chemistry* **2015,** *87*, 6639-6645.

30.   Koutsospyros, A.; Braida, W.; Christodoulatos, C.; Dermatas, D.; Strigul, N. A Review of Tungsten: From Environmental Obscurity to Scrutiny. *Journal of Hazardous Materials* **2006,** *136*, 1-19.

31.   Marquet, P.; François, B.; Vignon, P.; Lachâtre, G. A Soldier Who Had Seizures after Drinking Quarter of a Litre of Wine. *The Lancet* **1996,** *348* (9034), 1070.

Chapter 4. Quantification of Local Zinc and Tungsten Deposits in Bone with LA-ICP-MS Using Novel Hydroxyapatite-Collagen Calibration Standards

4.1. Preface

In Chapter 3, LA-ICP-MS measurements in bone were found to be more sensitive and provide better image resolution than SR-μXRF. Another advantage of LA-ICP-MS is the possibility of quantitative measurements, though this requires matrix-matched calibration standards. In the following chapter, we develop and compare the accuracy of potential LA-ICP-MS calibration standards: bone (BN), 7:3 hydroxyapatite:collagen (HC), and hydroxyapatite (HA) spiked with tungsten and zinc. Using our novel calibration strategy, we subsequently determine the local concentrations of tungsten and zinc in bone. This work has been prepared in manuscript form for publishing in the *Journal of Analytical Atomic Spectrometry*. Data from Supplementary Information is incorporated into the chapter.

4.2. Introduction

Bone tissue has many functions beyond structural support, including generation of blood cells (hematopoiesis), mineral storage, mineral homeostasis, and metabolic functions.[1, 2] Specifically, bone is integral for the removal and storage of toxic metals, such as lead, from the blood stream along with the homeostasis of essential minerals and metals including calcium, phosphorus, zinc and iron. Tungsten, recently flagged as a potential toxin, has also been shown to accumulate in bone as polytungstates.[3-5] Polytungstates are known catalytic agents and more toxic than simple monotungstate, $[WO_4]^{2-}$.[6, 7] Their presence in bone is concerning since these species may interfere with essential bone functions. Indeed, studies suggest that tungsten may act as a tumor promoter by increasing DNA damage in bone marrow resident B lymphocytes.[8] In our recent work, we qualitatively mapped zinc and tungsten distribution in bone using synchrotron radiation micro-X-ray fluorescence (SR-μXRF) and laser ablation inductively coupled plasma mass spectrometry (LA-ICP-MS).[5, 9] We observed heterogeneous localization of tungsten in cortical and cancellous bone tissue (the site of red bone marrow and the production of blood cells). To conduct rigorous toxicological studies of tungsten's mode of action and uptake mechanism in bone, quantitative measurements are required. In addition, we observed the relative increase of

zinc in the edges of the bone shaft, the location of increased bone remodelling.[5] Zinc is known to accumulate at sites of calcification during remodeling.[10, 11]

LA-ICP-MS is a powerful analytical technique capable of measuring the spatial distribution of trace elements at a micrometer scale in a variety of solid samples.[12] Because the coupling of laser energy with the solid surface is matrix specific, a major barrier for quantitative measurements with LA-ICP-MS is the requirement of a matrix-matched calibration standard. Unfortunately, standard reference materials (SRMs) do not cover every type of sample and/or analyte. Moreover, calibration with SRMs is limited to a single-point calibration, which can be less accurate than multi-point calibration strategies. The latter are the norm for other quantitative techniques.[13] When no SRM is available, synthetic matrix-matched standards can be created and used for quantification.[14, 15] Doping synthetic standards with different concentrations of the analyte has the advantage of allowing for multi-point calibration.

Bone and teeth have been analyzed using LA-ICP-MS in several studies.[16-21] These tissues are composed of ~30% organic collagen and ~70% inorganic hydroxyapatite, $Ca_{10}(PO_4)_6(OH)_2$.[22] For LA-ICP-MS measurements in bone, the most commonly used SRMs are NIST SRM 1486 Bone Meal and NIST SRM 1400 Bone Ash.[12] However, fully certified values for many elements are not available for these two SRMs, which are certified for only eight elements: Ca, Mg, P, Fe, Pb, K, Sr and Zn. While uncertified elemental contents can be found elsewhere,[23] no information is available for tungsten. In addition, NIST SRM 1400 contains only the inorganic matrix of bone since all organic material is removed during the ashing process. Its matrix, therefore, has a relatively higher calcium content in terms of dry weight compared to bone.[20] Consequently, using NIST SRM 1400 as a calibration standard requires a mathematical correction generally involving normalization with the calcium concentration.

Beyond SRMs, synthetic calibration strategies primarily use pure hydroxyapatite prepared via (a) precipitation of hydroxyapatite and subsequent addition of multi-element solution,[16] (b) co-precipitation of hydroxyapatite with analytes,[17] or (c) dissolution of hydroxyapatite and addition of a multi-element solution followed by evaporation to dryness.[18] Hydroxyapatite standards, like NIST SRM 1400, do not contain any organic material and thus require mathematical correction using calcium concentration to yield accurate results. While some studies do account for the differences in calcium content,[16] it is not clear if all reports include this correction.[17, 18] The

accuracy of hydroxyapatite standards is generally validated by analysis of known elemental concentrations in NIST SRM 1486.

Correction by calcium concentration requires knowing the exact calcium content in both calibration standard and sample.[17] However, unlike calibration standards, calcium distribution is heterogeneous throughout intact bone tissue due to non-calcified components such as connective tissue and bone marrow.[1] Therefore, bulk determinations of calcium in bone may not be representative of local concentrations, which makes applying a correction dependent on calcium concentration fallacious for biological thin-sections. The organic matrix of bone collagen may also change the ablation characteristics of the bone, a phenomenon not modeled by hydroxyapatite calibration standards.[24, 25] Calibration standards which contain the correct ratio of organic to inorganic material are ideal so that correcting for differences in calcium content is not required and the possible effects of collagen on the ablation characteristics of bone are appropriately modeled. An obvious choice of material meeting these requirements is bone itself. The Parsons Group developed reference materials for the analysis of lead in bone from powdered long bones obtained from Pb-dosed and undosed animals.[20, 26] While this method proved successful at determining lead concentrations in NIST SRM 1486 without a mathematical correction, this strategy is time-consuming, expensive, and not optimal for routine analysis of metal content in bone. A cheaper, synthetic standard which contains the correct calcium content and incorporates bone's organic component is thus highly desirable.

To address these issues, a new procedure has been devised for producing two matrix-matched calibration standards for bone which account for both organic and inorganic fractions. Ground bone (BN) and 7:3 hydroyapatite:collagen (HC) calibration standards were spiked with varying concentrations of a multi-element standard solution. The homogeneity and analytical performance (accuracy, precision, limits of detection) of these standards were then studied and validated using NIST SRM 1486. The effect of matrix-matching calibration was assessed by comparing the calibration with BN and HC standards to that of synthetic hydroxyapatite (HA) standards. Finally, we reported quantitative results for the measurement of zinc and tungsten concentration in bone tissue using this methodology.

4.3. Experimental

4.3.1. Preparation of Enriched Calibration Standards

Three calibration matrices were prepared: i) bone (BN); ii) a 7:3 mixture of hydroxyapatite:collagen (HC); and iii) hydroxyapatite (HA). The ratio of 7:3 was chosen to mimic the composition of bone, which contains ~70% hydroxyapatite and ~30% collagen.[1] The BN matrix was prepared from the mouse long bones. Animal experiments were performed in the Lady Davis Institute Animal Care Facility following the guidelines of the McGill University Animal Care Committee–approved protocol. Four-week-old male C57BL/6 J mice were purchased from Charles Rivers Laboratories Inc. (Montréal, Canada) or bred in-house and given food and water *ad libitum*. After drying the long bones, they were ground using a Retsch MM400 ball mill (Retsch 10 mL Zirconia Jars; 10 mm diameter (3.0 g) Yttrium-stabilized zirconia balls) at 30 Hz for 30 mins. To prepare the HC matrix, collagen (from bovine achilles tendon, Millipore Sigma) was ground to a powder using the above ball mill at the same instrument settings. Hydroxyapatite (reagent grade, Millipore Sigma) and powdered collagen were then combined in 7:3 ratio by weight and mixed using the ball mill at 10 Hz power for 5 mins to ensure thorough mixing of the solid components. Hydroxyapatite (reagent grade, Millipore Sigma) was used directly for the HA calibration standards.

Once the solid matrices were prepared, approximately 150 mg of each matrix was placed in a glass vial of 2 mL MilliQ water. The samples were spiked with appropriate volumes of multi-element standard solution containing dissolved zinc ($ZnSO_4 \cdot 7H_2O$, Millipore Sigma) and tungsten ($Na_2WO_4 \cdot 2H_2O$, Millipore Sigma). Blank standards were also produced by not spiking the mixing solutions. All samples were mixed for 1 hour, followed by evaporation to dryness in a vacuum oven. Samples were manually homogenized using a mortar and pestle and compressed into a pellet. The samples were pressed into 5 mm diameter disks of ~1 mm of thickness using a manual hydraulic press (Parr Instrument Company). The resulting pellets were individually stored in small glass vials.

4.3.2. Preparation of Bone Tissue Samples

Animal derived samples were prepared as follows. After 1 week of acclimation, mice were exposed for 4 weeks to water with 15 ppm of tungsten prepared by dissolving the appropriate amount of sodium tungstate dihydrate ($Na_2WO_4 \cdot 2H_2O$; Millipore Sigma) in tap water. The water

was replaced every 2 or 3 days to limit conversion to polytungstate species. Daily water consumption between groups of mice did not differ ($\pm$ 0.16 mL/g).[8] As we have previously described,[8] no changes in animal weight, physical appearance, or water intake were observed in the tungsten-exposed group.

Following the individual exposure regimen, mice were euthanized by CO_2 asphyxiation followed by cardiac puncture or cervical dislocation. Sample thin sections (100–250 μm) were prepared and imaged with backscattered electron imaging (BEI), using the fixation and polishing method previously reported.[5] Briefly, bone samples were fixed in 4% paraformaldehyde before being dehydrated and mounted in methyl methacrylate. From there, samples were sectioned using a diamond saw and polished into thin sections using a series of fine grit silicon carbide paper and diamond suspensions. The BEI shows dense, calcium-containing cortical and cancellous bone but not lighter organic cartilage and bone marrow, providing a reference image of bone morphology.

4.3.3. Solution Mode Elemental Analysis

ICP-MS solution analysis was conducted at McGill University using a thermo iCAPQ ICP-MS operated in standard mode. Instrument operating conditions are listed in Table 4.1. Solution ICP-MS was used to quantify the zinc and tungsten concentrations in BN, HC and HA calibration standards and bulk bone samples.

To prepare samples for elemental analysis, ~30 mg of sample was weighed and transferred to a 50 mL glass volumetric flask. Elemental analysis results from glass flasks were compared to those obtained using plastic vessels with no difference in metal concentrations evident. Concentrated nitric acid (HNO_3; TraceMetal Grade; Fischer Chemical), 1 mL, was added to the samples and the vials were capped and heated to ~90ºC for 1 hour in a sand bath. Hydrogen peroxide (H_2O_2; >30%, for trace analysis; Millipore Sigma), 2mL, was then added and the samples were kept at ~90ºC for 1 hour. After cooling, samples were diluted to 50 mL with stock solution and weighed. The stock solution was composed of a ratio of 78.3:10:9.7:1:1 MilliQ water (18.2 MOhms; Millipore): acetic acid (CH_3COOH; Optima; Fischer Chemical): ammonium hydroxide (NH_4OH; TraceMetal Grade; Fischer Chemical): hydrofluoric acid (HF; 1%; Millipore Sigma): Ge internal standard (1ppm; SCP Science). The stock solution was optimized to promote solubility of tungsten and hydroxyapatite; tungsten forms insoluble polytungstates at low pHs while hydroxyapatite precipitates at basic pHs. Using a minute amount of HF to promote solubility of any potential polytungstates, as well as acetic acid to buffer the solution to a final pH of ~ 4.6, was

found to provide optimal solubility conditions. Solutions were filtered with a syringe filter prior to analysis with ICP-MS. Reliable quantification of the analytes was achieved by conventional solution nebulization ICP-MS using matrix-matched calibration with ^{73}Ge as an internal standard. Three replicates were run per sample.

ICP-MS	Thermo iCAPQ ICP-MS
Rf power	1550 W
Nebulizer	microflow nebulizer
Spray chamber	concentric
Ar flow rates (Plasma gas and Auxiliary gas)	1.05 L/min
Isotopes	^{66}Zn, ^{182}W
Dwell time	0.01 s
Signal acquisition	STD mode

Table 4.1. ICP-MS operating conditions for solution elemental analysis

4.3.4. LA-ICP-MS Parameters

Analysis of elemental distribution in bone was performed with LA-ICP-MS at the Dartmouth Trace Element Analysis Lab. LA was carried out with a NWR213 laser (Elemental Scientific Lasers, Bozeman, Montana). Elemental detection was performed with an Agilent 7900 ICP-MS (Santa Clara, CA) set to monitor Ca, Zn, and W (at m/z 43, 66, and 182, respectively). Sampling parameters are summarized in Table 4.2.

After focusing on the calibration standard pellet (BN, HC, HA), five 1600 μm lines were ablated on the surface using 4μm, 15μm, and 50μm spot sizes. For each line, the average intensity data of the isotopes of interest was computed, removing outliers greater than 3.5 standard deviations. The overall average of the five lines was determined and then normalized against the ^{43}Ca signal after subtraction of the mean background signal. Normalized counts were plotted versus concentration (determined by solution ICP-MS) to generate a calibration curve.

On the bone thin sections, data was collected in the area of interest using a 15 μm spot size. Because bone thin sections contain areas with and without calcium, it is not possible to normalize all the intensity data against the ^{43}Ca signal in the same manner as the calibration standards. Instead, regions of bone were selected with similar ^{43}Ca signals (< 5% relative standard deviation, RSD). In these regions, the analyte signal was normalized by the ^{43}Ca signal after subtraction of the background. Concentration was determined using the HC calibration curve at 15 μm step-size.

Calcium, zinc, and tungsten distribution maps were generated by plotting intensity data using MATLAB (scripts available at https://github.com/davidkuter/ICP-MS). A histogram analysis was performed on the intensity data to determine upper and lower limits of LA-ICP-MS plots. These values were selected as such to exclude the bottom and top 0.5% of the outlying data.

Laser	Nd-YAG
Wavelength	213 nm
Repetition rate	20 Hz
Ar gas flow	950 ml/min
He flow rate	700 ml/min
Scan speed	60 µm/sec
Energy	75%
Fluence	~7 J/cm^2
Spot size (diameter)	4 µm, 15 µm, 50 µm
ICP-MS	Agilent 7900 ICP-MS
Rf power	1550 W
Ar flow rates *(*Plasma gas and Auxiliary gas)	0.95 and 1.0 L/min
Isotopes	^{43}Ca, ^{66}Zn, ^{182}W
Dwell time	0.0475 s

Table 4.2. LA-ICP-MS operating conditions

4.4. Results and Discussion

4.4.1. Quality of Pressed Powder Calibration Standards

The homogeneity of the elemental composition of the BN, HC and HA standards were studied by ablating five lines (1600 µm scan lines spaced 100 µm apart, operating conditions listed in Table 4.2.) on each pellet surface. The reproducibility (%RSD) of the normalized counts for each isotope at 4µm, 15µm, and 50µm spot sizes are listed in Table 4.3. The majority of the values are below 10%, with many values beneath 5%. The highest RSD values are found for zinc distribution in the BN standards, for samples with concentrations less than 1 µg g^{-1}, and at spot sizes of 4 µm. Imperfect homogenization of the BN matrix prior to spiking with zinc may result in some heterogeneity of the zinc distribution since bone contains a naturally high level of zinc. Similarly, a higher %RSD at a 4 µm spot size indicates that elemental distribution may be heterogeneous at this spot size. These results demonstrate that the solution mixing method for

doping calibration standards produces the most homogeneous distribution of zinc and tungsten in the HC and HA standards at 15 µm and 50 µm spot sizes. Reproducibility of the zinc signal in NIST SRM 1486 for four measurements also demonstrates homogeneous distribution with RSD values below 12% for all measurements. NIST SRM 1486 does not contain an appreciable amount of tungsten.

Matrix	Zinc Concentration ($\mu g\ g^{-1}$)	LA-ICP-MS %RSD (n=5) at spot size: 4 µm	15 µm	50 µm	Tungsten Concentration ($\mu g\ g^{-1}$)	LA-ICP-MS %RSD (n=5) at spot size: 4 µm	15 µm	50 µm
BN:	187 (0.4)	3.4	5.2	6.0	0.75 (0.2)	12.4	17.8	14.9
	195 (1.7)	6.6	6.4	10.3	4.43 (0.3)	3.2	9.8	7.0
	220 (1.2)	11.5	7.3	5.5	8.54 (0.4)	2.2	6.4	7.0
	247 (0.6)	10.7	2.5	5.1	21.7 (0.3)	5.3	5.8	4.7
	280 (1.5)	5.0	3.3	12.2	45.2 (0.2)	5.2	2.0	1.5
	310 (1.1)	6.1	4.2	14.2	64.2 (0.5)	2.9	3.8	2.9
HC:	35.3 (1.1)	4.5	5.2	2.6	0.62 (0.8)	13.5	4.1	7.9
	44.2 (1.0)	2.5	3.2	1.3	2.61 (0.5)	5.8	3.2	2.8
	89 (1.2)	5.5	5.8	2.1	3.47 (0.2)	3.8	3.0	2.6
	110 (1.3)	3.9	3.4	5.3	19.8 (0.3)	4.1	1.8	1.3
	119 (0.8)	4.6	4.3	2.7	46.1 (1.0)	5.8	3.8	3.8
	252 (0.1)	3.4	2.6	7.5	67.8 (0.3)	1.8	3.3	8.5
HA:	33.8 (1.8)	2.6	4.0	3.5	2.89 (0.3)	10.6	3.3	2.3
	44.7 (1.2)	4.5	3.2	5.2	3.74 (0.1)	15.5	9.5	6.4
	87 (1.1)	4.9	4.9	4.0	5.40 (0.5)	8.3	2.5	2.4
	117 (1.4)	3.8	2.9	4.5	11.6 (0.2)	3.7	3.1	3.1
	122 (1.1)	3.8	7.4	5.3	42.7 (0.5)	2.2	0.7	2.6
	244 (1.4)	3.0	2.3	5.4	68.2 (0.1)	3.4	1.9	3.7
NIST SRM 1486:	-	6.5	11.7	9.9	-	-	-	-

Table 4.3. Zinc and tungsten concentration and homogeneity of enriched BN, HC, HA and NIST SRM 1486 standards at 4µm, 15µm, and 50µm spot sizes. Data is normalized to ^{43}Ca. Concentrations are quantified by solution based ICP-MS and reported with relative standard deviations (%RSD).

4.4.2. Analytical Assessment for Calibration Purposes

The analytical performance of the synthesized pressed powder BN, HC, and HA and calibration standards were evaluated in terms of linearity, limits of detection (LOD), and accuracy. Details about the calibration curves (concentration range, linear regression) are given in Table 4.4.

Analyte	Spot Size	Matrix	Concentration range ($\mu g\ g^{-1}$)	Calibration Curve (y = mx+b)	
				m	*b*
⁶⁶Zn	4 μm	**BONE:**	187.33 - 309.61	7.47E-04	-7.27E-02
		HC:	35.29-252.14	2.54E-04	6.96E-04
		HA:	33.83-243.67	1.64E-04	-9.37E-04
	15 μm	**BONE:**	187.33 - 309.61	5.28E-04	-4.51E-02
		HC:	35.29-252.14	1.98E-04	-1.08E-03
		HA:	33.83-243.67	1.46E-04	-6.11E-05
	50 μm	**BONE:**	187.33 - 309.61	7.50E-04	-8.83E-02
		HC:	35.29-252.14	1.89E-04	-1.29E-03
		HA:	33.83-243.67	1.27E-04	-5.60E-04
¹⁸²W	4 μm	**BONE:**	0.75 - 64.21	1.62E-03	1.51E-03
		HC:	0.62-67.89	9.92E-04	2.62E-04
		HA:	2.89-68.21	7.95E-04	-6.17E-04
	15 μm	**BONE:**	0.75 - 64.21	1.10E-03	1.64E-03
		HC:	0.62-67.89	7.34E-04	1.63E-04
		HA:	2.89-68.21	6.97E-04	-6.24E-04
	50 μm	**BONE:**	0.75 - 64.21	9.70E-04	4.88E-03
		HC:	0.62-67.89	7.78E-04	-1.76E-04
		HA:	2.89-68.21	6.23E-04	-8.39E-04

Table 4.4. Concentration range and linear regression for zinc and tungsten calibration curves with BONE, HC and HA calibration standards.

Analyte	Spot Size	Matrix	Coefficient of Determination, R^2	LOD ($\mu g\ g^{-1}$)
⁶⁶Zn	4 um	**BN:**	0.9271	3.8
		HC:	0.9979	1.9
		HA:	0.9947	11
	15 um	**BN:**	0.9692	0.47
		HC:	0.9972	0.24
		HA:	0.9898	1.1
	50 um	**BN:**	0.9075	0.10
		HC:	0.9964	0.13
		HA:	0.9933	0.54
¹⁸²W	4 um	**BN:**	0.9993	0.25
		HC:	0.9985	0.068
		HA:	0.9943	0.32
	15 um	**BN:**	0.9990	0.043
		HC:	0.9992	0.012
		HA:	0.9806	0.043
	50 um	**BN:**	0.9956	0.0055
		HC:	0.9993	0.0022
		HA:	0.9974	0.0078

Table 4.5. Analytical performance of the method.

LA-ICP-MS calibration graphs of the enriched HA and HC pellets demonstrated a good linearity for all the analytes in both HA and HC matrices (Table 4.5.) with $R^2 > 0.994$ in most

cases. This confirms the strong correlation between the calculated concentrations and signal response of the ablated aerosol of the calibration standards. While the enriched BN pellets also demonstrated a good linearity $R^2 > 0.995$ for tungsten, the linearity was less for zinc ($R^2 > 0.90$). The LOD was defined as 3 times the standard deviation for n = 115 replicate measurements of the corresponding analyte signal of a gas blank normalized to subsequent ^{43}Ca signal of the blank BN, HC or HA standard. LOD's are reported in Table 4.5. and ranged between 11 µg g^{-1} for zinc in HA at a 4 µm spot size, to 0.0022 µg g^{-1} for tungsten in HC at a 50 µm spot size.

The accuracy of the three calibration standards, matrix-matched BN and HC along with nonmatrix-matched HA, were evaluated by quantifying zinc in NIST SRM 1486 through external calibration (without any corrections for calcium content) and comparing to the known reference value of zinc. As displayed in Table 4.6., both BN and HC standards provided accurate measurement of the zinc concentration in NIST SRM 1486 at all spot sizes, within the 95% confidence interval (using unpaired T-test analysis). Conversely, enriched HA standards overestimated the analyte concentrations.

Reference Value (µg g^{-1})	Measured Value (µg g^{-1})			
	Spot Size	BN	HC	HA
	4 µm	146 ± 10	141 ± 9.2	229 ± 15
147 ± 16	15 µm	141 ± 17	154 ± 18	202 ± 24
	50 µm	153 ± 15	148 ± 15	215 ± 21

Table 4.6. Quantitative analysis of the reference material NIST SRM 1486 Bone meal obtained by external calibration with enriched BN, HC, and HA standards.

These results re-iterate the importance of matrix-matched calibration standards to quantify metals in bone. HC calibration standards, by including both organic and inorganic components of bone, mimic the matrix of bone more closely than HA. Both matrix-matched standards, BN and HC, provided accurate quantification of zinc in NIST SRM 1486 without a correction for calcium content. Since it is difficult to determine local calcium concentrations in bone and, accordingly, apply a correction based on this information, calibration standards which do not require this additional step are ideal. These results also indicate that HC, which is both easier and cheaper to produce than BN, is a suitable synthetic calibration standard for the determination of metal concentrations in bone. Furthermore, BN calibration standards may already contain high concentrations of metals, such as zinc, which can substantially raise the metal concentration of the

lowest calibration point in the curve. Compared to the HC blank zinc concentration of 35.3 µg g^{-1}, the BN blank sample zinc concentration is 187 µg g^{-1} (Table 4.3.), which is actually higher than the NIST SRM 1486 reference value for zinc (147 µg g^{-1}). Presence of naturally occurring metals in bone may also result in more heterogeneous distribution of metals in the pellet if the sample is not perfectly homogenized, leading to higher %RSD and a loss of linearity in the calibration curve (Table 4.3. and 4.5.). Therefore, taking accuracy, sensitivity, and homogeneity into consideration, HC is the best LA-ICP-MS calibration standard to use for external calibration of metals in bone.

4.4.3. Quantification of Zinc and Tungsten in Mouse Femur

Tungsten and zinc heterogeneously accumulate in bone tissue but have not been quantified due to the lack of appropriate calibration standards, specifically for tungsten. LA-ICP-MS elemental maps for calcium, tungsten, and zinc in the femoral bone of a mouse exposed to 15 ppm tungsten for four weeks are shown in Figure 4.1., with intensity reported as the raw counts (color scaled as max/ min). Maps were collected in both the cancellous and cortical tissue using a 15 µm spot size.

To quantify tungsten and zinc deposits, measurement areas (spots A-D) were selected to represent both high and low tungsten/zinc concentrations while maintaining a consistent calcium profile. While bone tissue in general has a homogeneous distribution of calcium, calcium counts decrease at the bone edge or at pores in the bone due its "spongy" nature, complicating analysis. A consistent calcium profile is essential for accurate quantification since variation in the calcium raw count would have a significant effect on the normalized value (analyte count/ Ca count) of the element of interest. The %RSD of average Ca counts between all spots was small (5%), allowing for direct concentration comparison between the regions of interest.
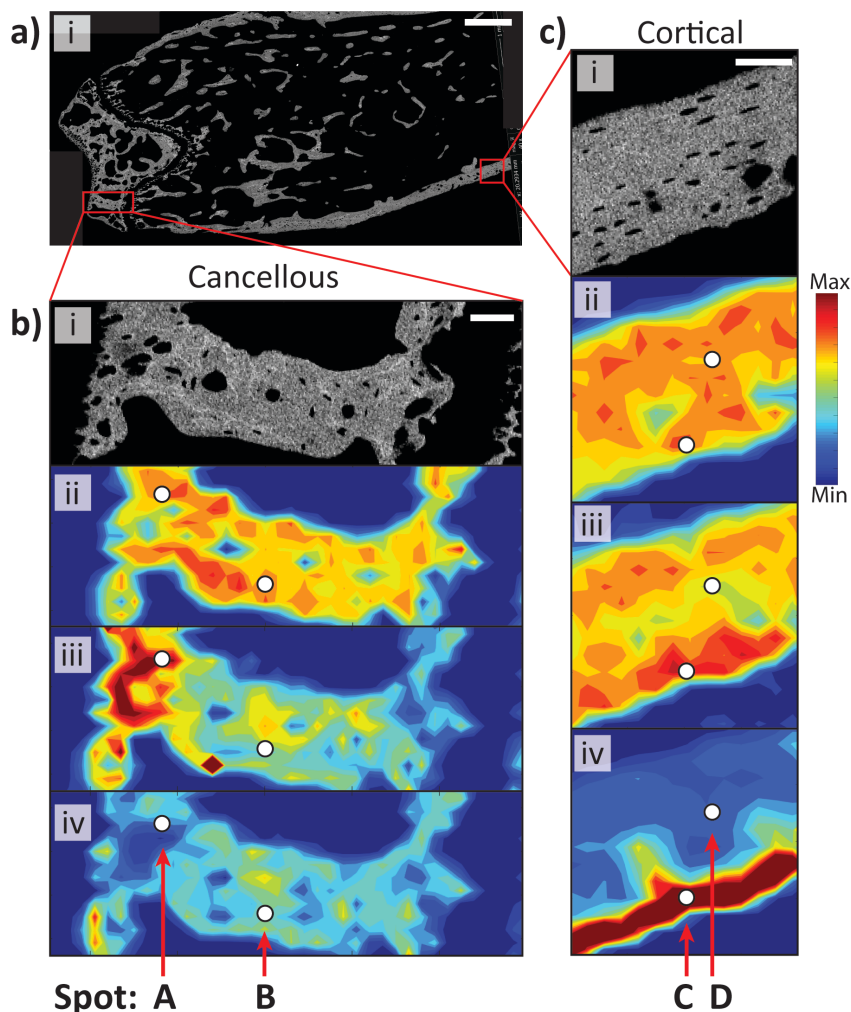
Figure 4.1. Quantification of tungsten and zinc deposits in bone. (ai) BEI of femoral bone from mouse treated orally with 15 ppm of tungsten for four weeks (scale bar = 500 μm). Magnified BEI images of cancellous (bi) and cortical (ci) are indicated by the red boxes (scale bar = 50 μm). Panels (ii), (iii), and (iv) are LA-ICP-MS ^{43}Ca, ^{182}W, and ^{66}Zn distribution maps, respectively. Intensity, indicated by the max – min scale, is in elemental counts. Spot A, B, C and D represent the regions where zinc and tungsten were quantified in bone.

Spot	A	B	C	D	Bulk
[W]/ μg g^{-1}	15.7	5.6	12.8	10.7	7.5 ± 0.30
[Zn]/ μg g^{-1}	142	276	942	135	211 ± 17

Table 4.7. Localized concentration of tungsten and zinc in bone from a mouse exposed to 15 ppm of tungsten for four weeks. Location of spots A-D indicated in Figure 4.1.

Local tungsten and zinc concentrations were determined by normalizing analyte counts with the ^{43}Ca signal in the region of interest, followed by converting normalized counts to concentration through external calibration with the HC standard. Bulk tungsten and zinc

concentrations in long bone were determined using solution ICP-MS. Samples were taken from the same mouse from which the thin-sections were prepared. Results are reported in Table 4.7.

Figure 4.1. shows an extremely high accumulation of zinc at the edge of the cortical bone in the bone shaft, similar to previous studies which observed the same feature.[5] Zinc is known to deposit at the cement lines between calcified and uncalcified bone and thus the high accumulation in this region is likely connected to the increased remodeling activity associated with the changing width of the long bone in these young, growing mice.[10] As seen in Table 4.7., the concentration of this zinc deposit (942 μg g^{-1}) is significantly higher than bulk determinations of zinc in bone (211 μg g^{-1}). While zinc is known to be essential to bone homeostasis, its exact form and mode of action at sites of calcification remains unknown.[27]

As reported previously,[5] the highest concentrations of tungsten are observed in cancellous tissue, followed by the outer edges of cortical bone. Quantification results demonstrate that tungsten is deposited in these regions at significantly higher concentrations (15.7 and 12.8 μg g^{-1} respectively) than indicated by solution ICP-MS measurements of tungsten concentration in the bulk bone (7.5 μg g^{-1}). When determining the potential toxic impacts of tungsten to bone cells, it is essential to consider the concentrations in which tungsten is elevated in the area of interest compared to the bulk bone alone. Increased tungsten concentration may also point to the formation of polytungstates which are more toxic than their monotungstate counterparts.[7] Polytungstates accumulate in bone following oral exposure to dissolved monotungstate.[5] Determining local tungsten distribution and form also has implications for developing future remediation strategies.

4.5. Conclusions

Quantitative analysis of zinc and tungsten in bone tissue was achieved using 7:3 hydroxyapatite: collagen calibration (HC) standards. The synthesized HC standards displayed sufficient homogeneity, sensitivity, precision, and a higher degree of accuracy compared to bone (BN) and hydroxyapatite (HA) calibration standards when validated with NIST SRM 1486 Bone Meal. Improved accuracy for HC compared to HA is credited to the improved bone matrix-matching capabilities of HC, since HC incorporates both organic and inorganic components while HA is comprised of only the inorganic matrix of bone.

This calibration method was used to quantify local zinc and tungsten deposits in the cancellous and cortical tissue of the femoral bone of a mouse exposed to 15 ppm of tungsten for

four weeks. Zinc and tungsten were found in concentrations as high as 942 μg g^{-1} and 15.7 μg g^{-1} respectively, much higher than bulk measurements of these metals. These results point to the importance of localized measurements of metal distribution in bone, as bulk determinations of concentrations could be misleading. Determining the local concentrations of tungsten improves understanding of the possible toxicological consequences of exposure as well as aiding in the development of appropriate treatment strategies.

4.6. References

1.   Clarke, B. Normal Bone Anatomy and Physiology. *Clinical Journal of the American Society of Nephrology* **2008,** *3* (Supplement 3), S131.

2.   Taichman, R. S. Blood and Bone: Two Tissues Whose Fates Are Intertwined to Create the Hematopoietic Stem-Cell Niche. *Blood* **2005,** *105* (7), 2631-2639.

3.   Guandalini, G. S.; Zhang, L.; Fornero, E.; Centeno, J. A.; Mokashi, V. P.; Ortiz, P. A.; Stockelman, M. D.; Osterburg, A. R.; Chapman, G. G. Tissue Distribution of Tungsten in Mice Following Oral Exposure to Sodium Tungstate. *Chemical Research in Toxicology* **2011,** *24* (4), 488-493.

4.   Lemus, R.; Venezia, C. F. An Update to the Toxicological Profile for Water-Soluble and Sparingly Soluble Tungsten Substances. *Critical reviews in toxicology* **2015,** *45* (5), 388-411.

5.   VanderSchee, C. R.; Kuter, D.; Bolt, A. M.; Lo, F.-C.; Feng, R.; Thieme, J.; Chen-Wiegart, Y.-c. K.; Williams, G.; Mann, K. K.; Bohle, D. S. Accumulation of Persistent Tungsten in Bone as in Situ Generated Polytungstate. *Communications Chemistry* **2018,** *1* (1), 8.

6.   Wang, S.-S.; Yang, G.-Y. Recent Advances in Polyoxometalate-Catalyzed Reactions. *Chemical Reviews* **2015,** *115* (11), 4893-4962.

7.   Strigul, N. Does Speciation Matter for Tungsten Ecotoxicology? *Ecotoxicology and Environmental Safety* **2010,** *73* (6), 1099-1113.

8.   Kelly, A. D. R.; Lemaire, M.; Young, Y. K.; Eustache, J. H.; Guilbert, C.; Molina, M. F.; Mann, K. K. In Vivo Tungsten Exposure Alters B-Cell Development and Increases DNA Damage in Murine Bone Marrow. *Toxicological Sciences* **2012,** *131* (2), 434-446.

9.   VanderSchee, C. R.; Kuter, D.; Chou, H.; Jackson, B. P.; Mann, K. K.; Bohle, D. S. Addressing K/L-Edge Overlap in Elemental Analysis from Micro-X-Ray Fluorescence: Bioimaging of Tungsten and Zinc in Bone Tissue Using Synchrotron Radiation and Laser Ablation Inductively Coupled Plasma Mass Spectrometry. *Analytical and Bioanalytical Chemistry* **2020,** *412* (2), 259-265.

10.   Haumont, S. Distribution of Zinc in Bone Tissue. *Journal of Histochemistry & Cytochemistry* **1961,** *9* (2), 141-145.

11.   Gomez, S.; Rizzo, R.; Pozzi-Mucelli, M.; Bonucci, E.; Vittur, F. Zinc Mapping in Bone Tissues by Histochemistry and Synchrotron Radiation–Induced X-Ray Emission: Correlation with the Distribution of Alkaline Phosphatase. *Bone* **1999,** *25* (1), 33-38.

12.   Miliszkiewicz, N.; Walas, S.; Tobiasz, A. Current Approaches to Calibration of La-Icp-Ms Analysis. *Journal of Analytical Atomic Spectrometry* **2015,** *30* (2), 327-338.

13.   Khamis, M. M.; Klemm, N.; Adamko, D. J.; El-Aneed, A. Comparison of Accuracy and Precision between Multipoint Calibration, Single Point Calibration, and Relative Quantification for Targeted Metabolomic Analysis. *Analytical and Bioanalytical Chemistry* **2018,** *410* (23), 5899-5913.

14.   Bellotto, V. R.; Miekeley, N. Improvements in Calibration Procedures for the Quantitative Determination of Trace Elements in Carbonate Material (Mussel Shells) by Laser Ablation Icp-Ms. *Fresenius' Journal of Analytical Chemistry* **2000,** *367* (7), 635-640.

15.   Hare, D.; Austin, C.; Doble, P. Quantification Strategies for Elemental Imaging of Biological Samples Using Laser Ablation-Inductively Coupled Plasma-Mass Spectrometry. *Analyst* **2012,** *137* (7), 1527-1537.

16.   Gruhl, S.; Witte, F.; Vogt, J.; Vogt, C. Determination of Concentration Gradients in Bone Tissue Generated by a Biologically Degradable Magnesium Implant. *Journal of Analytical Atomic Spectrometry* **2009,** *24* (2), 181-188.

17.   Ugarte, A.; Unceta, N.; Pécheyran, C.; Goicolea, M. A.; Barrio, R. J. Development of Matrix-Matching Hydroxyapatite Calibration Standards for Quantitative Multi-Element La-Icp-Ms Analysis: Application to the Dorsal Spine of Fish. *Journal of Analytical Atomic Spectrometry* **2011,** *26* (7), 1421-1427.

18.   Stadlbauer, C.; Reiter, C.; Patzak, B.; Stingeder, G.; Prohaska, T. History of Individuals of the 18th/19th Centuries Stored in Bones, Teeth, and Hair Analyzed by La–Icp–Ms—a Step in Attempts to Confirm the Authenticity of Mozart's Skull. *Analytical and Bioanalytical Chemistry* **2007,** *388* (3), 593-602.

19.   Uryu, T.; Yoshinaga, J.; Yanagisawa, Y.; Endo, M.; Takahashi, J. Analysis of Lead in Tooth Enamel by Laser Ablation-Inductively Coupled Plasma-Mass Spectrometry. *Analytical Sciences* **2003,** *19* (10), 1413-6.

20.   Bellis, D. J.; Hetter, K. M.; Jones, J.; Amarasiriwardena, D.; Parsons, P. J. Calibration of Laser Ablation Inductively Coupled Plasma Mass Spectrometry for Quantitative Measurements of Lead in Bone. *Journal of Analytical Atomic Spectrometry* **2006,** *21* (9), 948-954.

21. Hanć, A.; Olszewska, A.; Barałkiewicz, D. Quantitative Analysis of Elements Migration in Human Teeth with and without Filling Using La-Icp-Ms. *Microchemical Journal* **2013,** *110*, 61-69.

22. Shea, J. E.; Miller, S. C. Skeletal Function and Structure: Implications for Tissue-Targeted Therapeutics. *Advanced Drug Delivery Reviews* **2005,** *57* (7), 945-957.

23. Jochum, K. P.; Nohl, U.; Herwig, K.; Lammel, E.; Stoll, B.; Hofmann, A. W. Georem: A New Geochemical Database for Reference Materials and Isotopic Standards. *Geostandards and Geoanalytical Research* **2005,** *29* (3), 333-338.

24. Lalande, M.; Schwob, L.; Vizcaino, V.; Chirot, F.; Dugourd, P.; Schlathölter, T.; Poully, J.-C. Direct Radiation Effects on the Structure and Stability of Collagen and Other Proteins. *ChemBioChem* **2019,** *20* (24), 2972-2980.

25. Egorov, D.; Hoekstra, R.; Schlathölter, T. A Comparative Vuv Absorption Mass-Spectroscopy Study on Protonated Peptides of Different Size. *Physical Chemistry Chemical Physics* **2017,** *19* (31), 20608-20618.

26. Hetter, K. M.; Bellis, D. J.; Geraghty, C.; Todd, A. C.; Parsons, P. J. Development of Candidate Reference Materials for the Measurement of Lead in Bone. *Analytical and Bioanalytical Chemistry* **2008,** *391* (6), 2011-2021.

27. Huang, T.; Yan, G.; Guan, M. Zinc Homeostasis in Bone: Zinc Transporters and Bone Diseases. *International journal of molecular sciences* **2020,** *21* (4), 1236.

Chapter 5. Identification of Local Copper and Zinc Deposits in Bone Tissue

5.1. Preface

XRF is a powerful technique capable of simultaneously detecting the presence of multiple elements in a sample. This powerful ability can lead to unexpected results and new avenues of research. This chapter presents one such example. While using XRF to map tungsten distribution in the bones of tungsten treated mice (Chapter 2), we serendipitously detected highly localized deposits of copper and zinc. Figure 5.1. shows a representative XRF spectrum of bone from a mouse exposed to tungsten in water. Zinc and copper emission lines are clearly evident. Furthermore, these signals were not affected by treatment with or absence of tungsten.
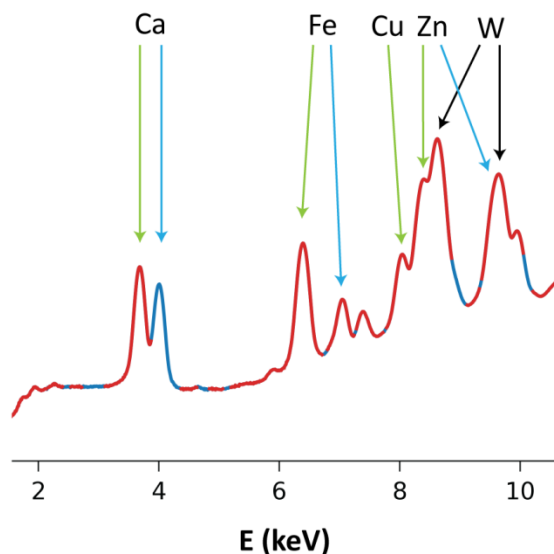
Figure 5.1. XRF spectrum in the bone of a tungsten-treated mouse. K_α, K_β and L emission lines indicated by green, blue and black arrows, respectively.

In this chapter, we apply the X-ray techniques described in Chapter 2 to investigate copper and zinc in bone tissue. SR-μXRF will be employed to map specific distribution while XAS will be utilized to gain structural information of these metals and elucidate their role in bone.

5.2. Introduction

Copper and zinc are key essential elements in the human body. They are present in numerous enzymes, including those required for maintaining healthy bone functioning.[1-3] The need for copper in the maintenance and biosynthesis of bone and connective tissues is well established.[4] Zinc is known to play a key role in bone formation and bone resorption.[5]

One of the primary known roles of copper in bone tissue is in the metalloenzyme lysyl oxidase (LOX), a copper-dependent amino oxidase containing a mononuclear copper(II) active site.[6] The LOX family are responsible for collagen and elastin cross-linking.[7] Cross-linking between collagen fibrils strengthens collagen's ability to provide mechanical stability and integrity to tissues.[8] Collagen is found in many tissues of the body, including articular cartilage, ligament, tendon, and bone.[9] Bone and ligaments are composed primarily of collagen type I, while articular cartilage is primarily composed of collagen type II.[10-12] Articular cartilage is a highly specialized connective tissue found in joints which provides a smooth, lubricated surface for low friction articulation and facilitates the transmission of loads to the underlying subchondral bone.[13]

The degree of collagen cross-linking, and by extension LOX activity, are tissue specific and likely related to their individual physiological functions rather than the particular type of collagen.[14] Collagen in bone and ligament form large fibers with extensive cross-linking due to their need for high tensile strength. The extracellular matrix of articular cartilage contains a large amount of water held by collagen-proteoglycan complexes with branching networks of collagen fibers embedded in amorphous proteoglycan aggregates. The collagen fibers in articular cartilage are relatively small and without the criss-cross pattern seen in other types of cartilage.
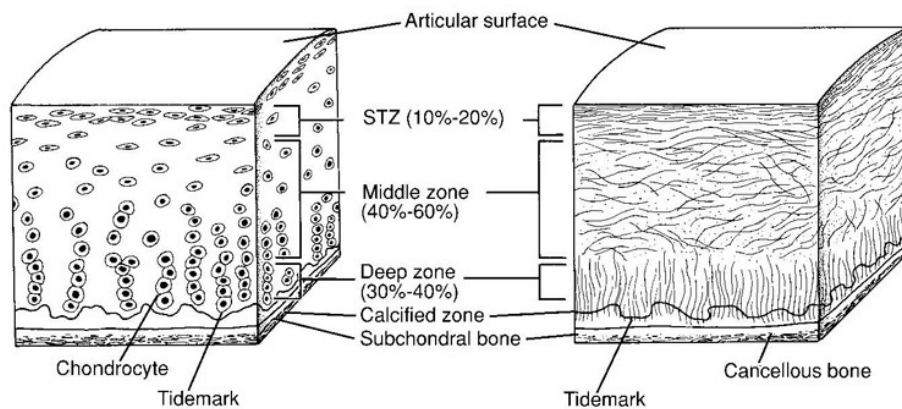

Figure 5.2. Chondrocyte organization and collagen fiber architecture in the three main zones of articular cartilage. Reprinted with permission.[15]

Articular cartilage is separated into zones which are differentiated by collagen fiber ultrastructure and organization of chondrocytes, the cells found in cartilage (Figure 5.2.).[15] Collagen in the superficial (transitional) zone is packed tightly and aligned parallel to the articular surface.[13] This zone is responsible for most of the tensile properties of cartilage. In the middle zone, collagen fibrils are larger and organized obliquely. The deep zone contains the largest diameter collagen fibrils arrange perpendicular to the articular surface. The calcified zone and deep zone are separated by the tidemark, which represents the mineralizing front in articular cartilage.

Large amounts of zinc have been found in the tidemark of articular cartilage and other sites of calcification, including the cement line between calcified and uncalcified bone.[16-18] As described in Chapter 2-4, we also observed heterogeneous zinc distribution in bone. The form(s) of zinc in these sites has not yet been positively identified. Suggestions include zinc incorporation into newly formed bone or storage of a zinc-containing enzyme. Two metalloenzyme candidates include matrix metalloproteinase (MMP),[19] which play an important role in the degradation of collagen during bone remodeling, and bone alkaline phosphatase (ALP). ALP is a membrane-bound metalloenzyme essential in bone formation and mineralization.[20-22] The active site includes one magnesium (II) and two zinc (II) ions. Bone ALP is considered a highly specific marker of calcification within bone.[23, 24] In articular cartilage, the tidemark is known to be an area of metabolic calcification[25] and correlates to the location of ALP activity.[26]

In this chapter, the distribution of copper and zinc in the articular cartilage and calcified bone of the hip and knee joint will be investigated using SR-μXRF. Subsequently, XAS spectra will be collected in areas of high copper and zinc accumulation. The X-ray absorption near-edge structure (XANES) spectra of bone samples will then be compared to reference standards and literature spectra, to elucidate the form and role of copper and zinc at locations of accumulation.

5.3. Experimental

5.3.1. Preparation of Bone Samples

Animal experiments were performed under a McGill University Animal Care Committee approved protocol. Four-week-old male C57BL/6J mice were purchased from Charles Rivers Laboratories Inc. (Montréal, Quebéc) or bred in house and given food and water *ad libitum*. Mice were euthanized by CO_2 asphyxiation followed by cardiac puncture or cervical dislocation. Tibia

and femur bones were removed and placed for one week in a solution of 4% paraformaldehyde for fixation. Bones were then washed three times with a solution of 1% phosphate-buffered solution (PBS) at pH 7.4 and stored in the same solution.

Adult human articular cartilage was obtained from the femoral head of patients suffering from either osteoarthritis (OA) (female, 68yrs) or hip fracture (female, 75 yrs) who were undergoing total hip replacement operations. Articular cartilage in the femoral head was classified as normal (fracture) or degenerated (OA), as determined by examination of the specimens using light microscopy. The femoral head was sectioned to obtain a ~5 mm sample. The sample was then fixated in 4% paraformaldehyde for one week before being washed three times and stored in a 1% phosphate-buffered solution (PBS) at pH 7.4.

After fixation, mouse and human samples were prepared for analysis by the same method. To mount the samples, bones were dehydrated using a series of alcohol washes followed by washes with xylene and MMA before finally being set in MMA. Using a diamond saw, samples were cut to a thickness of approximately 100 μm, exposing the surface of interest. They were polished using 600 grit silicon carbide paper and 6 μm and 1 μm diamond suspension.

5.3.2. SR-μXRF and μXANES

SR-μXRF and *in vivo* copper and zinc K-edge μXANES measurements were performed at the Advanced Photon Source (APS), Argonne National Laboratory, Argonne, Illinois, USA. Experiments on mouse samples were conducted at GSECARS station 13-ID-E while measurements on human samples were completed at CLS @ APS 20-ID-B (PNC-XSD-ID).

At 13-ID-E, μXRF mapping used monochromatic 10.5 keV X-rays from the APS undulator source selected with a Si(111) double-crystal monochromator and harmonic rejection mirrors to remove higher energies. This beam was focused to 2x2 μm using Kirkpatrick-Baez mirrors. The sample was placed at 45° to the incident beam and rastered through the beam. A 4-element silicon drift detector, at 45° to the sample and 90° to the incident beam, was used to measure XRF spectra at 5 μm intervals. Mouse SR-μXRF maps were prepared using GSE map viewer, an application of Larch.[27] *In vivo* copper and zinc K-edge μXANES spectra were collected in the mouse samples on regions of high elemental concentration as revealed by the SR-μXRF maps. μ-XANES spectra were also collected on copper (CuO, Cu_2O, CuS, $CuSO_4$) and zinc ($ZnSO_4$, $ZnCO_3$, $ZnPO_3$, ZnS,

ZnO, Zn-tetratolylporphyrin (TTP)) standards. The Si (111) monochromator was calibrated using zinc foil. Copper K-edge μXANES and zinc K-edge μXANES were collected over an energy range from 8,880 to 9423eV and 9,559 to 10,288eV, respectively, with a spot size of 2×2μm on the sample provided by Kirkpatrick-Baez (KB) mirror focusing. A 13-element Ge detector situated at 45° with respect to the sample stage was used. To minimize the effect of third-order harmonics, the Si (111) monochromator was detuned by 15% at the middle of the XAS scan region. Copper and zinc K-edge data were normalized, averaged, and fit to standard data using XAS viewer.[27]

At 20-ID-B, the Vortex Si Drift (four-element) detector was oriented 45° to the sample with a resolution of 2×2μm and incident energy of 10.5 keV. SR-μXRF maps were collected with a step size of 5μm. A reduction of the third harmonic of the Bragg peak was achieved from a 10% detuning of the Si (111) monochromator. SR-μXRF maps from human samples were analyzed and prepared with PyMCA.[28] *In vivo* copper and zinc K-edge μXANES spectra were collected on the human samples in regions of high elemental concentration revealed by the SR-μXRF maps. The Si (111) monochromator was calibrated using zinc foil. Copper K-edge μXANES and zinc K-edge μXANES were collected over an energy range from 8,830 to 9224eV and 9,511 to 10,406eV, respectively, with a spot size of 2×2μm on the sample provided by Kirkpatrick-Baez (KB) mirror focusing. A 13-element Ge detector was used situated at 45° with respect to the sample stage. To minimize the effect of third-order harmonics, the Si (111) monochromator was detuned by 15% at the middle of the XAS scan region. Copper and zinc K-edge data were normalized, averaged, and fit to standard data using XAS viewer.[27]

5.4. Results

5.4.1. SR-μXRF of Murine Joint Tissue

Elemental distribution maps of copper, zinc, and iron in the knee and hip joints of mice were collected using SR-μXRF. The overlay image of the three elements in the femoral head is seen in Figure 5.3., with Cu, Zn, and Fe distribution shown in green, red, and blue, respectively. Iron distribution is primarily in the middle of the femoral neck, the location of bone marrow. Distinct accumulation of Zn (red) is observed in the calcified tissue, with a faint Cu (green) signal also present. Most significant is the high accumulation of both Zn and Cu at the outer edge of the femoral head, with Cu on the outer edge. This Zn feature was previously observed in Chapter 3,

Figure 3.6. in both control and tungsten exposed mice. Roschger *et al.* previously demonstrated using SR-μXRF that Zn accumulates in the tidemark of articular cartilage in normal adult human joints.[16] If the zinc feature observed in Figure 5.3. is due to Zn accumulation in the tidemark, the Cu is likely accumulating in the non-calcified zones of articular cartilage. To determine the exact location of Zn and Cu accumulation, a larger sample is needed so that features are differentiable.
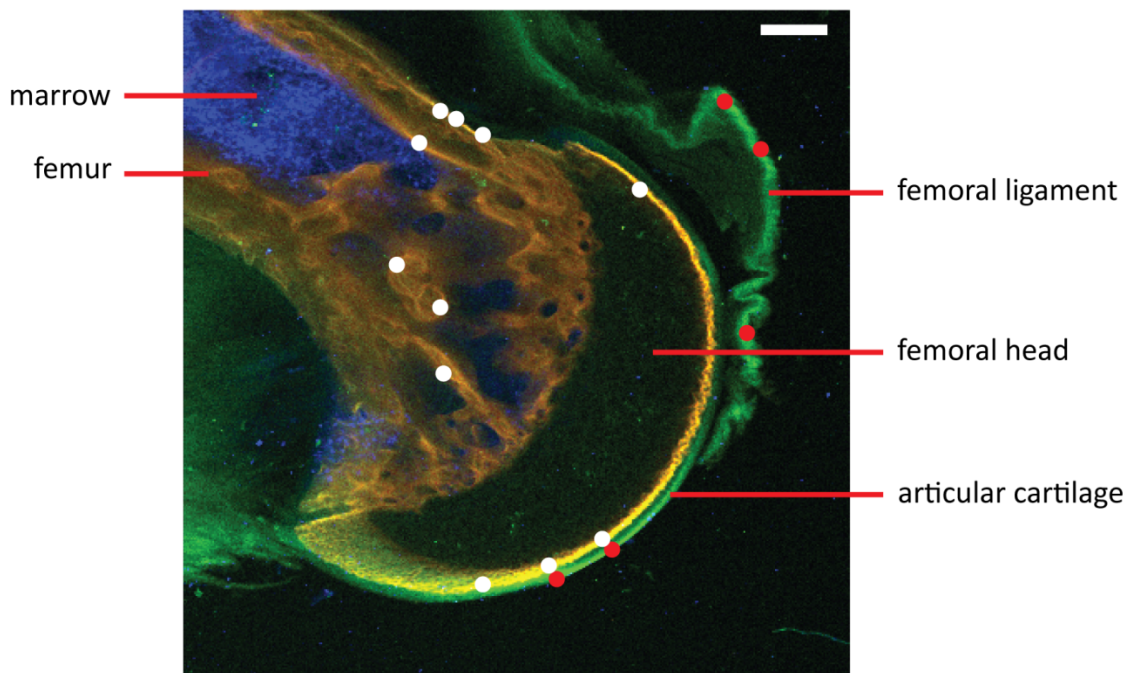

Figure 5.3. Copper (green), zinc (red), and iron (blue) distribution in femoral head. Locations of μXANES scans for copper and zinc are demonstrated by the red and white dots, respectively. Scale bar = 200 μm.

SR-μXRF elemental distribution maps were also measured in mouse knee tissue (Figure 5.4.). The sample sectioned in the lateral plane was treated with four weeks of 1000 ppm of tungsten, whereas the sample sectioned in the anterior plane was a control sample. Cu was found in the patellar and collateral ligaments in the knee and appears to be unaffected by exposure to tungsten. A faint Cu signal is also detected throughout the bone tissue. Zinc is present throughout the calcified bone tissue of the knee, in both the femur and tibia. Furthermore, an intense Zn signal is seen in the outer edge of the patella, in the same location as the tidemark for this tissue.[16]
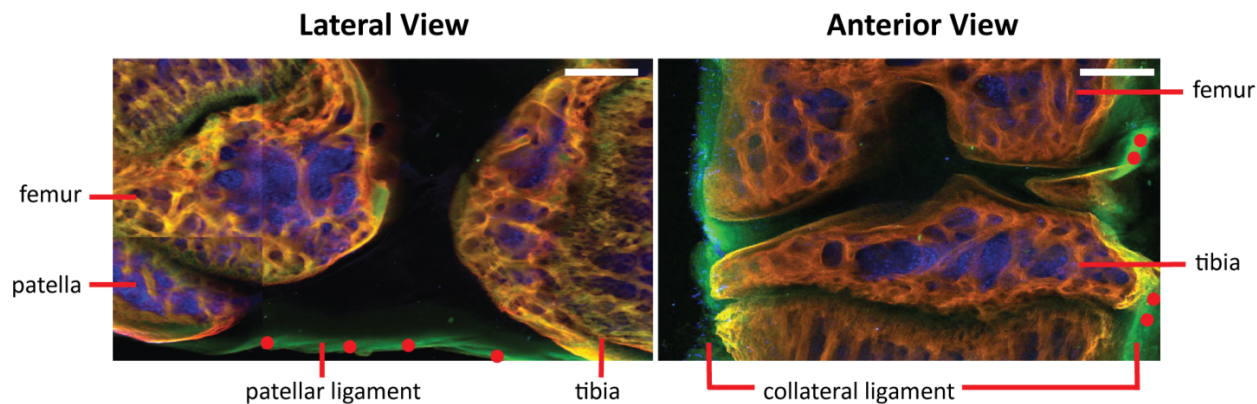
Figure 5.4. Copper (green), zinc (red), and iron (blue) distribution in knee from lateral and anterior views. Locations of Cu μXANES scans indicated by red dots. Scale bar = 500 μm.

5.4.2. SR-μXRF of Human Femoral Head

To differentiate between Zn and Cu features in the articular cartilage of the femoral head, SR-μXRF elemental distribution was measured in a human femoral head sample. Samples taken from human tissue have significantly larger features than mouse tissue, allowing for the differentiation between bone, tidemark, and cartilage. In mouse tissue, the tidemark feature is small, preventing imaging of these finer features. Two samples were measured with SR-μXRF: one with articular cartilage in normal condition and one where the articular cartilage is degenerated due to OA. Samples were obtained from femoral hips removed during hip replacement surgery. OA is a disease characterized by joint pain and loss of mobility which can result in joint failure.[26] In OA cartilage, progression of the disease leads to surface fissures, collagen fiber fibrillation, and cell cluster formation ultimately leading to degeneration of the cartilage. Degeneration of the articular cartilage in the OA sample versus the normal sample is clearly observed in the microscope image (Figure 5.5.).

Figure 5.5. clearly shows specific accumulation of zinc (red) in the tidemark between calcified tissue (blue) and non-calcified cartilage. Zinc is also found in the calcified tissue beneath the tidemark. Copper (green) is found throughout the entirety of the articular cartilage, with slightly higher accumulation at the articular surface into the superficial zone. This distribution is similar to that observed in mouse tissue (Figure 5.3.). The specific copper localization at the articular surface in the normal tissue is lost in the OA sample, likely due to degeneration of the articular cartilage.
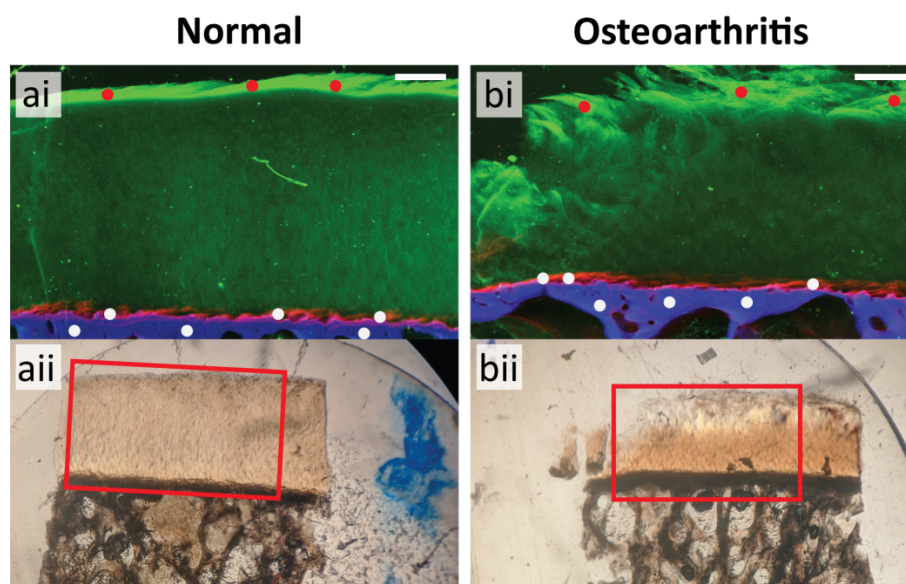
Figure 5.5 Copper (green), zinc (red), and calcium (blue) distribution in human femoral head with (a) normal and (b) degenerated cartilage due to OA. Sections visualized with SR-μXRF (i) are indicated by the red squares in the microscope images (ii). Locations of Cu and Zn μXANES scans indicated by the red and white dots, respectively. Scale bar = 500 μm.

5.4.3. Copper μXANES

Copper K-edge μXANES spectra was collected at areas of high copper accumulation in mouse and human samples, as indicated in Figures 5.3 – 5.5. XAS data of individual spots across the samples were merged, resulting in the spectra seen in Figure 5.6. In the mouse femoral head, Figure 5.6.a, the Cu μXANES spectra was weak and noisy, likely from low concentrations. The signals were stronger in the mouse anterior and lateral knee sections, with the best signal from the human samples. Because the human samples have larger Zn and Cu features, it easier to obtain good signal for μXANES. A sharp pre-edge peak at 8982 eV in the copper XAS spectra was observed across all samples. All the spectra have good overlap, indicating that the copper present in the knee ligaments and articular cartilage in femoral head are in the same oxidation state and have very similar local environments. No difference is seen between normal and OA articular cartilage. Cu K-edge μXANES spectra of the human femoral head sample and copper standards are compared in Figure 5.7. Though the fit is imperfect, it is clear that copper(I) oxide best fits the sample spectra. The pre-edge peak at 8982 eV is particularly characteristic of Cu(I) oxide species.[29] This peak is present in Cu(I) species due to the Cu $1s \rightarrow 4p$ transition and sensitive to the coordination environment of the Cu(I) center.[30]
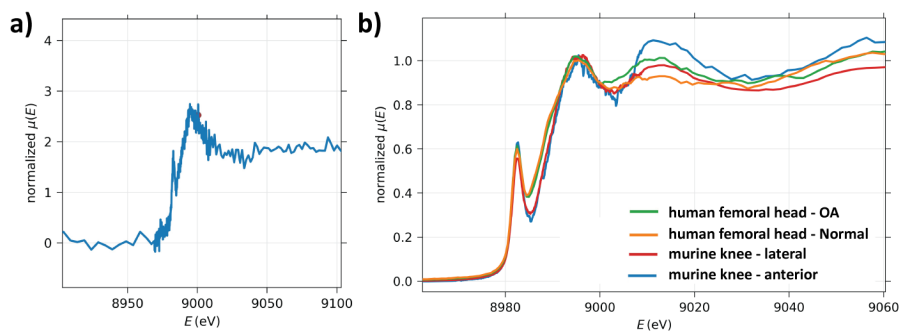
107

Figure 5.6. Cu K-edge XAS in (a) murine femoral head and (b) murine knee and human femoral head.
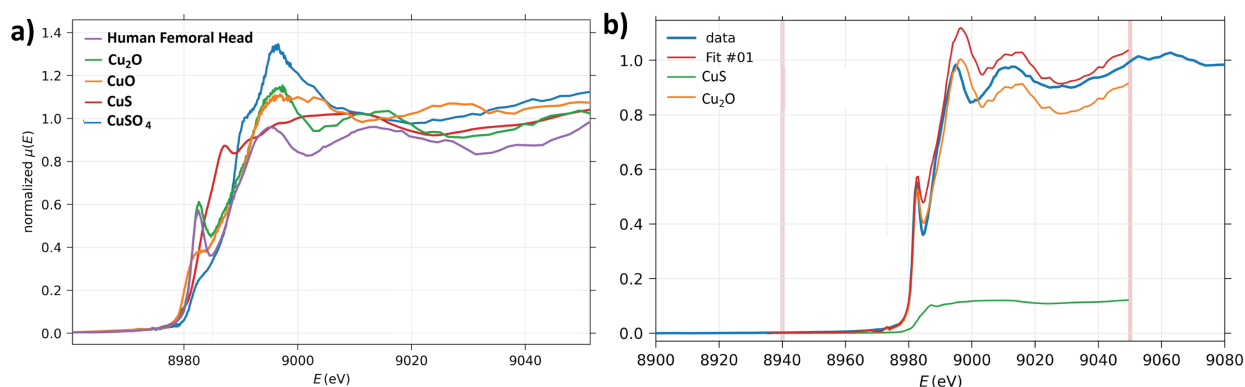

Figure 5.7. (a) Comparison of Cu K-edge XANES spectra of human femoral head (orange) and copper standards: copper(I) oxide (Cu_2O, green), copper(II) oxide (CuO, orange), and copper(I) monosulfide (CuS, red), copper(II) sulfate ($CuSO_4$, blue). (b) Cu K-edge XANES spectra of sample fit with standards.

5.4.4. Zinc μXANES

Zn K-edge μXANES data was measured in the mouse and human femoral head at the tidemark and in various locations in the calcified tissue to determine if there were any differences in the Zn local environment in these regions (Figure 5.8). For each spectrum, data is merged across all measured locations indicated in Figure 5.3. and 5.5. Spectra shapes were identical across the normal and OA human femoral head samples and, thus, these were merged as well. The shape of all spectra are very similar with an identical rising edge, indicating the similarity of zinc local environment and charge. However, Figure 5.8.b shows that the main edge peak at 9665-9670 eV changes in shape, suggesting differences in zinc coordination or even differing contributions from more than one zinc binding site. Overall, the Zn XAS spectra measured in mouse samples are less intense and more noisy, likely due to the smaller Zn feature and subsequently smaller quantity of zinc in these samples.
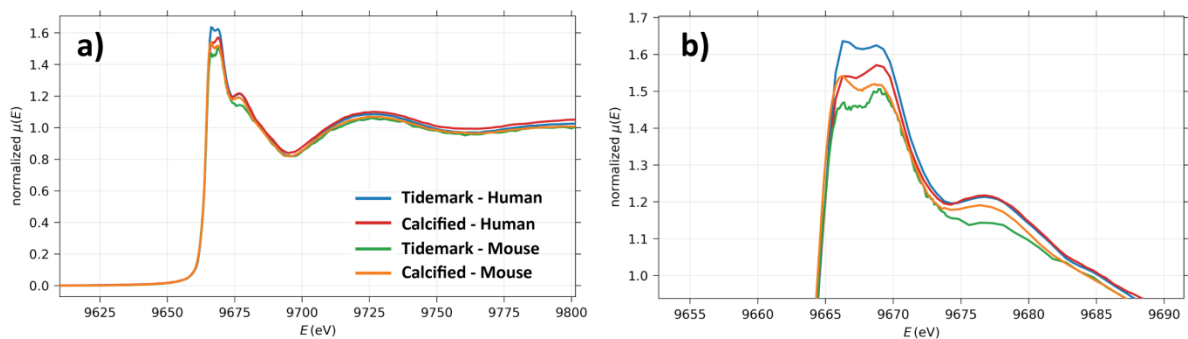
Figure 5.8. (a) Zn K-edge μXANES of tidemark and calcified tissue in human and mouse femoral head tissue. (b) Magnified image of main edge peak.
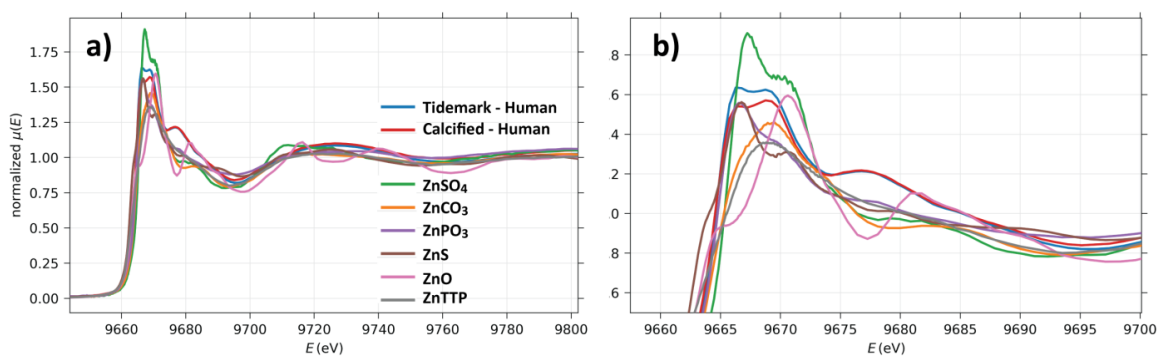

Figure 5.9. (a) Comparison of Zn K-edge μXANES of tidemark and calcified tissue in human femoral head tissue with zinc standards. (b) Magnified image of main edge peak.
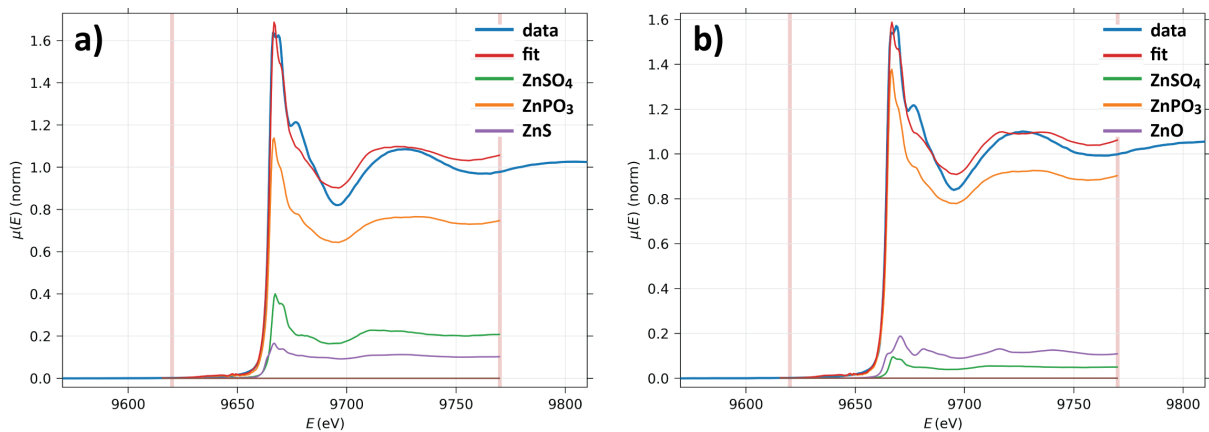

Figure 5.10. (a) Zn K-edge μXANES fit of (a) tidemark and (b) calcified tissue in human femoral head with zinc standards.

When comparing Zn K-edge μXANES spectra of human tidemark and calcified tissue to zinc standards, Figure 5.9., it is easy to see that no standard is a good fit for the sample data. In

particular, the shoulder in the sample data at 9677 eV is not replicated by any of the standards and is not fit adequately by any of the zinc standards used (Figure 5.10.)

5.5. Discussion

5.5.1. Copper

Significant amounts of copper were found in the articular cartilage of human and mouse femoral heads, as well as in the ligaments surrounding the mouse knee joint. A faint copper signal was also detected in the femur and tibia bone. Cu K-edge µXANES spectra are remarkably similar at all measured locations, Figure 5.6., suggesting that copper exists in similar environments. Cartilage and ligament tissue are composed primarily of collagen, with smaller amounts of collagen present in calcified bone tissue as well. LOX is a well-known copper containing enzyme responsible for collagen cross-linking and is a likely candidate for the observed copper accumulation.

Supporting the hypothesis that the observed copper accumulation is due to the presence of LOX is higher accumulation of Cu at the articular surface and superficial zone of normal human tissue (Figure 5.5.). This zone of articular cartilage contains denser, more organized collagen and it is reasonable to expect a high accumulation of LOX. In joints effected by OA, articular cartilage is stiffened due the up-regulation of LOX and increased collagen cross-linking.[31, 32] The amount of collagen type II also decreases during the progression of OA. Miosge *et al.* demonstrated that collagen type I is produced by OA cartilage and especially expressed in the fibrocartilaginous tissue of the later stages of the disease progress.[33] Up-regulation of LOX and the formation of fibril collagen type 1 may lead to the larger diffuse copper feature observed throughout the articular cartilage in the OA sample. Furthermore, in mouse tissue a stronger Cu K-edge µXANES signal was obtained from knee ligament, versus femoral head, articular cartilage. Ligament contains primarily collagen type I, the strongest type of collagen due to its extensive cross-linking. More LOX would be expected, therefore, in ligament versus articular cartilage, giving rise to a higher concentration of copper and an improved Cu K-edge µXANES signal.
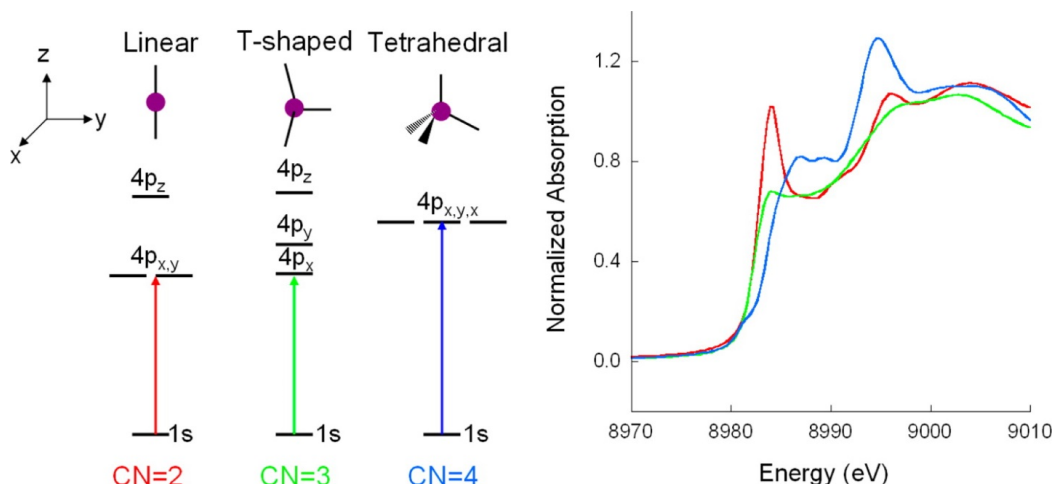
Figure 5.11. (Left) Ligand field splitting of Cu(I) 4p orbitals as a function of the site geometry. (Right) K-edge XAS spectra of two-coordinate Cu(I), $[Cu_2(EDTB)](ClO_4)_2$ with 2N ligands (red), three-coordinate Cu(I), $[Cu(L1-pr)](BF_4)$ with 1S, 2N ligands (green), and four-coordinate Cu(I), $[Cu(py)_4]ClO_4$ with 4N ligands (blue). Reprinted from ref.[1] Copyright 2005 American Chemical Society.

More indicative than µXRF mapping of copper in bone tissues, is the structural information revealed by Cu K-edge µXANES measurements on the local copper deposits. As described by Solomon *et al.* and shown in Figure 5.11., a pre-edge feature at ~8984 eV in the Cu K-edge XAS spectra is extremely characteristic of a Cu(I) species.[1] Furthermore, the shape of the XANES region defines the coordination environment of the Cu(I) site and the intensity of the pre-edge peak and can be used to quantify the amount of reduced copper in a metalloprotein sample. The shape of Cu K-edge XANES spectra in bone, Figure 5.6., indicates that copper in these sites is most likely a three-coordinate Cu(I) species. The implications of these findings require a brief, but in depth, discussion of what is known about copper in not only the active site of LOX, but of copper amine oxidases in general.
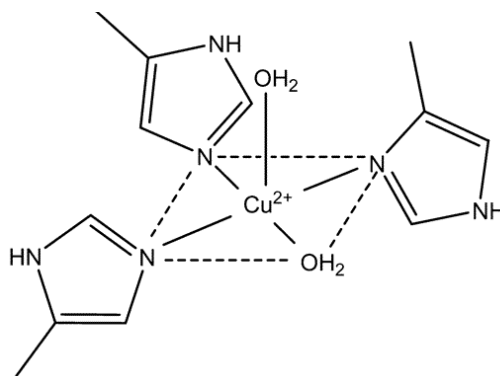

Figure 5.12. Cu(II) site in amine oxidases. Reprinted with permission from Bollinger *et al.*[6] Copyright (2015) American Chemical Society.

LOX is a copper amine oxidase which catalyzes the oxidative deamination of lysyl residues in collagen and elastin, allowing for the formation of the cross-links essential for the structure of these proteins.[34] Copper amine oxidases contain a tightly bound Cu(II) ion and cofactor 2,4,5-tryhydroxyphenethylamine quinone (TPQ) at the active site. The model for the Cu(II) active site in amine oxidases (Figure 5.12.) is supported by several spectroscopic studies including XAS, ENDOR and EPR.[35, 36] While rapid freeze-quench EPR experiments appear to rule out the possibility of copper reduction during the catalytic cycle,[37] other studies report that Cu(II) can be reduced by the addition of substrate amine under anaerobic conditions.[38, 39] The difference in these results is attributed to the temperature under which the EPR spectra is obtained; at room temperature a significant change is observed in the EPR spectra.[35] This is due to Cu(II) being favored under low temperatures, thus, the Cu(I)-semiquinone state was not observed during the rapid-freeze quenched conditions of the previous experiment. These results suggest that copper has a redox function in amine oxidases, with a proposed catalytic cycle shown in Figure 5.13.[40] Kinetic and computation studies also indicate that a redox-active metal in copper amine oxidases is required to catalyze the reduction of O_2 to H_2O_2.[41] Currently, it is not known whether molecular oxygen reacts with Cu(I) bound to TPQ, TPQ semiquinone, or Cu(I) as there is evidence for each option.[42-44]
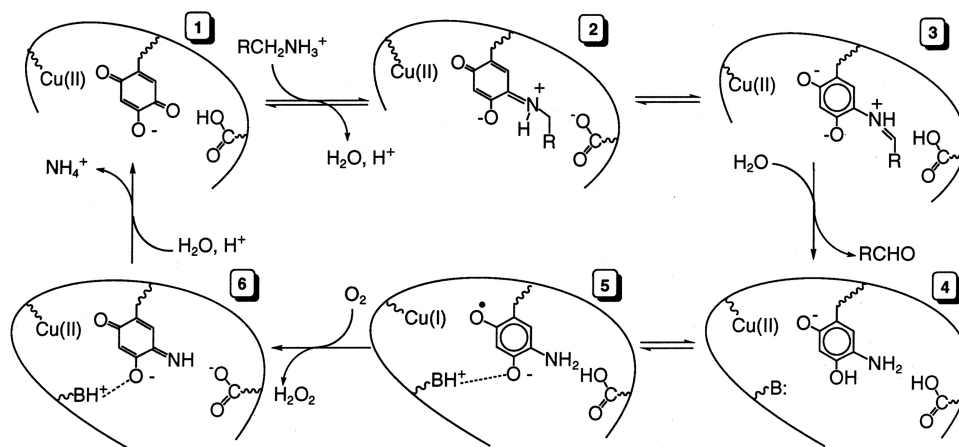

Figure 5.13. Mechanism of substrate amine oxidation. Reprinted with permission.[40] Copyright 1998 American Chemical Society.

Thus far, the proposed catalytic cycle for copper amine oxidases has not been extended to LOX. EPR characterization of *Drosophilia* LOX, a model for human LOX, demonstrates that Cu(II) is the active form of copper in the LOX active site, with structure similar to that of Cu(II)

sites in other amine oxidases (Figure 5.13.).[6, 45, 46] However, LOX differs from other copper amine oxidases because lysine tyrosylquinone (LTQ) rather than TPQ is the redox cofactor.[34] Furthermore, as a monomer of 32 kDA, LOX is smaller than other copper amine oxidases (dimers of 75-85 kDa subunits).[47] In the proposed LOX catalytic mechanism, LTQ is the sole electron sink, without reduction of the Cu(II) cofactor.[48]

Our results indicate the presence of a Cu(I) species in bone, in locations with high concentrations of organized collagen, and likely LOX. When compared to the Cu K-edge XAS spectra of Cu(I) forms of amine oxidases, Figure 5.14., significant similarities are seen including the shape of the curve and pre-edge feature.[40] Cu(I) amine oxidase were determined to be three-coordinate, similar to the Cu(I) species in bone.
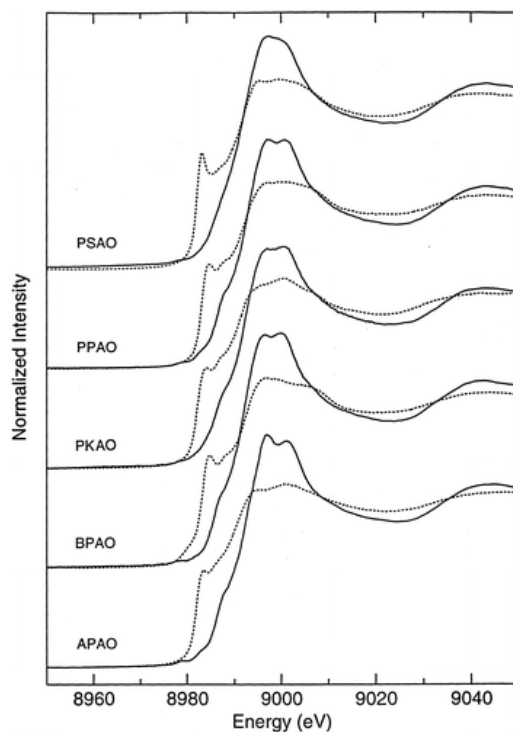

Figure 5.14. Copper K-edge X-ray absorption spectra of five amine oxidases: (-) oxidized forms and (- - -) dithionite-reduced forms. Reprinted with permission.[40] Copyright 1998 American Chemical Society.

Ultimately, these results present us with an interesting puzzle. While it is clear that Cu(I) species are detected in bone, more experiments are needed to determine whether this is due to a reduced form of LOX, another copper complex altogether, or even photoreduction in the X-ray beam. While Cu(I) has not been specifically detected in LOX, the necessity of Cu(I) in the catalytic mechanism of other copper amine oxidases certainly supports this as a possibility.

5.5.2. Zinc

Zinc was found with a heterogeneous distribution in bone tissue, similar to results from Chapter 2-4. In addition, a highly localized zinc deposit was found in the tidemark of articular cartilage in mouse and human femoral head samples. Zn K-edge XANES spectra in bone and the tidemark were essentially identical, with slight changes at the main edge (Figure 5.8.). All spectra exhibit a peak doublet for the main edge between 9665-9670 eV and a shoulder peak at ~ 9677 eV. XANES spectra are very sensitive to changes in the local environment and thus the similarity between the XANES spectra for zinc in calcified tissue and in the tidemark suggest a similar Zn coordination environment. The features in biological samples are very different when compared to the reference standards, Figure 5.9. Conducting linear combination fits using combinations of the model compounds did not yield a reasonable fit (Figure 5.10.) indicating that the Zn K-edge XAS spectra in bone is not due to presence of any of the tested inorganic Zn standards.
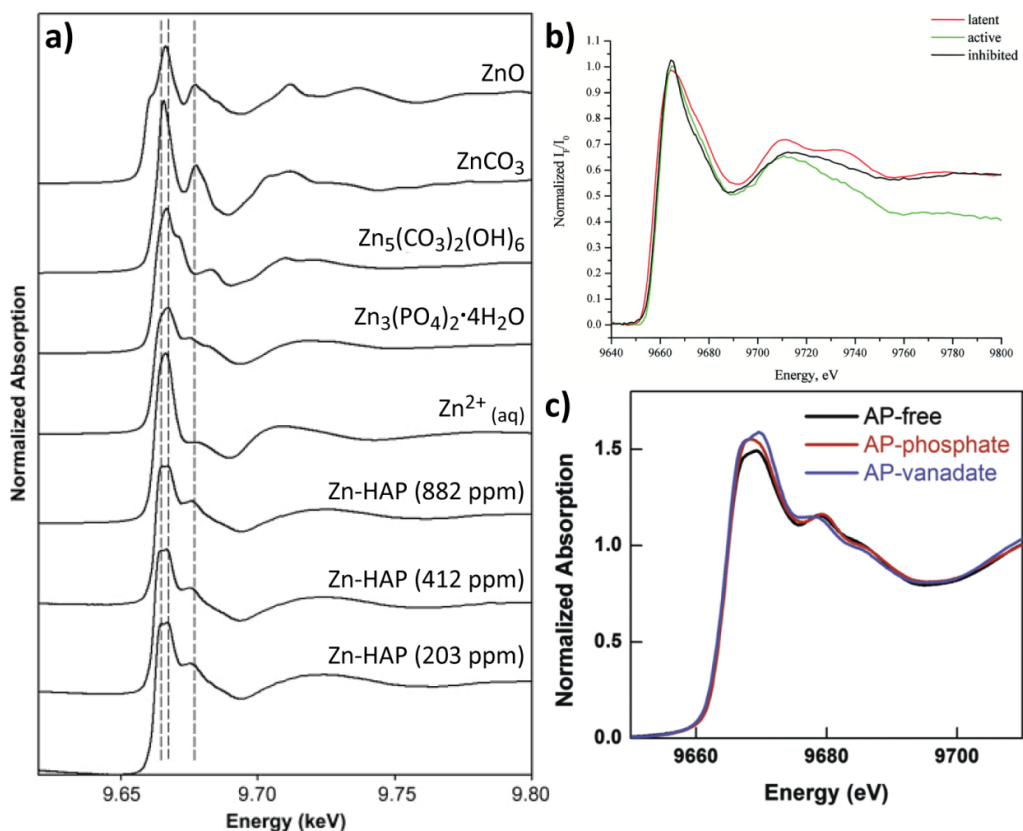

Figure 5.15. Zn K-edge XAS spectra (a) Zn-doped HAP and standards, (b) MMP, and (c) ALP. (a) Normalized Zn K-edge XANES spectra of Zn model compounds and three Zn doped HAP samples. Used with permission.[49] (b) Normalized raw XAS data in the zinc K-edge region of pro-MMP2 (red), active (green), and MMP-2-SB-3CT complex (black).[50] (c) Zn K-edge XAS data for ALP: free proteins (black), phosphoryl-group-bound (red), vanadate-bound (blue). Reused with permission.[51]

Figure 5.15. shows the Zn K-edge XANES spectra of MMP, ALP and Zn incorporated in hydroxyapatite (HAP).[49-51] Interestingly, both Zn-HAP and ALP have broad main edges, similar to the double peak feature seen in the bone samples. Furthermore, both compounds exhibit a shoulder feature at ~9677 eV. MMP, on the other hand, has a sharp main edge peak and no obvious shoulder feature. This indicates that the zinc signal observed in bone and articular cartilage could be due to ALP, incorporation into HAP, or a combination of both.

It is certainly possible that the observed zinc deposits in bone are due to a combination of ALP and incorporation into apatite. ALP and Zn have been shown to localize in the tidemark in separate experiments.[16, 26] However, zinc association with HAP has also been demonstrated and investigated in several experiments.[49, 52-54] Dessombz *et al*. investigated zinc deposits in cartilage and meniscus calcifications using μXRF and μXAS and found the presence of at least two zinc species.[55] They hypothesized that one may correspond to Zn embedded in a metalloprotein and the second to Zn at the surface or in biological apatite. More work is needed to precisely define the nature of the zinc deposits present in bone and the tidemark. Future experiments could include direct comparison of Zn K-edge XAS spectra of ALP and Zn-HAP standards as well as computation modelling to gain more insight into the system.

5.6. Conclusions

Copper and zinc distribution in the hip and knee joints was mapped using SR-μXRF. The strongest Cu signal was found in tissues with high collagen content: ligament and articular cartilage. Cu K-edge XAS spectra did not differ significantly across the tissue, indicating the similarity of the copper environment across the sample. More significantly, the pre-edge feature at ~8984 eV clearly demonstrates that the copper species in the bone exists in its reduced form, Cu(I). Further experiments are required to determine if this Cu(I) species is the first evidence of a reduced copper form of LOX or is from a different copper complex altogether.

Zinc was found in calcified tissue and the tidemark of articular cartilage. Like copper, the Zn K-edge XAS spectra did not differ significantly across the tissue. The Zn K-edge XANES spectra contained a shoulder peak at ~ 9677 eV, which was not matched by any of the measured zinc standard compounds. However, XANES spectra of ALP and Zn-doped HAP reported in the literature do contain this distinctive feature. Further work is required to determine whether the

115

observed Zn accumulation in bone and the tidemark is due to either ALP, incorporation into the bone matrix, or a combination of both.

5.7. References

1.   Solomon, E. I.; Heppner, D. E.; Johnston, E. M.; Ginsbach, J. W.; Cirera, J.; Qayyum, M.; Kieber-Emmons, M. T.; Kjaergaard, C. H.; Hadt, R. G.; Tian, L. Copper Active Sites in Biology. *Chemical Reviews* **2014,** *114* (7), 3659-3853.

2.   McCall, K. A.; Huang, C.-c.; Fierke, C. A. Function and Mechanism of Zinc Metalloenzymes. *The Journal of Nutrition* **2000,** *130* (5), 1437S-1446S.

3.   Vallee, B. L.; Auld, D. S. Zinc Coordination, Function, and Structure of Zinc Enzymes and Other Proteins. *Biochemistry* **1990,** *29* (24), 5647-5659.

4.   Dollwet, H. H. A.; Sorenson, J. R. J. Roles of Copper in Bone Maintenance and Healing. *Biological Trace Element Research* **1988,** *18* (1), 39-48.

5.   Yamaguchi, M. Role of Zinc in Bone Formation and Bone Resorption. *The Journal of Trace Elements in Experimental Medicine* **1998,** *11* (2-3), 119-135.

6.   Bollinger, J. A.; Brown, D. E.; Dooley, D. M. The Formation of Lysine Tyrosylquinone (Ltq) Is a Self-Processing Reaction. Expression and Characterization of a Drosophila Lysyl Oxidase. *Biochemistry* **2005,** *44* (35), 11708-11714.

7.   Lin, W.; Xu, L.; Li, G. Molecular Insights into Lysyl Oxidases in Cartilage Regeneration and Rejuvenation. *Frontiers in Bioengineering and Biotechnology* **2020,** *8* (359).

8.   Herchenhan, A.; Uhlenbrock, F.; Eliasson, P.; Weis, M.; Eyre, D.; Kadler, K. E.; Magnusson, S. P.; Kjaer, M. Lysyl Oxidase Activity Is Required for Ordered Collagen Fibrillogenesis by Tendon Cells. *The Journal of biological chemistry* **2015,** *290* (26), 16440-16450.

9.   Cai, L.; Xiong, X.; Kong, X.; Xie, J. The Role of the Lysyl Oxidases in Tissue Repair and Remodeling: A Concise Review. *Tissue Engineering and Regenerative Medicine* **2017,** *14* (1), 15-30.

10.   Poole, A. R. An Introduction to the Pathophysiology of Osteoarthritis. *Front Biosci* **1999,** *4*, D662-70.

11.   Luo, Y.; Sinkeviciute, D.; He, Y.; Karsdal, M.; Henrotin, Y.; Mobasheri, A.; Önnerfjord, P.; Bay-Jensen, A. The Minor Collagens in Articular Cartilage. *Protein & Cell* **2017,** *8* (8), 560-572.

12.   Bella, J.; Hulmes, D. J. S., Fibrillar Collagens. In *Fibrous Proteins: Structures and Mechanisms*, Parry, D. A. D.; Squire, J. M., Eds. Springer International Publishing: Cham, 2017; pp 457-490.

13.   Sophia Fox, A. J.; Bedi, A.; Rodeo, S. A. The Basic Science of Articular Cartilage: Structure, Composition, and Function. *Sports health* **2009,** *1* (6), 461-468.

14.   Nimni, M. E., *Collagen. Volume 1, Biochemistry*. CRC Press: Boca Raton, FL, 2018.

15.   Buckwalter, J. A.; Mow, V. C.; Ratcliffe, A. Restoration of Injured or Degenerated Articular Cartilage. *JAAOS - Journal of the American Academy of Orthopaedic Surgeons* **1994,** *2* (4).

16.   Roschger, A.; Hofstaetter, J. G.; Pemmer, B.; Zoeger, N.; Wobrauschek, P.; Falkenberg, G.; Simon, R.; Berzlanovich, A.; Thaler, H. W.; Roschger, P.; Klaushofer, K.; Streli, C. Differential Accumulation of Lead and Zinc in Double-Tidemarks of Articular Cartilage. *Osteoarthritis and Cartilage* **2013,** *21* (11), 1707-1715.

17.   Pemmer, B.; Roschger, A.; Wastl, A.; Hofstaetter, J. G.; Wobrauschek, P.; Simon, R.; Thaler, H. W.; Roschger, P.; Klaushofer, K.; Streli, C. Spatial Distribution of the Trace Elements Zinc, Strontium and Lead in Human Bone Tissue. *Bone* **2013,** *57* (1), 184-193.

18.   Haumont, S. Distribution of Zinc in Bone Tissue. *Journal of Histochemistry & Cytochemistry* **1961,** *9* (2), 141-145.

19.   Krane, S. M.; Inada, M. Matrix Metalloproteinases and Bone. *Bone* **2008,** *43* (1), 7-18.

20.   Sharma, U.; Pal, D.; Prasad, R. Alkaline Phosphatase: An Overview. *Indian journal of clinical biochemistry : IJCB* **2014,** *29* (3), 269-278.

21.   Szulc, P.; Bauer, D. C., Biochemical Markers of Bone Turnover in Osteoporosis. In *Osteoporosis (Fourth Edition)*, Marcus, R.; Feldman, D.; Dempster, D. W.; Luckey, M.; Cauley, J. A., Eds. Academic Press: San Diego, 2013; pp 1573-1610.

22.   Golub, E. E.; Boesze-Battaglia, K. The Role of Alkaline Phosphatase in Mineralization. *Current Opinion in Orthopaedics* **2007,** *18* (5).

23.   Miao, D.; Scutt, A. Histochemical Localization of Alkaline Phosphatase Activity in Decalcified Bone and Cartilage. *Journal of Histochemistry & Cytochemistry* **2002,** *50* (3), 333-340.

24.   Kuo, T.-R.; Chen, C.-H. Bone Biomarker for the Clinical Assessment of Osteoporosis: Recent Developments and Future Perspectives. *Biomarker Research* **2017,** *5* (1), 18.

25.   Revell, P. A.; Pirie, C.; Amir, G.; Rashad, S.; Walker, F. Metabolic Activity in the Calcified Zone of Cartilage: Observations on Tetracycline Labelled Articular Cartilage in Human Osteoarthritic Hips. *Rheumatology International* **1990,** *10* (4), 143-147.

26. Black, C. S.; Crepeau, P. K.; Sheffield, I. D.; Macdonald, J. R.; Wootton, D. J.; Baek, M.; Eggett, D. L.; Reynolds, P. R.; Kooyman, D. L. Identification of the Tidemark Line of Calcification in Osteoarthritic Cartilage Using a Stain for Alkaline Phosphatase. *Osteoarthritis and Cartilage* **2015,** *23*, A139.

27. Newville, M. Larch: An Analysis Package for Xafs and Related Spectroscopies. *Journal of Physics: Conference Series* **2013,** *430*, 012007.

28. Solé, V. A.; Papillon, E.; Cotte, M.; Walter, P.; Susini, J. A Multiplatform Code for the Analysis of Energy-Dispersive X-Ray Fluorescence Spectra. *Spectrochimica Acta Part B: Atomic Spectroscopy* **2007,** *62* (1), 63-68.

29. Gaur, A.; Shrivastava, B. D.; Joshi, S. K. Copper K-Edge Xanes of Cu(I) and Cu(Ii) Oxide Mixtures. *Journal of Physics: Conference Series* **2009,** *190*, 012084.

30. Kau, L. S.; Spira-Solomon, D. J.; Penner-Hahn, J. E.; Hodgson, K. O.; Solomon, E. I. X-Ray Absorption Edge Determination of the Oxidation State and Coordination Number of Copper. Application to the Type 3 Site in Rhus Vernicifera Laccase and Its Reaction with Oxygen. *Journal of the American Chemical Society* **1987,** *109* (21), 6433-6442.

31. Kim, J.-H.; Lee, G.; Won, Y.; Lee, M.; Kwak, J.-S.; Chun, C.-H.; Chun, J.-S. Matrix Cross-Linking–Mediated Mechanotransduction Promotes Posttraumatic Osteoarthritis. *Proceedings of the National Academy of Sciences* **2015,** *112* (30), 9424.

32. Alshenibr, W.; Tashkandi, M. M.; Alsaqer, S. F.; Alkheriji, Y.; Wise, A.; Fulzele, S.; Mehra, P.; Goldring, M. B.; Gerstenfeld, L. C.; Bais, M. V. Anabolic Role of Lysyl Oxidase Like-2 in Cartilage of Knee and Temporomandibular Joints with Osteoarthritis. *Arthritis research & therapy* **2017,** *19* (1), 179-179.

33. Miosge, N.; Hartmann, M.; Maelicke, C.; Herken, R. Expression of Collagen Type i and Type ii in Consecutive Stages of Human Osteoarthritis. *Histochemistry and Cell Biology* **2004,** *122* (3), 229-236.

34. Floris, G.; Finazzi Agrò, A., Amine Oxidases. In *Encyclopedia of Biological Chemistry (Second Edition)*, Lennarz, W. J.; Lane, M. D., Eds. Academic Press: Waltham, 2013; pp 87-90.

35. Dooley, D. M.; Brown, D. E.; Clague, A. W.; Kemsley, J. N.; McCahon, C. D.; McGuirl, M. A.; Turowski, P. N.; McIntire, W. S.; Farrar, J. A.; Thomson, A. J., Structure and Reactivity of Copper-Containing Amine Oxidases. In *Bioinorganic Chemistry of Copper*, Karlin, K. D.; Tyeklár, Z., Eds. Springer Netherlands: Dordrecht, 1993; pp 459-470.

36. Scott, R. A.; Dooley, D. M. X-Ray Absorption Spectroscopic Studies of the Copper(Ii) Sites in Bovine Plasma Amine Oxidase. *Journal of the American Chemical Society* **1985,** *107* (14), 4348-4350.

37.   Grant, J.; Kelly, I.; Knowles, P.; Olsson, J.; Pettersson, G. Changes in the Copper Centres of Benzylamine Oxidase from Pig Plasma During the Catalytic Cycle. *Biochemical and Biophysical Research Communications* **1978,** *83* (3), 1216-1224.

38.   Turowski, P. N.; McGuirl, M. A.; Dooley, D. M. Intramolecular Electron Transfer Rate between Active-Site Copper and Topa Quinone in Pea Seedling Amine Oxidase. *The Journal of biological chemistry* **1993,** *268* (24), 17680-2.

39.   Dooley, D. M.; McGuirl, M. A.; Brown, D. E.; Turowski, P. N.; McLntire, W. S.; Knowles, P. F. A Cu(I)-Semiquinone State in Substrate-Reduced Amine Oxidases. *Nature* **1991,** *349* (6306), 262-264.

40.   Dooley, D. M.; Scott, R. A.; Knowles, P. F.; Colangelo, C. M.; McGuirl, M. A.; Brown, D. E. Structures of the Cu(I) and Cu(Ii) Forms of Amine Oxidases from X-Ray Absorption Spectroscopy. *Journal of the American Chemical Society* **1998,** *120* (11), 2599-2605.

41.   Liu, Y.; Mukherjee, A.; Nahumi, N.; Ozbil, M.; Brown, D.; Angeles-Boza, A. M.; Dooley, D. M.; Prabhakar, R.; Roth, J. P. Experimental and Computational Evidence of Metal-O2 Activation and Rate-Limiting Proton-Coupled Electron Transfer in a Copper Amine Oxidase. *The Journal of Physical Chemistry B* **2013,** *117* (1), 218-229.

42.   Vakal, S.; Jalkanen, S.; Dahlström, K. M.; Salminen, T. A. Human Copper-Containing Amine Oxidases in Drug Design and Development. *Molecules* **2020,** *25* (6).

43.   Shepard, E. M.; Dooley, D. M. Inhibition and Oxygen Activation in Copper Amine Oxidases. *Accounts of Chemical Research* **2015,** *48* (5), 1218-1226.

44.   Shepard, E. M.; Okonski, K. M.; Dooley, D. M. Kinetics and Spectroscopic Evidence That the Cu(I)−Semiquinone Intermediate Reduces Molecular Oxygen in the Oxidative Half-Reaction of Arthrobacter Globiformis Amine Oxidase. *Biochemistry* **2008,** *47* (52), 13907-13920.

45.   Rao, G.; Bansal, S.; Law, W. X.; O'Dowd, B.; Dikanov, S. A.; Oldfield, E. Pulsed Electron Paramagnetic Resonance Insights into the Ligand Environment of Copper in Drosophila Lysyl Oxidase. *Biochemistry* **2017,** *56* (29), 3770-3779.

46.   Gacheru, S. N.; Trackman, P. C.; Shah, M. A.; O'Gara, C. Y.; Spacciapoli, P.; Greenaway, F. T.; Kagan, H. M. Structural and Catalytic Properties of Copper in Lysyl Oxidase. *Journal of Biological Chemistry* **1990,** *265* (31), 19022-19027.

47.   Messerschmidt, A., Copper Metalloenzymes. In *Comprehensive Natural Products Ii*, Liu, H.-W.; Mander, L., Eds. Elsevier: Oxford, 2010; pp 489-545.

48.   Lucero, H. A.; Kagan, H. M. Lysyl Oxidase: An Oxidative Enzyme and Effector of Cell Function. *Cellular and Molecular Life Sciences CMLS* **2006,** *63* (19), 2304-2316.

49.   Tang, Y.; Chappell, H. F.; Dove, M. T.; Reeder, R. J.; Lee, Y. J. Zinc Incorporation into Hydroxylapatite. *Biomaterials* **2009,** *30* (15), 2864-2872.

50.   Kleifeld, O.; Kotra, L. P.; Gervasi, D. C.; Brown, S.; Bernardo, M. M.; Fridman, R.; Mobashery, S.; Sagi, I. X-Ray Absorption Studies of Human Matrix Metalloproteinase-2 (Mmp-2) Bound to a Highly Selective Mechanism-Based Inhibitor: Comparision with the Latent and Active Forms of the Enzyme. *Journal of Biological Chemistry* **2001,** *276* (20), 17125-17131.

51.   Bobyr, E.; Lassila, J. K.; Wiersma-Koch, H. I.; Fenn, T. D.; Lee, J. J.; Nikolic-Hughes, I.; Hodgson, K. O.; Rees, D. C.; Hedman, B.; Herschlag, D. High-Resolution Analysis of Zn2+ Coordination in the Alkaline Phosphatase Superfamily by Exafs and X-Ray Crystallography. *Journal of Molecular Biology* **2012,** *415* (1), 102-117.

52.   Matsunaga, K.; Murata, H.; Mizoguchi, T.; Nakahira, A. Mechanism of Incorporation of Zinc into Hydroxyapatite. *Acta Biomaterialia* **2010,** *6* (6), 2289-2293.

53.   Lee, Y. J.; Elzinga, E. J.; Reeder, R. J. Sorption Mechanisms of Zinc on Hydroxyapatite: Systematic Uptake Studies and Exafs Spectroscopy Analysis. *Environmental Science & Technology* **2005,** *39* (11), 4042-4048.

54.   Takatsuka, T.; Hirano, J.; Matsumoto, H.; Honma, T. X-Ray Absorption Fine Structure Analysis of the Local Environment of Zinc in Dentine Treated with Zinc Compounds. *European Journal of Oral Sciences* **2005,** *113* (2), 180-183.

55.   Dessombz, A.; Nguyen, C.; Ea, H.-K.; Rouzière, S.; Foy, E.; Hannouche, D.; Réguer, S.; Picca, F.-E.; Thiaudière, D.; Lioté, F.; Daudon, M.; Bazin, D. Combining Mx-Ray Fluorescence, Mxanes and Mxrd to Shed Light on Zn2+ Cations in Cartilage and Meniscus Calcifications. *Journal of Trace Elements in Medicine and Biology* **2013,** *27* (4), 326-333.

Chapter 6. Conclusions, Contributions to Knowledge, and Suggestions for Future Work

6.1. Conclusions and Contributions

In this thesis, we describe an *in situ* method for investigating metal distribution and speciation in bone. This method was applied to the investigation of tungsten but can be extended to other metal systems of interest. Since tungsten is an emerging contaminant recently found to accumulate in bone, accurately determining its distribution and speciation *in situ* is essential for directing toxicological studies and informing treatment regimes.

Using synchrotron radiation micro X-ray fluorescence (SR-μXRF), we found heterogeneous accumulation of tungsten in bone tissue with some sites having ~10-fold greater intensities than background levels. Localization of tungsten was similar to zinc, which is known for depositing in areas of active bone remodeling. Persistence of tungsten in cortical bone tissue following removal of the source indicates that it is retained in an insoluble form. The X-ray absorption near-edge structure (XANES) spectra for tungsten in these tissues indicate that it is no longer in the originally administered form, orthotungstate, but rather resembles the heteropolytungsate species, phosphotungstate. The acidic conditions and high phosphate concentrations present at bone resorption sites suggest that phosphotungstate may be forming *in situ* during bone remodeling.

While SR-μXRF is a powerful elemental mapping technique that has been used to map tungsten and zinc distribution in bone tissue, there are some limitations to the sensitivity and image resolution of this technique when imaging bone. The heterogeneity and thickness of the bone thin sections along with overlap of the tungsten L-edge with the zinc K-edge signals, complicates SR-μXRF data analysis, introduces minor artefacts into the resulting element maps, and decreases image sensitivity and resolution. To confirm and more carefully delineate these SR-μXRF results, we employed Laser Ablation Inductively Coupled Plasma Mass Spectrometry (LA-ICP-MS) to untangle the problem created by the K/L-edge overlap of the tungsten/zinc pair. While the overall elemental distribution results are consistent between the two techniques, LA-ICP-MS provides significantly higher sensitivity and image resolution compared to SR-μXRF measurements in

bone. These improvements reveal tissue specific distribution patterns of tungsten and zinc in bone, not observed using SR-µXRF. We conclude that probing elemental distribution in bone is best achieved using LA-ICP-MS, though SR-µXRF retains the advantage of being a non-destructive method with the capability of being paired to X-ray techniques, which determine speciation *in situ*.

LA-ICP-MS has the additional advantage of being a quantitative technique with the use of appropriate matrix-matched calibration standards. Determining the local concentrations of metals in bone provides valuable information about their mechanisms of uptake and action. A series of bone (BN), 7:3 hydroxyapatite:collagen (HC), and hydroxyapatite (HA) standards spiked with tungsten and zinc were created and tested as calibration standards for LA-ICP-MS analysis of bone tissue. The analytical performance of these standards was studied and validated at different step sizes using NIST SRM 1486 Bone Meal. The effect of matrix-matched calibration was assessed by comparing the calibration with BN and HC standards, which incorporate both inorganic and organic components of bone, to that of HA standards. HC standards were found to be more homogeneous and provide a linear calibration with better accuracy than other standards. The limits of detection for HC at a 15 µm step size were determined to be 0.24 and 0.012 $\mu g\ g^{-1}$ for zinc and tungsten, respectively. Using this approach, we quantitatively measured zinc and tungsten deposits in the femoral bone of a mouse exposed to 15 ppm tungsten for four weeks. Localized concentrations of zinc (942 $\mu g\ g^{-1}$) and tungsten (15.7 $\mu g\ g^{-1}$) at selected regions of enrichment were substantially higher than indicated by bulk measurements of these metals.

The powerful ability of XRF to detect multiple elements in a sample simultaneously was demonstrated by our serendipitous discovery of localized copper and zinc deposits in bone. Using SR-µXRF and XANES, we investigated the distribution and speciation of copper and zinc in the joint tissues of mouse and human samples. Copper was found to accumulate in collagen-rich tissues, namely ligament and the articular cartilage. Lysyl oxidase (LOX) is a well-known Cu(II) metalloenzyme that catalyzes the formation of cross-links within cartilage. However, Cu K-edge XANES measurements reveal that copper is present in these tissues as a reduced Cu(I) species. Further work is required to determine whether presence of a Cu(I) species indicates the role of a reduced Cu(I) species in LOX's catalytic mechanism, the presence of another Cu(I) species, or is simply due to photoreduction of Cu(II) in the X-ray beam. SR-µXRF experiments further revealed a highly localized zinc feature in the tidemark of articular cartilage, along with a generally

heterogeneous distribution throughout calcified bone tissue. The tidemark is the metabolically active zone in articular cartilage and marks the calcification front of the tissue. Zinc's presence here supports previous studies indicating the key role zinc plays in bone remodeling. XANES experiments reveal similarity between Zn *K*-edge spectra at the tidemark and in bone, to that of Zn-doped hydroxyapatite and alkaline phosphatase, the zinc metalloenzyme essential in bone formation and mineralization. More work is required to precisely define the nature of the zinc deposits in bone.

In this thesis we describe a method for mapping and quantifying local tungsten distribution in bone, as well as gaining information about its speciation *in situ*. The application of the described methods to other metal systems was demonstrated in our investigations of zinc and copper in bone tissue. Given the complexity of bone tissue and metal speciation under physiological conditions, *in situ* experiments such as this are greatly needed. The discovery of a tungsten polyoxometalate (POM) species in bone is particularly significant. First, it supports the claim that the aqueous chemistry of a metal dictates its uptake mechanism in bone. Understanding metal accumulation in bone thus requires experiments to be done under biomimetic conditions. Second, formation of a phosphotungstate-like species *in vivo* (along with the similarity of tungsten and zinc distribution) supports the hypothesis that Group 5 and 6 metal accumulation is related to bone remodeling. Formation of POMs generally requires acidic pH conditions, such as those present at bone resorption sites. Many POMs, including phosphotungstate, are known redox catalysts and their presence in bone could have significant health implications.

6.2. Suggestions for Future Work

Several knowledge gaps remain with regards to tungsten accumulation in bone. XANES alone is inadequate to positively identify tungsten speciation in bone. XANES measurements rely on the fingerprinting approach, or comparison of the XANES spectra recorded of tungsten in bone to that of reference species. While differences in the XANES spectra are clear between tetrahedral $[WO_4]^{2-}$ and octahedral polytungstates, differences for the various polytungstates are far subtler. In addition, comparisons between bone tungsten deposits and tungsten standards are approximate since tungsten reference species are not identical to that in bone. Accurately identifying tungsten's

speciation is necessary for effectively directing toxicological studies, understanding the mechanisms behind tungsten's toxicity, and developing effective remedial strategies.

Extended X-ray absorption fine structure (EXAFS) analysis is typically used to determine local structure around the tungsten atom, i.e. type, number and distances of coordinating atoms. However, standard X-ray absorption spectroscopy (XAS) at the tungsten L-edge suffers from broadening and a resulting loss of spectra resolution (Figure 6.1.).[1] Alternatively, high-energy resolution fluorescence detected extended X-ray absorption fine structure (HERFD-EXAFS) allows for transition metal spectra to be obtained at much higher resolutions (~2-3 times) than conventional XAS methods. As seen in Figure 6.2., this allows for the differentiation in the spectra for various tungsten compounds. Future work, therefore, could include applying this method to local tungsten deposits in bone to obtain more specific information about local environment, identities and locations of coordinating atoms, and atoms in the second sphere. This information would elucidate tungsten binding mechanisms in bone as well as aid in the development of appropriate treatment strategies to remove tungsten.
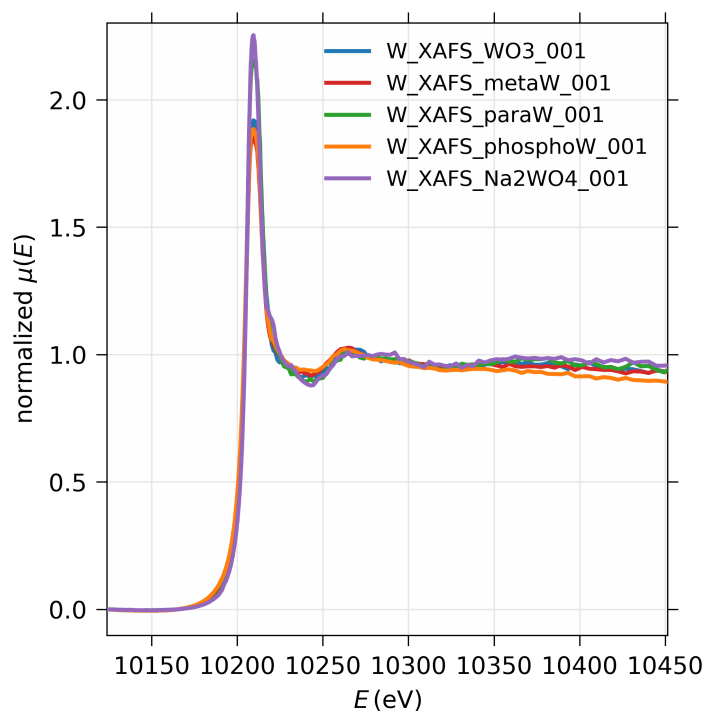
Figure 6.1. W L-edge XAS of tungsten standards: WO_3 (blue), metatungstate (red), paratungstate (green), phosphotungstate (orange), and orthotungstate (WO_4, purple).
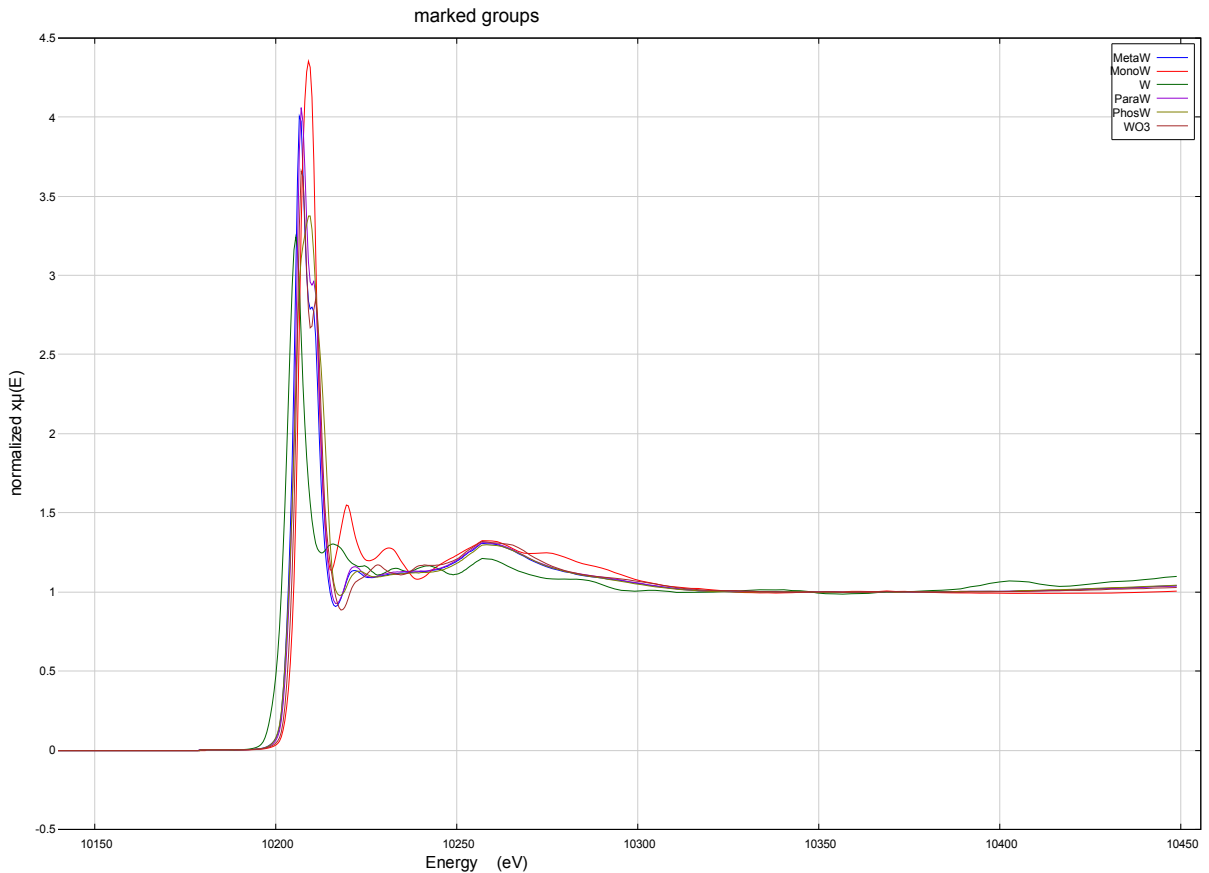
Figure 6.2. HERFD-XAS of tungsten standards: WO_3 (burgundy), metatungstate (blue), paratungstate (purple), phosphotungstate (army green), orthotungstate (WO_4, red), and $W_{(s)}$ (green).

Another possible avenue of research is to use our developed method for quantifying local tungsten deposits to gain more information about tungsten uptake and dynamics within bone tissue. Our collaborators, Kelly *et al.*, used bulk ICP-MS to quantify tungsten accumulation in bone after exposure to tungsten dissolved in water.[2] They found that the total tungsten content depends on the concentration of tungsten to which the individual was exposed. Moreover, tungsten concentration increased rapidly following the first week of exposure, after which the accumulation rate decreased significantly ($p < 0.001$) for the remainder of the experiment (Figure 6.3.). Lower exposures suggest an incomplete saturation of the bone compartment, as tungsten content here peaked at values below the bone concentration achieved with our highest exposure.
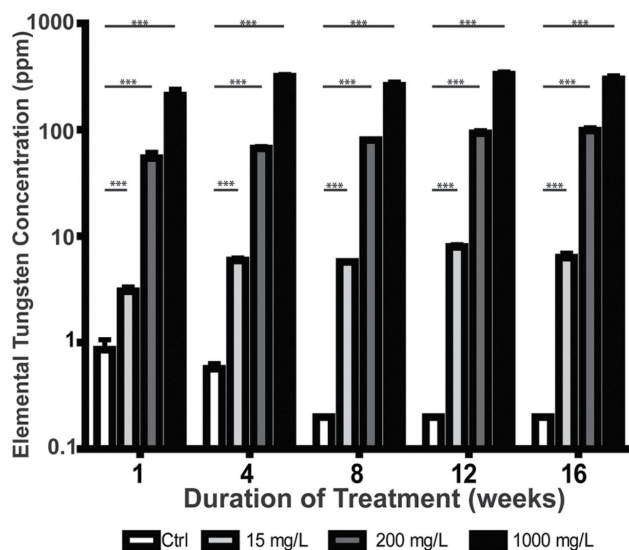
Figure 6.3. Tungsten levels in bone accumulate rapidly and are exposure dependent. After removal of bone marrow, tibia bones were analyzed for their elemental tungsten content by ICP-MS. Reused with permission.[2]

Further insight on these results and tungsten uptake mechanisms in bone could be gained by quantifying tungsten accumulation in the different bone compartments following exposure to different forms of tungsten (orthotungstate vs. polytungstates) at various time and concentration exposure regimes. The connection between tungsten uptake and bone remodelling may be further probed by co-treatment of mice with tungsten and bisphosphonate.

Lastly, the methods developed for the determination of tungsten speciation and distribution in bone may be applied to other systems of interest, such as the accumulation of other metals (lead, cadmium, strontium) in bone.

6.3. References

1.   Jayarathne, U.; Chandrasekaran, P.; Greene, A. F.; Mague, J. T.; DeBeer, S.; Lancaster, K. M.; Sproules, S.; Donahue, J. P. X-Ray Absorption Spectroscopy Systematics at the Tungsten L-Edge. *Inorganic Chemistry* **2014,** *53* (16), 8230-8241.

2.   Kelly, A. D. R.; Lemaire, M.; Young, Y. K.; Eustache, J. H.; Guilbert, C.; Molina, M. F.; Mann, K. K. In Vivo Tungsten Exposure Alters B-Cell Development and Increases DNA Damage in Murine Bone Marrow. *Toxicological Sciences* **2013,** *131*, 434-446.

Appendix

Beamline Descriptions

Synchrotron	CLS	NSLS-II	APS		NSRRC
Beamline	VESPERS	5-ID	13-ID-E	20-ID-B	17C1
Web Address	https://vespers.lightsource.ca/	https://www.bnl.gov/nsls2/beamlines/beamline.php?r=5-ID	https://gsecars.uchicago.edu/gsecars-facility/sector-13-beamlines/13-ide/	https://www.aps.anl.gov/Spectroscopy/Beamlines/20-ID	http://tls.conf.asia/bd_page.aspx?lang=en&port=17C1&pid=1404
Source	Bending magnet	21 mm undulator	36 mm undulator	36 mm undulator	Wiggler 20
Experiments	XRF	XRF, XAS	XRF; XAS	XRF; XAS	XAS
XRF E_0 (keV)	Polychromatic "pink" beam	12.4	10.5	10.5	---
Monochromator	---	Si (111) Horizontal Double Crystal	Si (111) cryo-cooled double-crystal	Si (111) LN2-cooled	Si (111) Double Crystal
Detector	4-element Vortex Si drift	4-element Si drift	4-element Si drift	**XRF:** Vortex Si drift (4-element) **XAS:** 13-element Ge	Lytle Detector

Facility Funding Acknowledgments